Effects of Complex Material-Environment Interactions on Hot Corrosion Mechanisms

---

A Dissertation
presented to
the faculty of the School of Engineering and Applied Science
University of Virginia

---

in partial fulfillment of the requirements
for the Degree
Doctor of Philosophy
by

K.J. Meisner

Acknowledgements

Most of this work was sponsored by The Office of Naval Research (ONR), research grant numbers N00014-14-1-0637 and N20A-T019. I would like to thank Dr. Dave Shifler of ONR for this funding as well as helpful comments on the characterization of marine turbine blades. I would also like to thank Dr. Valentina Angelici Avincola for extensive work on the low velocity burner rig, Dr. Brian Gleeson for the model NiCoCrAlY alloy samples and for helpful comments on the NiCoCrAlY furnace testing, Dennis Russom of Naval Sea Systems Command for supplying marine turbine blades, Dr. Bi-Cheng Zhou for collaboration on CALPHAD modeling, Dr. Jimmy Burns for helpful discussions on the cracking observed on turbine blades, Dr. Prasanna Balachandran for collaboration on the CMAS/$CaSO_4$ corrosion project and for his modeling expertise, Materials Research & Design (MR&D) for their collaboration on the CMAS/$CaSO_4$ project, Max Venaas at UC Irvine Advanced Power and Energy Program for designing the new burner rig combustion system, and Dr. Rob Golden of Rolls Royce for supplying the YSZ-coated samples. I would like to thank Cameron Miller for his help doing sample preparation and characterization of superalloys in his undergrad years, as well as the rest of the Opila research team for their support and help around the lab. I am also very thankful for the support of my family, especially my parents and brothers Ryan and Ian.

Table of Contents

1.0 Introduction

1.1 Present knowledge: high temperature oxidation

The term “hot corrosion” refers to the high temperature degradation of materials due to the presence of molten salt deposits, typically alkali metal sulfates such as Na_2SO_4. It involves the disruption of a metal’s protective oxide scale and therefore must be understood in relation to the typical oxidation of metals.

The simple reaction for the oxidation of a metal M is shown in Equation 1.

$$\frac{2x}{y}\mathrm{M(s)} + \mathrm{O_2(g)} \leftrightarrow \frac{2}{y}\mathrm{M_xO_y(s)} \tag{1}$$

In most situations, the metal and its corresponding oxide are solid and therefore the reaction involves a net decrease in entropy ($\Delta S < 0$) due to the consumption of the O_2 molecule with its three translational degrees of freedom in the gas phase. This net decrease in entropy is typically overcome by the decrease in enthalpy ($\Delta H < 0$) accompanied by the transformation of a metal to its relatively stable oxide (except in the case of precious metals such as Pt and Au). The Gibbs free energy change upon oxidation, as shown in Equation 2, is therefore negative but increasing with temperature for most metals.

$$\Delta G^{\circ}{}_{\mathrm{rxn}} = \Delta H^{\circ}{}_{\mathrm{rxn}} - T\Delta S^{\circ}{}_{\mathrm{rxn}} \tag{2}$$

The relative stabilities of metal oxides and their temperature dependence are illustrated by Ellingham diagrams [1] such as that in Figure 1. These diagrams plot the Gibbs free energy of formation of metal oxides normalized to one mol of O_2(g). The more stable oxides, with more negative ΔG°, are found lower on the diagram. Most metals have a similar increasing temperature dependence due to the dominance of O_2(g) consumption on ΔS°, as explained previously.

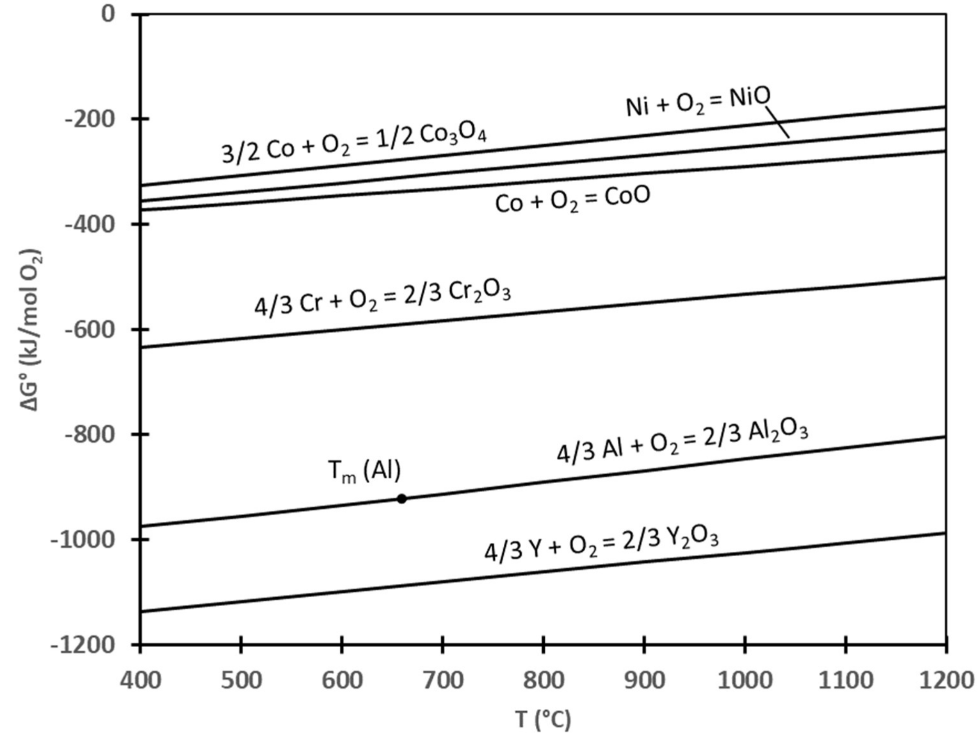

Figure 1. An Ellingham diagram for the formation of various metal oxides relevant to this work

The Ellingham diagram shows that Y_2O_3, followed by Al_2O_3, then Cr_2O_3, and lastly oxides of Ni and Co, are the most thermodynamically favorable product of an oxidizing Ni-Co-Cr-Al-Y alloy. Ellingham Diagrams may be constructed in an analogous manner for other metal compounds, such as metal sulfides [1]. A reference state other than the pure metal may also be chosen. For example, the relative stability of the sulfate salts with respect to their corresponding oxides will be shown later.

However, a freely oxidizing metal is not in thermodynamic equilibrium with its surroundings. The oxidation rate, as well as the identity of the external oxide scale layer(s), must be determined from the rate of metal and oxidant transport and/or the chemical reaction kinetics. The foundational mathematical description of bulk metal oxidation is provided by Wagner [2–4]. Wagner considers the rate-limiting mass transport step, such as the transport of point defects in the oxide scale. Figure 2 shows the rate-controlling solid state diffusion processes that take place in a simple Ni-Pt alloy. The gaseous diffusion of O_2 and the reaction kinetics at the reaction interface are typically orders of magnitude faster that solid state processes and therefore can be neglected for these conditions.

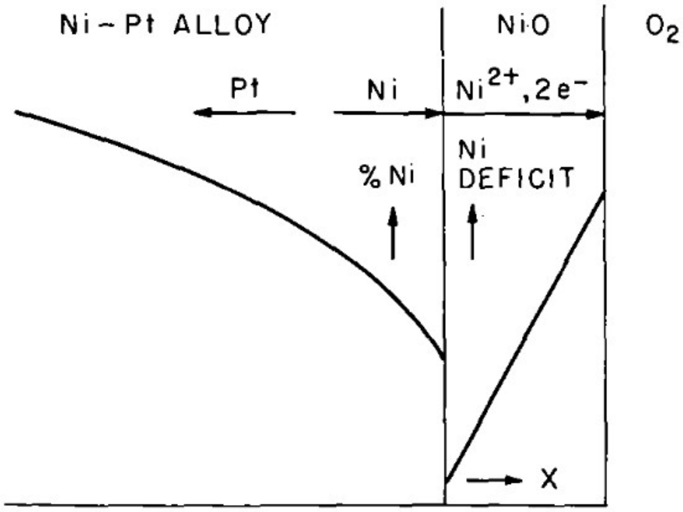

Figure 2. Diffusion processes during the oxidation of Ni-Pt alloys. From Wagner 1952 [2]

For a Ni-Pt alloy, only Ni forms a stable oxide and so there is a net flux of Ni towards the metal/oxide interface and then through the oxide as Ni^{2+}. At the oxide/gas interface, Ni is oxidized to Ni^{2+}. Equivalently, there is a net flux of Pt away from the metal/oxide interface. For growth of the oxide layer to continue, there must be inward O^{2-} transport and/or outward Ni^{2+} diffusion through the oxide. The identities of the diffusing species through the oxide depend on its defect chemistry. NiO is a metal-deficient oxide and therefore grows via outward migration of Ni^{2+} (or, equivalently, inward migration of cation vacancies) [2]. Assuming a constant diffusivity, the scale growth will be inversely proportional to the scale thickness, x as shown in Equation 3 [2,5]. Integration yields Equation 4, which shows that scale thickness varies parabolically (i.e. with the square root of time) and may be described by a parabolic rate constant k'.

$$\frac{dx}{dt} = \frac{k'}{x} \tag{3}$$

$$x(t) = \sqrt{2k't} \tag{4}$$

Analogous rate laws may be derived for other oxidation rate measurements such as mass gain or displacement of the metal/oxide interface during scale growth. Parabolic kinetics are applicable to most adherent, dense, and sufficiently thick (on the order of micrometers) oxide scales that are desirable for engineering applications. This is because parabolic kinetics are commonly the result of relatively slow solid-state diffusion processes. This rate law is not applicable for early stages when the oxide is a thin film or when the scale is cracked, porous, or spalled [5,6].

In a binary alloy system consisting of a more noble element A and a less noble element B, such as the example of Ni-Pt above, a minimum critical concentration of element B is required for the formation of a continuous external oxide scale. Equation 5 shows a simplified equation for this critical solute concentration as originally derived by Wagner [4,6].

$$N_B = \frac{V}{z_B M_O}\left(\frac{\pi k'}{D}\right)^{1/2} \tag{5}$$

N_B is the critical atomic fraction of element B required for an external B-oxide scale, V is the molar volume of the alloy, z_B is the valence of B cations, M_O is the atomic weight of oxygen, D is the diffusion coefficient of B in the alloy, and k' is the parabolic rate constant mentioned previously. Qualitatively, this relation shows that the minimum required solute concentration is determined by the competition between the rate at which an alloy can supply element B to the metal/oxide interface (related to D) and the rate of consumption of B at this interface to form an oxide (related to k'). Below this critical concentration, oxidation occurs via the formation and growth of oxide precipitates beneath the metal-gas interface, which prevents the formation of a continuous external scale [5,6].

This general principle, that there must be a large enough reservoir of the oxide-forming element to maintain a protective external scale, may be generalized to multicomponent alloys. Other beneficial factors include slow growth rate of the oxide, good adhesion of the oxide to the metallic substrate, and chemical compatibility with other species such as water and sulfur [5,6]. Al_2O_3, Cr_2O_3, and SiO_2 are typical oxide scales with desirable properties for high temperature applications [5,6].

Elements other than the oxide-forming element may play a role in the protectiveness of the oxide. An element that forms an oxide of intermediate stability between two other alloying elements (e.g., Cr in Ni-Cr-Al and Fe-Cr-Al) may promote the formation of the more stable external scale (e.g. Al_2O_3) at lower concentrations than that predicted for just the binary system using Equation 5. This phenomenon is called the "third element effect" and likely includes multiple, simultaneous mechanisms. One mechanism may be that oxidation of third element lowers the pO_2 at the solid-gas interface, promoting the formation of the more stable oxide (Al_2O_3 in the example of Ni-Cr-Al) over the less stable oxide (e.g., NiO) [5,6]. These less thermodynamically stable oxides are called "transient oxides" and may form in the early stages of oxidation, prior to the formation of a continuous scale, because they are faster-growing [5,6]. Inhibition of transient oxidation appears to benefit the formation of a protective single-phase oxide [7].

Small amounts (on the order of 0.1 wt%) of reactive elements such as Y, Hf, Zr, and Ce greatly reduce the spallation of Al_2O_3 and Cr_2O_3 scales, particularly under thermal cycling conditions [8–11]. This is termed the "reactive element effect" (REE). The REE has been a subject of considerable study and debate for decades and continues to be an active area of research. An in-depth explanation of all proposed REE mechanisms is beyond the scope of this work, but a few mechanisms are generally accepted. Sulfur contributes to spallation by diffusing to the metal-oxide interface and weakening the interfacial bond [11–14]. Reactive elements have an affinity for S, and so additions of Y or Hf may be efficient S getters. Reactive element additions also change Al_2O_3 scale growth from combined outward metal cation diffusion and inward O^{2-} diffusion to inward O^{2-} transport only, reducing the formation of interfacial voids and oxides of other alloying elements [11,15]. Other effects possibly include reduced alloy grain size and thus enhanced transport of Al or Cr to the oxide scale, segregation of rare earth cations to oxide grain boundaries that block transport of other ions through the scale, and modification of the oxygen gradient within the scale [11].

1.2 Present knowledge: hot corrosion

Hot corrosion is an accelerated oxidation process due to the presence of a corrosive deposit, typically a molten salt [5,6,16]. Molten Na_2SO_4 is of particular interest in gas turbines. It is presumed to form via ingestion of NaCl in the environment and subsequent reaction with SO_x in the combustion gases [16,17]. Equations 6 and 7 show proposed reactions for Na_2SO_4 formation in gas turbine environments [17].

$$2\mathrm{NaCl(g)} + \mathrm{SO_2(g)} + \frac{1}{2}\mathrm{O_2(g)} + \mathrm{H_2O(g)} \leftrightarrow \mathrm{Na_2SO_4(g)} + 2\mathrm{HCl(g)} \tag{6}$$

$$2\mathrm{NaCl(g)} + \mathrm{SO_3(g)} + \mathrm{H_2O(g)} \leftrightarrow \mathrm{Na_2SO_4(g)} + 2\mathrm{HCl(g)} \tag{7}$$

DeCrescente and Bornstein originally believed that these reactions occur homogenously in the gas phase and that condensed phase $Na_2SO_4(s, l)$ deposits on surfaces when the partial pressure of $Na_2SO_4(g)$ exceeds the equilibrium partial pressure of $Na_2SO_4(g)$ for the environmental conditions (i.e. the salt deposits via a dew point phenomenon) [17]. Note that this deposition mechanism will be discussed and investigated later in greater detail.

Upon deposition and melting, the interaction of liquid Na_2SO_4 with a metallic substrate is electrochemical in nature. The anodic dissolution or oxidation of metal is coupled with the cathodic reduction of SO_3 in the melt, as shown in Equations 8 and 9 [18,19].

$$\mathrm{M} \leftrightarrow \mathrm{M}^{n+} + \mathrm{ne}^{-} \tag{8}$$

$$\mathrm{SO_3^{-}} + \mathrm{e}^{-} \leftrightarrow \mathrm{SO_2} + \mathrm{O}^{2-} \tag{9}$$

The molten Na_2SO_4 contains equilibrium amounts of Na_2O and SO_3 in solution as shown in Equation 10 [19].

$$\mathrm{Na_2SO_4(l)} \leftrightarrow \mathrm{Na_2O\ (in\ Na_2SO_4\ melt)} + \mathrm{SO_3\ (in\ melt)} \tag{10}$$

Equation 10 describes an acid-base equilibrium, with SO_3 the acidic oxide and Na_2O the basic oxide according to Lewis acid-base theory [20]. Therefore, the basicity of a melt corresponds to log Na_2O (equivalently, log O^{2-}) and the acidity corresponds to log pSO_3 [19]. This is analogous to the pOH and pH of an aqueous solution.

Of course, typical engineering metals and alloys possess external oxide scales at high-temperature oxidizing conditions. The acid-base character of the molten salt gives it the ability to dissolve oxide scales through an acid-base reaction called “fluxing” [16,21–24]. Reaction with the basic component, as in Equation 11, is called “basic fluxing” and reaction with the acidic component, shown in Equation 12, is “acidic fluxing” [21].

$$\mathrm{M_xO_y(s)} + \mathrm{Na_2O\ (in\ melt)} \leftrightarrow \mathrm{Na_2M_xO_{y+1}\ (in\ melt)} \tag{11}$$

$$\mathrm{M_xO_y(s)} + \mathrm{ySO_3\ (in\ melt)} \leftrightarrow \mathrm{M_x(SO_4)_y\ (in\ melt)} \tag{12}$$

This simultaneous electrochemical and acid-base description of corrosion is familiar to aqueous corrosion scientists, albeit in a different context. Stability diagrams analogous to Pourbaix potential-pH diagrams [25,26] may be constructed for systems relevant to hot corrosion [18,27,28]. Figure 3 shows such a stability diagram for Cr [29], with regions of passivation (Cr_2O_3) and regions of corrosion where non-protective reaction products are stable (e.g. $Cr_2(SO_4)_3$(s) and Na_2CrO_4(l)). The corresponding diagram for Al in Na_2SO_4 [30], shown in Figure 4, illustrates the differences in oxide solubility.

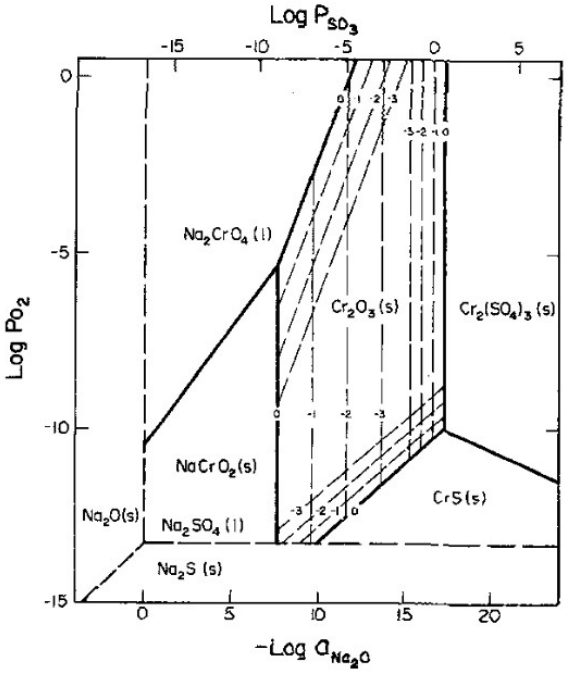

Figure 3. Stability diagram for Cr in Na_2SO_4 at 1200 K as a function of acidity. (pSO_3)/basicity (log a Na_2O) and oxygen potential. The dashed lines within the Cr_2O_3(s) stability region correspond to the phase boundary positions as a function of log [Cr^{3+}] in the melt. From Zhang 1986 [29].

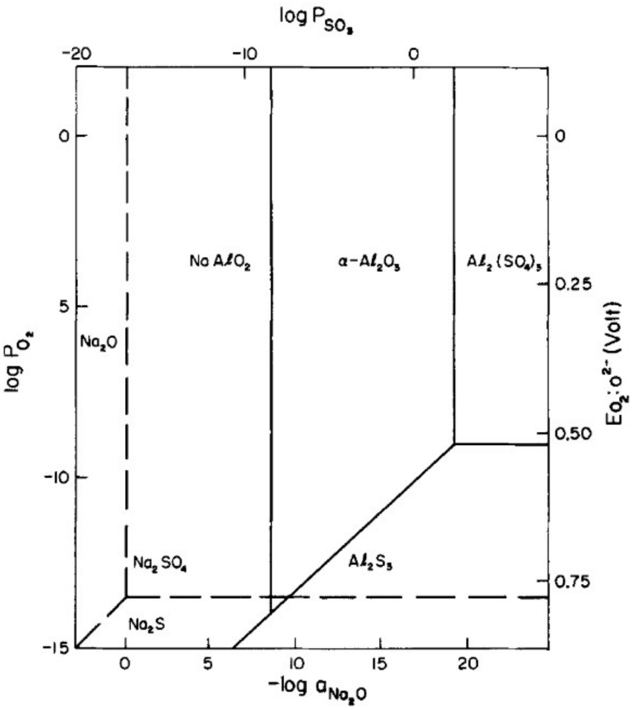

Figure 4. Stability diagram for Al in Na_2SO_4 at 1200 K as a function of acidity (pSO_3)/basicity (log a Na_2O) and oxygen potential. From Schryer 1985 [31].

There are two primary temperature regimes in which hot corrosion of Ni- and Co-base alloys have been observed. One is at approximately 900 °C, above the melting point of pure Na_2SO_4 (884 °C), and the other is at approximately 700 °C [16,32]. Corrosion at the higher temperature regime is called "high temperature hot corrosion" (HTHC) or Type I hot corrosion while that around 700 °C is called "Low temperature hot corrosion" (LTHC) or Type II hot corrosion [16]. A liquid may form at around 700 °C because Na_2SO_4 forms low-melting temperature eutectic mixtures with sulfates of alloying elements. The eutectic temperature of Na_2SO_4-$NiSO_4$ is 671 °C and that of Na_2SO_4-$CoSO_4$ is 590 °C [33]. Sulfates of Ni and Co form by reaction of the transient oxides with SO_3 in the combustion gas, as shown in Equation 13. Therefore, a minimum pSO_3 in the environment is required for Equation 13 to be thermodynamically favorable.

$$\mathrm{MO(s) + SO_3(g) \leftrightarrow MSO_4(s)} \tag{13}$$

Luthra and LeBlanc determined that this minimum pSO_3 is roughly $2\mathrm{x}10^{-5}$ atm for $CoSO_4$ and $2\mathrm{x}10^{-4}$ atm for $NiSO_4$ at 700 °C [34]. The reaction of SO_2(g) and O_2(g) to form SO_3(g), as shown in Equation 14, is entropically unfavorable and therefore pSO_3 decreases with temperature [35].

$$\mathrm{SO_2(g) + \tfrac{1}{2}O_2(g) \leftrightarrow SO_3(g)} \tag{13}$$

With increasing temperature, this decreasing pSO_3 and shortening of the transient oxidation stage result in slower corrosion rates at temperatures greater than 700 °C but below 884 °C [36]. At 884 °C and above, the pure Na_2SO_4 melts and HTHC may proceed. Figure 5 schematically shows this dependence on temperature and pSO_3 [16].

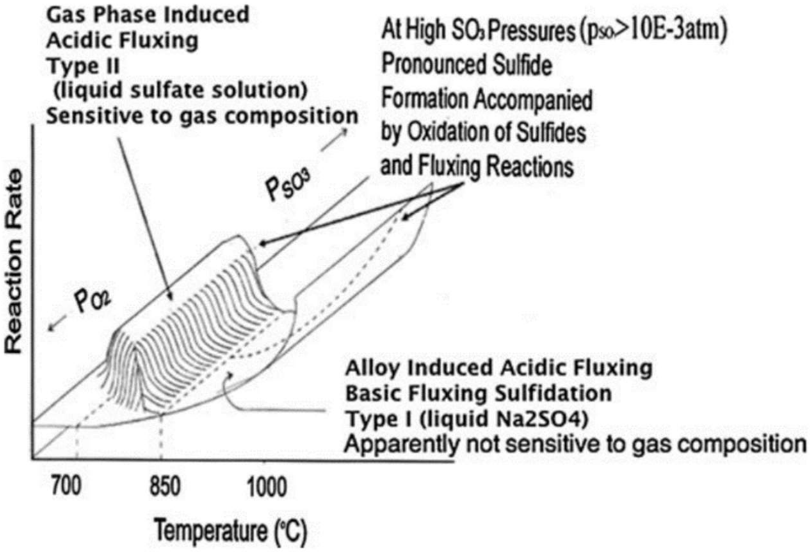

Figure 5. Schematic of temperature dependence for Na2SO4-induced hot corrosion and oxidation. Reprinted by permission from Springer Nature Customer Service Centre GmbH: Springer <u>Oxidation of Metals</u> "Hot Corrosion of Metals and Alloys" by Pettit, F., Copyright (2011) [16].

2.0 Motivation

2.1 Characterization of service hardware

Corroded marine gas turbine blades were characterized to identify corrosion modes to be studied in greater detail in the laboratory. These service hardware findings motivate subsequent experiments in a more controlled experimental settings, as will be discussed. This section is reproduced with slight modifications from the previously published article "Hot Corrosion of Shipboard Gas Turbine Blades" [37]. It is reproduced here to demonstrate knowledge gaps and the motivations for the laboratory experiments that comprise the bulk of this dissertation. Reprinted by permission from Springer Nature Customer Service Centre GmbH: Springer Oxidation of Metals "Hot Corrosion of Shipboard Gas Turbine Blades", Meisner, K.J., Opila, E.J. Copyright (2020).

2.1.1 Abstract

Turbine blades removed from the first stage of a shipboard gas turbine engine for excessive degradation were characterized. Scanning electron microscopy (SEM) coupled with energy dispersive spectroscopy (EDS), X-ray diffraction (XRD), and inductively-coupled plasma optical emission spectroscopy (ICP-OES) were used to characterize corrosion deposits and features of field hardware that are not typically obtained in controlled laboratory settings. Corrosion was associated with deposits of varying compositions on the airfoil, beneath the platform, and within cooling passages. Deposits on the airfoil were primarily sodium sulfate presumably derived from seawater. Deposits below the platform and within cooling channels were crystalline aggregates of Ca, Mg, Al, and Si compounds presumably derived from dust and sand. FactSage [38]

thermochemical calculations were performed for gas turbine environments and results are used to explain variations in deposit chemistry. The results show that solid sodium sulfate may not be retained in some gas turbine conditions, leaving the deposits rich in Ca and Mg compounds. Gaps in understanding this complex environment are identified.

2.1.2 Introduction

Superalloy components and their coatings are known to be attacked by molten salt species in gas turbines. Gas turbine combustion environments result in accumulation of deposits on hardware such as turbine blades, leading to accelerated high temperature oxidation/corrosion processes referred to as "hot corrosion" [16]. The deposits are commonly Na_2SO_4 and other compounds of the alkali metals and alkaline earth metals. One hypothesis is that Na_2SO_4 forms in marine gas turbine conditions due to ingested NaCl and sulfur impurities in the fuel and/or environment, as shown previously in Equations 6 and 7 [16].

Note that while the reactions in Equations 6 and 7 are thermodynamically favorable the kinetics are slow, especially considering the short residence times of gases in turbines. Schofield, Steinberg, and Hynes performed spectroscopic and kinetic analyses of Na- and S-doped flames under varying conditions. They concluded that Na_2SO_4 is not a major product; other Na species such as NaOH are dominant [39–41]. Reactor experiments by Hanby [42] suggest that Reactions 6 and 7 cannot form sufficient amounts of Na_2SO_4 within engine residence times ($\leq$ 16 ms). He hypothesized that Na_2SO_4 forms via impaction of condensed phase NaCl particulates on turbine components, which remain in place long enough to convert to the sulfate [42]. Nevertheless, most research identifies NaCl and Na_2SO_4 in seawater and S from the fuel or environment as the main source of Na_2SO_4.

In the case of Na_2SO_4, this salt may condense onto metal surfaces at temperatures below its dew point in the gas turbine [43], resulting in hot corrosion. More recently, aircraft gas turbine deposits other than Na_2SO_4 have attracted attention. A review by Krisak, Bentley, Phelps, and Radsick argues that Ca-containing deposits are the dominant corrodents in today's aircraft engines due to recent case studies associating Ca-rich deposits with the areas of greatest material loss on turbine components [44]. They also state that the previously-discussed kinetic limitations of Na_2SO_4 formation [39–42] are evidence against it being the most important depositing species. Cited case studies identify $CaSO_4$, a calcium-magnesium-aluminosilicate (CMAS) glass, and other CMAS-type deposits as the most corrosive [45–47]. CMAS is known to form via ingestion of sand and is particularly corrosive above its melting point, which varies with composition but is typically ≥ 1150 °C [48,49]. The maximum operating temperatures of marine gas turbines (approximately 900 °C) are too low for CMAS glass corrosion, but the above studies suggest the need for re-examining marine gas turbine deposits for compounds other than Na_2SO_4. Complex deposit mixtures rich in Ca, Mg, Al, and Si on corroded marine turbine blades have been reported have been reported by Shifler [50–52].

In this study, turbine blades from the hot section of a shipboard engine were characterized. These turbine blades were previously removed from service after an inspection revealed them to be degraded. Hot corrosion morphologies and deposits were investigated using electron microscopy and analytical chemistry techniques. Emphasis was placed on the characterization of both the engineering materials (the superalloys and their metallic coatings) and the deposits that formed from the ingestion of environmental impurities. FactSage thermochemical modeling software [38] was used to calculate the equilibrium compositions of deposits predicted in service environments and the results are compared to the experimental findings. Ca, K, Mg, Al, Si, and Fe species are identified as deposits in this study. Deposit formation and possible effects on hot corrosion mechanisms are discussed.

2.1.3 Materials and methods

Five turbine blades (labeled A1 through A5) from the first stage of a marine gas turbine were examined. A1, A2, A4, and A5 all exhibited cracking at the trailing edge of the airfoil tip. Each blade consists of the cast equiaxed nickel-base superalloy Mar-M247 of nominal composition (in weight percent) 0.15 C, 8.4 Cr, 10.0 Co, 10.0 W, 0.7 Mo, 3.0 Ta, 5.5 Al, 1.0 Ti, 1.5 Hf, 0.015 B, 0.05 Zr, bal. Ni [53] with a 100 µm thick CoNiCrAl overlay coating intended for hot corrosion protection. Small additions of elements such as Y or Hf may be present in the coating but are too dilute for detection. The Mar-M247 consists of γ' Ni_3Al precipitates in a γ matrix, with composition from EDS shown in Table 1 compared to nominal values [53]. The CoNiCrAl coating has a composition of approximately 62.3 Co/19.3 Ni/13.8 Cr/4.5 Al (in weight percent) and consists of β CoAl/NiAl precipitates in a γ matrix. It is possible the coating originally contained more Al and/or Cr because these elements may be depleted via oxidation and sulfidation. The time in service and exact service conditions are unknown. However, it may be assumed that corrosion occurred within the range of approximately 600-925 °C. The lower limit is assumed because hot corrosion typically requires melting of the deposits, which often occurs in the range of 600-700 °C [34,54,55]. The typical maximum operating temperate of this gas turbine is 925 °C. Figure 6 shows blade A1 and is representative of all five specimens where pitting on the pressure side of the airfoil and corrosion beneath the platform were observed.

Table 1. Composition of Mar-M 247 substrate by EDS

Mar-M 247 Composition		
	Nominal [Harris 1984]	EDS
Ni	Bal.	62.2
Co	10.0	10.4
W	10.0	8.7
Cr	8.4	8.0
Al	5.5	4.7
Ta	3.0	2.4
Hf	1.5	1.7
Ti	1.0	1.0
Mo	0.7	0.8

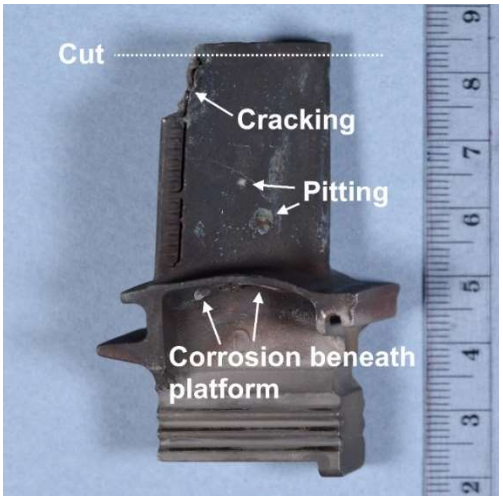

Figure 6. View of the pressure side of Blade A1 showing degradation. The location of the cut to inspect cooling channels is shown.

An FEI Quanta 650 Field Emission Gun Scanning Electron Microscope (SEM) coupled with an Oxford Instruments X-Max 150 Energy Dispersive X-ray Spectroscopy (EDS) detector were used to characterize the exterior surfaces of the blades. Cross sections of blades A1 and A5 were prepared by cutting, grinding, and polishing with non-aqueous media to preserve water-soluble deposits and corrosion products for examination by SEM and EDS. Blade A1 was cross-sectioned in three positions: 2 mm from the airfoil tip and through two of the largest pressure-side pits, as indicated in Figure 6. Blade A3 was sectioned vertically through its long axis to examine corrosion and cracking beneath the platform.

Deposits of foreign material were discovered beneath the platform and in the cooling channels, particularly near the airfoil tip. This material was dislodged from Blade A2 (from beneath the platform) and Blade A4 (from within the cooling channels). SEM and EDS were used to characterize the morphology and composition of the deposit particles. X-ray diffraction (XRD) using a Malvern Panalytical Empyrean X-ray diffractometer was performed on both the A4 cooling channel deposits and the A2 under-platform deposits to identify phases present. Phases were identified using the Malvern Panalytical HighScore suite [56]. The top 1 cm of the airfoil (as measured from the tip) of Blade A1 was digested in deionized water for 24 hours to dissolve water soluble species present on the exterior surface and in cooling channels. An addition of 0.5 mL of 12 M HCl to the digestion solutions ensured the dissolution of any water-insoluble particles in the digestion solution. This solution was characterized using inductively-coupled plasma optical emission spectroscopy (ICP-OES) with a Thermo Scientific iCAP 6000 spectrometer.

The Fact Pure Substance database was used with FactSage [38] to predict the composition of deposits. The Reaction module was used to construct an Ellingham diagram for the formation of sulfates from their corresponding oxides. The Gibbs free energy of reaction, ΔG°_{rxn} per mole of SO_3, was used to create an Ellingham diagram and predict the chemical species in the deposits along with the XRD, ICP-OES, and EDS results. The Predom module was used to construct predominance diagrams for the expected phases across ranges of pO_2 and pSO_3. Lastly, the Equilib module allowed for estimation of the equilibrium gas and deposit composition via Gibbs free energy minimization. Because deposits were found in both cooling channels and on the blade exterior, both of these environments were studied. The combustion gas stream was approximated by a composition consisting of F-76 marine diesel with 0.1 wt% sulfur, air (at a 50:1 A/F ratio), and enough sea spray to establish 5 ppmw of Na in the gas stream. The cooling air stream was approximated with the same composition minus the fuel and sulfur. The C:H:N ratio of F-76 fuel was determined by Elemental Analysis Inc. using combustion analysis. The composition used for sea spray was that of ASTM D1141 [57]. Temperatures were set to 700 and 900 °C and pressure was set to 15 atm. The amount of S and Na in the system was then varied to investigate the effects of varying fuel S content and seawater ingestion.

2.1.4 Results

Material Degradation

Figure 7 shows backscattered electron (BSE) micrographs and illustrations of the areas of greatest metal loss due to corrosion. Figure 7a shows that on the pressure side, the deepest pits extend halfway through the material (> 300 μm penetration). Corrosion pits have clearly breached the coating and were consuming substrate material. Elsewhere on the pressure side, pits that do not breach the coatings nevertheless penetrate deeply. Figure 8 shows a hot corrosion pit that barely stops short of the substrate. There is a depletion zone in the vicinity lacking β precipitates, suggesting that the reservoir of Al is locally depleted by diffusion to the surface. Indeed, EDS of the corrosion scale in Figure 9 shows it is mostly non-protective Cr_2O_3 with Al_2O_3 and Al sulfides at the metal-scale interface. Similar pits were found on the suction side, but none breached the coating.

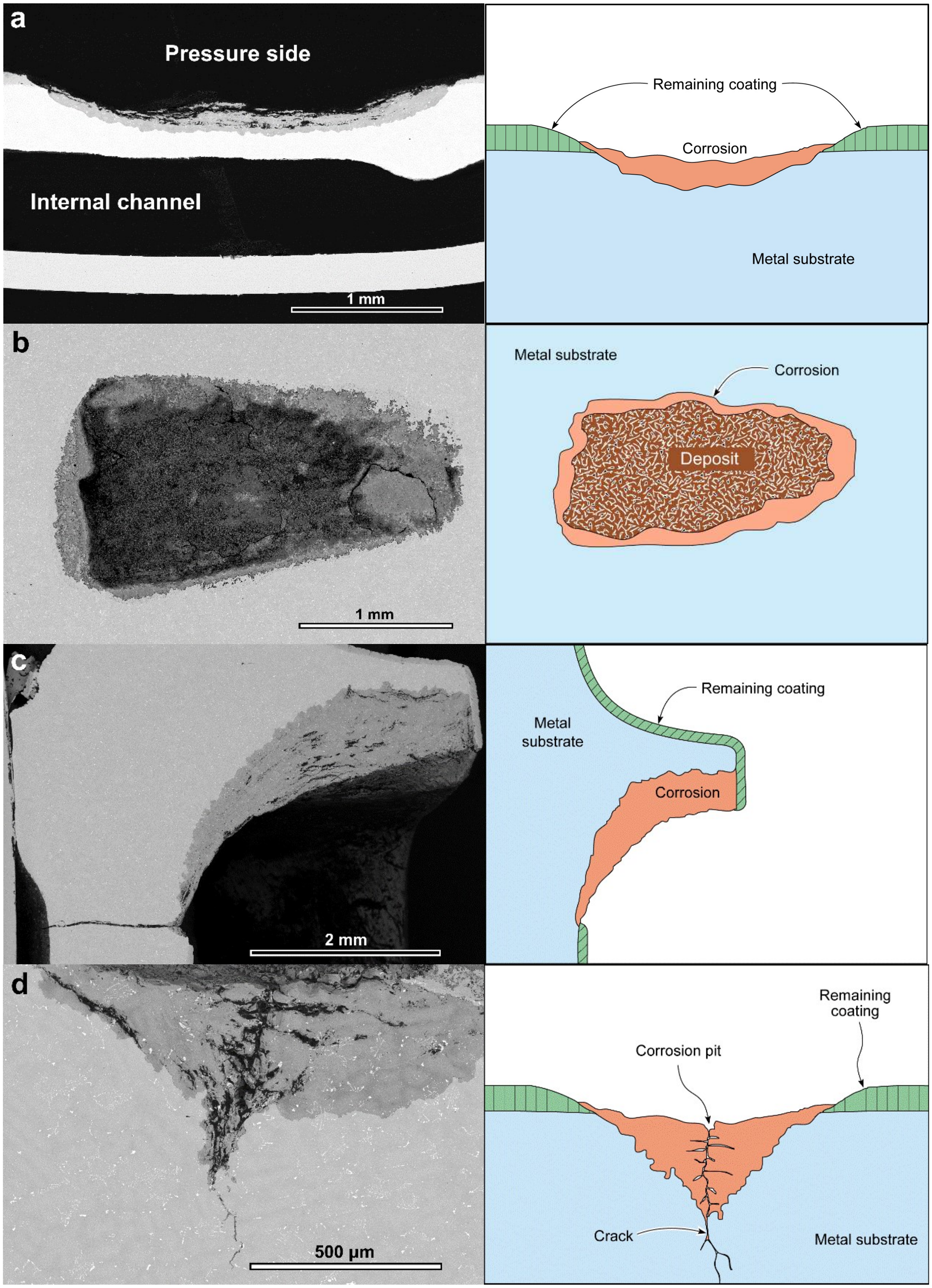

Figure 7. Major corrosion modes: a) Pressure-side pitting b) Corrosion within cooling channels c) Corrosion beneath the platform of d) Under-platform corrosion-induced cracking

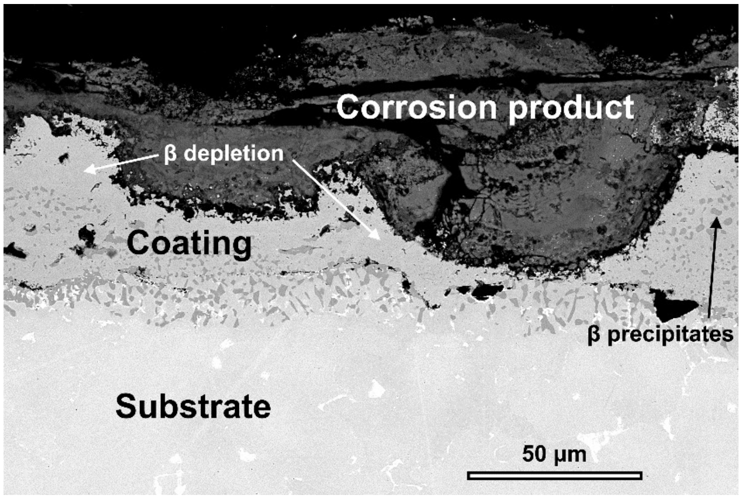

Figure 8. Cross-section of Blade A1 showing pressure side pitting

Figure 7b shows a cross-section (2 mm from the airfoil tip) through a cooling channel in blade A1. The inner surface is corroded and foreign material blocks the entire channel cross-section. EDS suggests these deposits consist of mixtures of Na, K, Ca, Mg, Fe, Al, and Si oxides, sulfides, and/or sulfates. Around other channels, up to 200 µm of material is consumed, as shown in Figure 10. EDS maps in Figure 11 show Al and Cr sulfides near the metal/scale interface. While this scale also contains oxides and sulfides of Cr and Al, it contains a significant amount of NiO compared to the exterior CoNiCrAl coating.

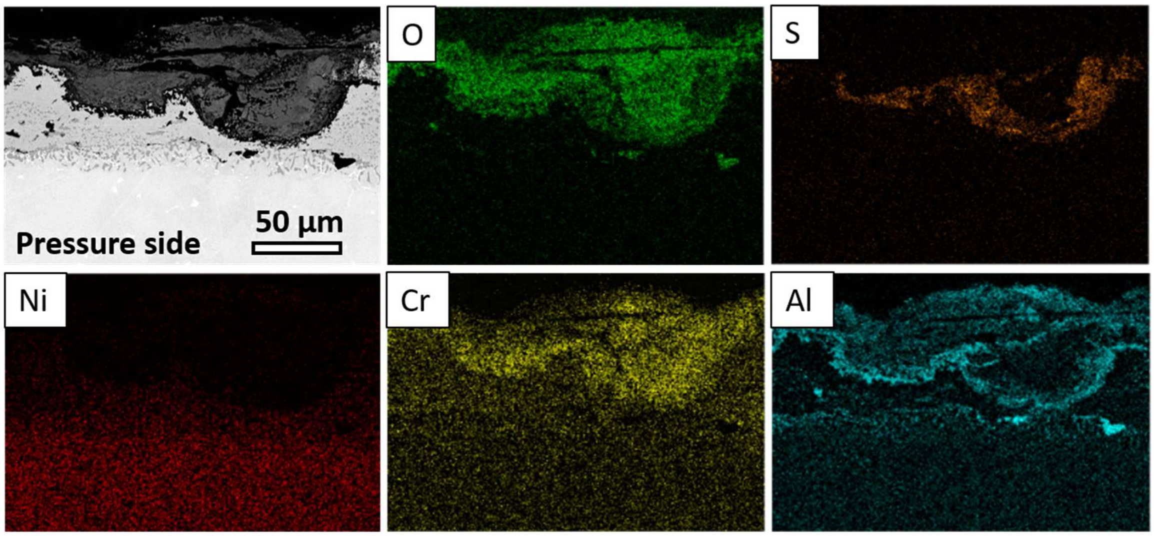

Figure 9. EDS maps of pitting on Blade A1 pressure side

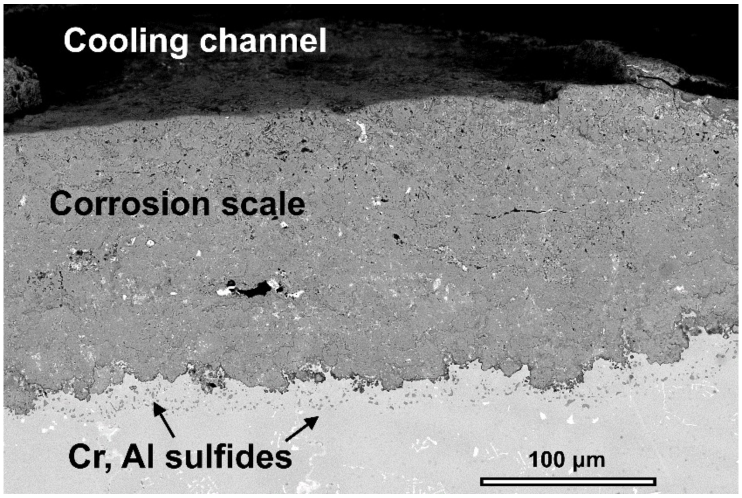

Figure 10. Corrosion within cooling channel of Blade A1

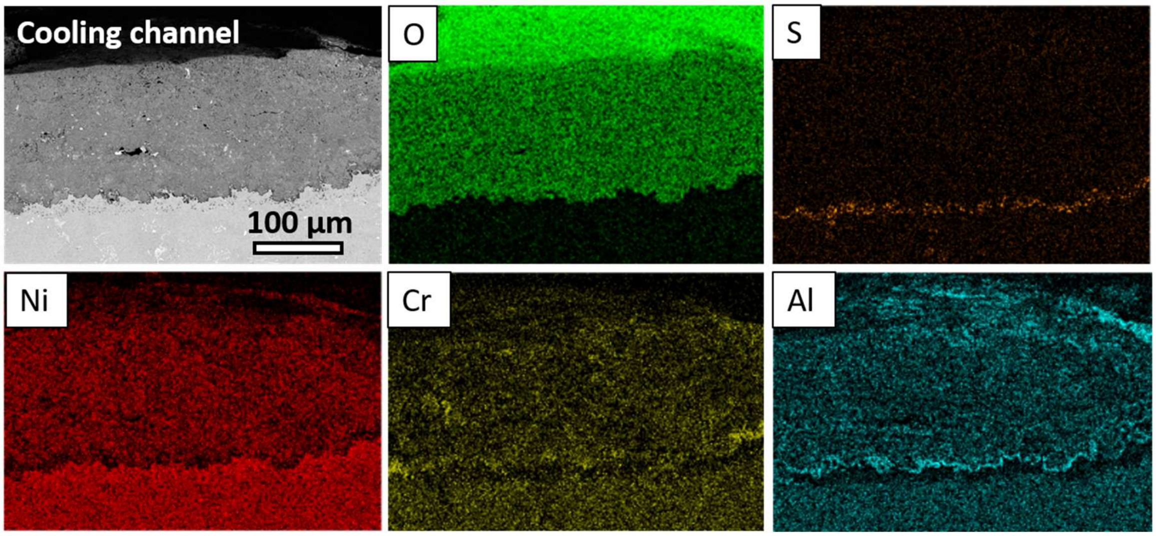

Figure 11. EDS maps of corrosion withing Blade A1 cooling channel

Figure 7c shows corrosion beneath the platform of blade A5. This area shows metal loss of up to 1 mm which represents the greatest amount of metal loss of any location on the blades. EDS suggests the corrosion product consists of Al_2O_3, Cr_2O_3, and sulfides of Al and Cr. A through-wall crack is also visible that likely initiated at the exterior surface where there is corrosion, as there is a corrosion pit there that may have acted as a stress concentrator. This is consistent with other cracks beneath the platform that are not through-wall. Figure 12 shows such a crack and is located at the exterior surface where a corrosion pit is present. Higher magnification micrographs show oxidation and corrosion along the length of the crack, suggesting the crack allowed corrosive species to penetrate deep into the substrate. While not visible in Figure 7c, similar under-platform corrosion in the other blades were associated with crystalline Ca-Mg-Fe-Al-Si oxide deposits similar in composition to those found in the cooling channels. However, the corrosion morphology below the platform is different from that in the cooling channels; the underside of the platform lacks the sulfides of Al and Cr near the metal/scale interface in the cooling channels.

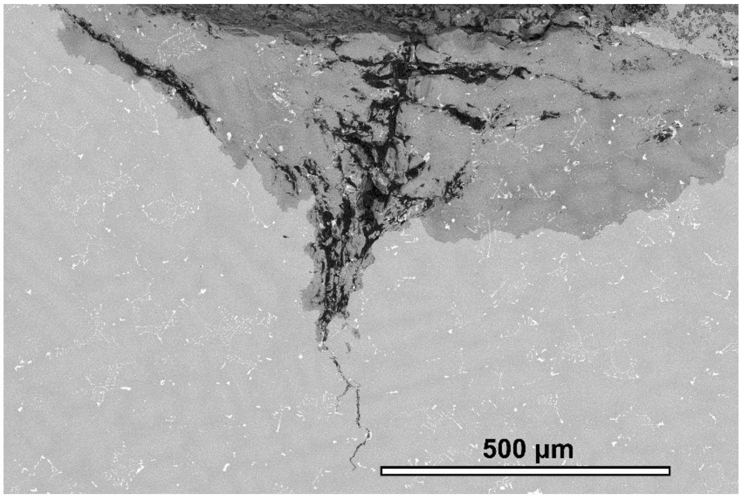

Figure 12. Crack originating from a corrosion pit beneath the platform of Blade A5

Deposits

Figure 13 is a backscattered electron micrograph showing deposits on the pressure side of the airfoil of Blade A2. The deposits (dark grey relative to the oxidized metal) are circular and on the order of tens of micrometers in diameter. EDS of the deposits found on the airfoil, in the cooling channels, and beneath the platform are shown in Table 2. The results indicate that mostly Na_2SO_4 is present as a corrosion product on the pressure side of the airfoil. The deposits in Figure 13 do not uniformly cover the entire airfoil surface. The ones shown here are from lower on the airfoil, close to the platform and the trailing edge. This section of the blade is presumably cooler, promoting deposition and decreasing volatilization of Na_2SO_4. The assumptions presented here are validated by the absence of Na_2SO_4-type deposits higher up on the airfoil, except on the trailing edge near the cooling air exit holes.

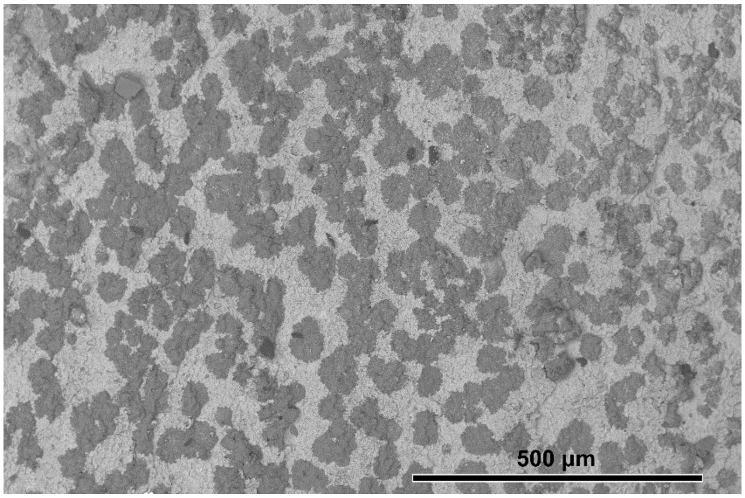

Figure 13. Plan view of deposits (dark circles) on the pressure side of the airfoil of Blade A2

Table 2. Table 2. EDS composition (at%) of deposits by location. Amount of constituents greater than 10% are bolded for emphasis.

	Airfoil	Cooling Channel	Beneath Platform
Al	2.2	**10.4**	**10.0**
Ca	0.1	**15.5**	**13.8**
Co	2.8	0.2	**11.5**
Cr	0.9	0.9	2.6
Fe	6.8	**11.0**	9.5
K	0.1	1.8	0.1
Mg	0.2	6.0	1.6
Na	**60.6**	**17.7**	**10.5**
Ni	1.8	1.0	**17.4**
S	**23.8**	**15.3**	5.9
Si	0.6	**19.1**	**16.6**
Ti	0.2	1.0	0.6

The foreign material extracted from the cooling channels of blade A2 differed from that from beneath the platform of blade A4. The material from the cooling channel was red due to the presence of hematite (Fe_2O_3) while the deposits beneath the platform were black due to the presence of magnetite (Fe_3O_4). Figure 14 shows the XRD patterns of these same cooling channel deposits (top) and under-platform deposits (bottom). Peaks of SiO_2 (quartz and low cristobalite) and $CaSO_4$ were present in both deposits. The cooling channels uniquely show CrS_x and mixed Na/Ca sulfate deposits, while deposits from under the platform contain $Fe_{1-x}S$ and detectable amounts of cubic NiO/CoO. Note that there are comparatively small amounts of Na-containing phases compared to these other compounds. SEM showed that both deposits consist of a mixture of discrete particles ≤ 10 µm in diameter. Table 2 shows EDS comparison of approximately 250 µm^2 area of each deposit powder compared to the airfoil deposits discussed previously. The cooling channel and platform compositions are consistent being oxides, sulfides, and/or sulfates of Ca, Mg, Fe, Al, and Si, along with Na_2SO_4 and K salts. The airfoil deposits are mostly Na_2SO_4.

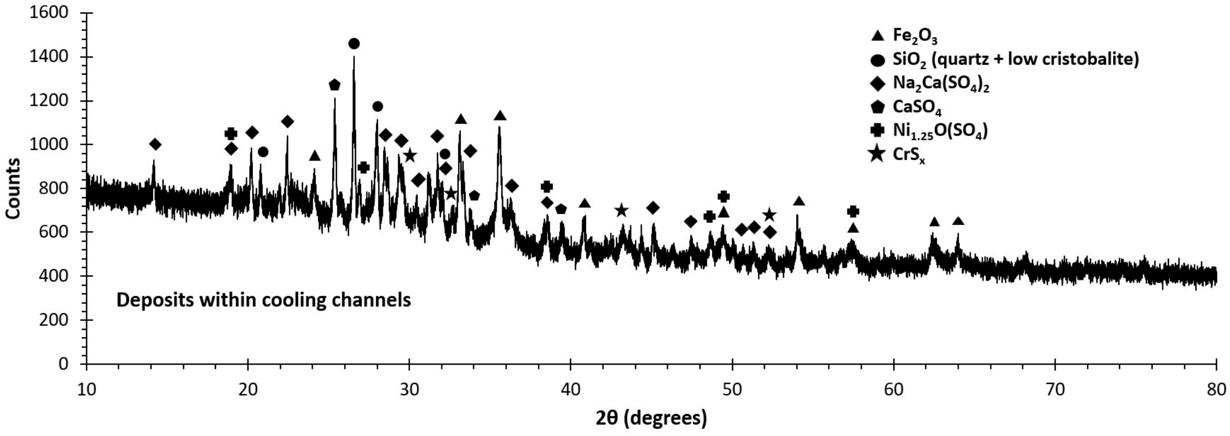

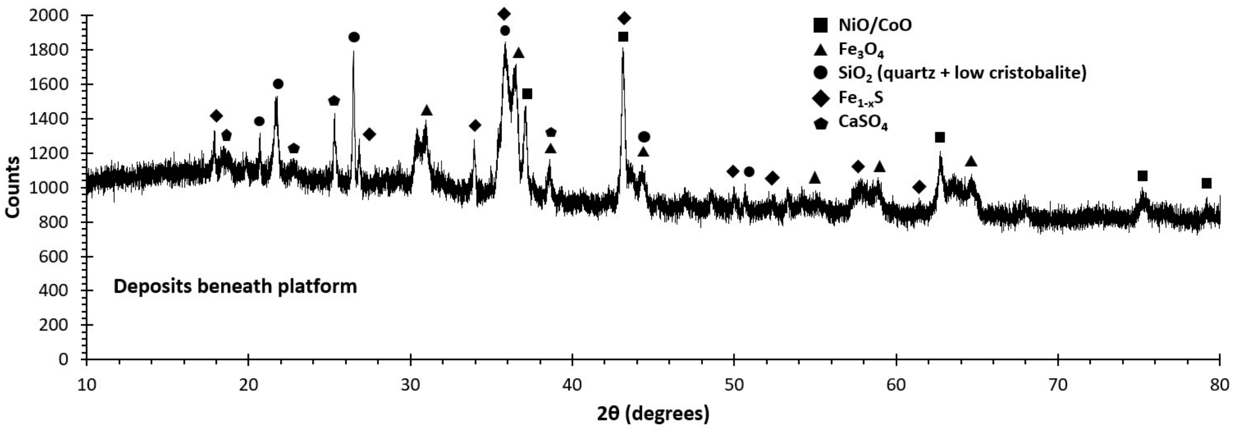

Figure 14. XRD patterns of deposits from cooling channel (top) and beneath the platform (bottom). Note the presence of Fe_2O_3 *within the cooling channel and* Fe_3O_4 *beneath the platform.*

ICP-OES Results

The results of the ICP-OES analysis of water soluble deposits from the top 1mm of blade A1 are shown in Figure 15. Use of ICP-OES is qualitative as the water digestion followed by HCl addition likely underrepresents water-insoluble species. Ca, Mg, Al, and Si concentrations are at least as great as soluble metal (i.e. salts of Ni, Co, and Cr) species. Note that both the exterior airfoil and the interior cooling channel surfaces were exposed to the digestion solution. The orange bars are the expected intensities based on the composition of ASTM D1141 artificial ocean water [57]. The solution has the expected Na^+, K^+, and Ca^{2+} concentrations for seawater but is relatively deficient in Mg^{2+}.

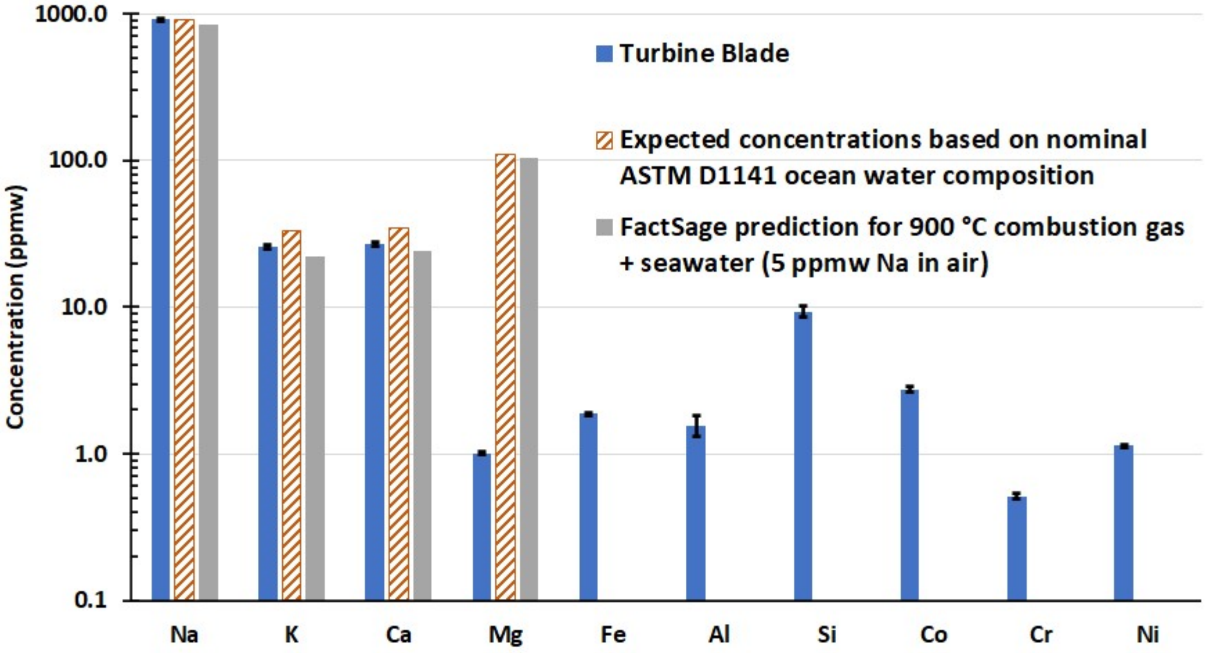

Figure 15. ICP-OES results of the digested Blade A1 deposits. Error bars are ± 1 standard deviation of 3 repeats of same solution. Shaded orange bars are expected concentrations based on the composition of ASTM D1141 artificial ocean water.

Thermochemical Calculations

The composition of the air, fuel, and sea spray streams used in the FactSage calculation are shown in Table 3. Table 4 shows the Equilib module results for both the combustion gas stream and the cooling channel gas stream for 5 ppmw Na in air. Solid sulfates of Na, Mg, Ca, and K are predicted to form in the combustion stream at 700 °C. Note that these calculations assume pure substances; the condensed phases may actually be in solid solution with each other. A thermodynamic assessment by Du shows that K_2SO_4, $CaSO_4$, and $MgSO_4$ have extensive solubility in hexagonal Na_2SO_4 [58], enough that the sulfates observed here could form a single hexagonal phase with significant ionic disorder. At 900 °C the Na_2SO_4 is predicted to melt as expected, and the pSO_3 decreases, converting $MgSO_4$ to MgO. Condensed phase chlorides are not predicted in either scenario and instead most Cl is present as HCl (g). With the exception of Mg species, the ratio of cations matches the experimental ICP-OES results within an order of magnitude.

Table 3. Compositions of seawater, fuel, and air streams used as input for FactSage equilibrium calculations

ASTM D1141 Seawater	
Species	Mass fraction
NaCl	2.37E-02
$MgCl_2$	5.02E-03
Na_2SO_4	3.95E-03
$CaCl_2$	1.12E-03
KCl	6.71E-04
$NaHCO_3$	1.94E-04
KBr	9.75E-05
H_3BO_3	2.61E-05
$SrCl_2$	2.41E-05
NaF	2.90E-06
H_2O	9.65E-01

F-76 Marine Diesel*	
Species	Mass fraction
C	8.57E-01
H	1.38E-01
N	5.95E-04
S	1.00E-03

*With 0.1 wt% S

Air	
Species	Mass fraction
N_2	7.55E-01
O_2	2.32E-01
Ar	1.30E-02

Salts of Na, Mg, and Ca are also predicted for the cooling channel. Surprisingly, the composition is mostly NaCl(s). In the gas phase, NaCl(g) and KCl(g) concentrations are significantly higher and pNaCl now exceeds pHCl. Potassium-containing sulfates are not present as nearly all K is in KCl(g). However, Mg and Ca sulfates remain. The calculation was repeated for both greater S content (equivalent amount of S in 0.1 wt% marine diesel, but excluding C, H, and N) and a lower seawater content (1 ppmw Na in air) and the results are shown in Table 5. The results for 5 ppmw Na and 1 ppmw Na are nearly identical except that all NaCl(s) volatilizes at 1 ppmw Na. This shows that under variable sea salt ingestion, NaCl may be stable only for transient moments. NaCl will volatilize in this environment when the gas stream is not saturated with NaCl(g), leaving behind deposits richer in Mg and Ca salts. The presence of NaCl(s), NaCl(g), and KCl(g) in the cooling channels is an effect of the relatively S-poor environment in the absence of fuel combustion. The results for increased S content show that S reduces NaCl and KCl and increases amounts of their corresponding sulfates. MgO/$MgSO_4$ and $CaSO_4$ are significantly less sensitive to the S content of the gas as they do not form chlorides as readily.

2.1.5 Discussion

The corrosion morphologies and locations are consistent with previous analysis of marine gas turbine blades performed by Shifler [59]. Corrosion within cooling channels and beneath the platform was comparatively more severe than corrosion on the airfoil. The worst location was beneath the platform, with a penetration depth approaching 1 mm and significant corrosion-induced cracking. EDS and XRD show that the deposits associated with this attack are rich in Ca, Mg, Fe, Al, and Si species and relatively poor in Na_2SO_4. These mixtures of oxides, sulfates, and sulfides in the cooling channels and beneath the platforms bear a similarity to CMAS in cation species. However, XRD analysis shows no amorphous phases and SEM shows discrete particles indicating that melting and solidification of a glass has not occurred. XRD, SEM, and ICP-OES are consistent with these particles being ingested sand or dust. This indicates that these deposits likely have the same origin as CMAS, but the service temperatures were not high enough to convert them to molten CMAS glass. Solid particulate ingestion is expected at the relatively low operating temperatures of marine gas turbines compared to aircraft engines. Despite not converting to molten

CMAS, this crystalline particulate mixture is corrosive, leading to the consumption of hundreds of micrometers of metal. Possible mechanisms are discussed below.

Table 4. Calculated equilibrium compositions for turbine environments at 15 atm with 5 ppmw Na in air from seawater. Only gases with fugacity $\geq 10^{-6}$ atm are shown. Compounds containing Na and Cl are in bold for comparison.

Combustion Stream 900 °C		**Combustion Stream 700 °C**		**Cooling Channel Stream 700 °C**	
Gas Phase		**Gas Phase**		**Gas Phase**	
Species	Fugacity (atm)	Species	Fugacity (atm)	Species	Fugacity (atm)
N_2	1.1E+01	N_2	1.1E+01	N_2	1.2E+01
O_2	2.2E+00	O_2	2.2E+00	O_2	3.1E+00
CO_2	6.1E-01	CO_2	6.1E-01	Ar	1.4E-01
H_2O	5.9E-01	H_2O	5.9E-01	H_2O	1.1E-02
Ar	1.4E-01	Ar	1.4E-01	NO	3.9E-04
NO	2.2E-03	NO	3.2E-04	NO_2	9.7E-05
SO_2	1.5E-04	SO_3	1.7E-04	**NaCl**	**2.9E-05**
NO_2	1.3E-04	**HCl**	**1.1E-04**	**HCl**	**2.1E-05**
HCl	**1.0E-04**	SO_2	4.5E-05	**$(NaCl)_2$**	**1.1E-05**
SO_3	7.2E-05	NO_2	6.7E-05	**KCl**	**1.9E-06**
OH	9.3E-06				
Condensed Phases		**Condensed Phases**		**Condensed Phases**	
Species	Deposit mole fraction	Species	Deposit mole fraction	Species	Deposit mole fraction
Na_2SO_4 (l)	**7.9E-01**	**Na_2SO_4 (s)**	**8.0E-01**	**NaCl (s)**	**6.9E-01**
MgO (s)	1.6E-01	$MgSO_4$ (s)	1.5E-01	MgO (s)	2.05E-01
$CaSO_4$ (s)	3.5E-02	$CaSO_4$ (s)	3.5E-02	**Na_2SO_4 (s)**	**7.13E-02**
$K_2Mg_2(SO_4)_3$ (s)	1.2E-02	$K_2Mg_2(SO_4)_3$ (s)	1.7E-02	$CaSO_4$ (s)	3.7E-02
Moles deposit / system total	3.8E-06	Moles deposit / system total	3.9E-06	Moles deposit / system total	3.5E-06

Table 5. Calculated equilibrium compositions for cooling channel gas streams (air + sea water) at 700 °C and 15 atm. The S content of the middle column is the fuel S without the other components (C, H, and N) in order to show the effects of S only. Corresponding results for 5 ppmw Na are repeated from Table 4 for comparison. Only gases with fugacity $\geq 10^{-6}$ atm are shown. Compounds containing Na and Cl are in bold for comparison.

Cooling Channel Stream 5 ppmw Na		**Cooling Channel Stream 5 ppmw Na + S**		**Cooling Channel Stream 1 ppmw Na**	
Gas Phase		**Gas Phase**		**Gas Phase**	
Species	Fugacity (atm)	Species	Fugacity (atm)	Species	Fugacity (atm)
N_2	1.2E+01	N_2	1.2E+01	N_2	1.2E+01
O_2	3.1E+00	O_2	3.1E+00	O_2	3.1E+00
Ar	1.4E-01	Ar	1.4E-01	Ar	1.4E-01
H_2O	1.1E-02	H_2O	1.1E-02	H_2O	2.2E-03
NO	3.9E-04	NO	3.9E-04	NO	3.9E-04
NO_2	9.7E-05	SO_3	1.8E-04	NO_2	9.7E-05
NaCl	**2.9E-05**	**HCl**	**1.1E-04**	**NaCl**	**1.3E-05**
HCl	**2.1E-05**	NO_2	9.7E-05	**HCl**	**4.2E-06**
$(NaCl)_2$	**1.1E-05**	SO_2	3.9E-05	**$(NaCl)_2$**	**2.1E-06**
KCl	**1.9E-06**				
Condensed Phases		**Condensed Phases**		**Condensed Phases**	
Species	Deposit mole fraction	Species	Deposit mole fraction	Species	Deposit mole fraction
NaCl (s)	**6.9E-01**	**NaCl (s)**	**0.0E+00**	**NaCl (s)**	**0.0E+00**
MgO (s)	2.05E-01	**Na_2SO_4 (s)**	**8.0E-01**	**Na_2SO_4 (s)**	**2.3E-01**
Na_2SO_4 (s)	**7.13E-02**	$MgSO_4$ (s)	1.5E-01	MgO (s)	6.5E-01
$CaSO_4$ (s)	3.7E-02	$CaSO_4$ (s)	3.5E-02	$CaSO_4$ (s)	1.2E-01
		$K_2Mg_2(SO_4)_3$ (s)	1.7E-02		
Moles deposit / system total	3.5E-06	Moles deposit / system total	3.9E-06	Moles deposit / system total	2.2E-07

ICP-OES, EDS, XRD, and the thermochemical calculations together suggest the likely compositions. Chlorine, which would originate from seawater, was almost entirely absent from EDS spectra and the powder diffraction patterns had no peaks from chloride phases. Therefore, what little Na and K condensed species are present are probably sulfates, while Cl was likely present only in gaseous species such as NaCl(g) or HCl(g). In Figure 15, ICP-OES shows that the digested deposit solution was relatively poor in Mg^{2+} despite having the concentrations of Na^+, K^+, and Ca^{2+} expected from seawater. This can be explained with the Ellingham Diagram in Figure 16, which shows that Na_2SO_4, K_2SO_4, and $CaSO_4$ are the most stable sulfates with respect to their corresponding oxides. These species would be soluble in the water digestion. $MgSO_4$ and the transition metal sulfates are relatively less stable, suggesting they would more likely be present as insoluble oxides and thus be deficient in the analyzed solution. Indeed, the concentrations of these metal cations are all less than 10 ppm. The predominance diagram in Figure 17 shows that a greater pSO_3 is required for $MgSO_4$ than $CaSO_4$ and, by extension, Na_2SO_4 and K_2SO_4. A minimum pSO_3 concentration for the formation of $MgSO_4$ at 700 °C is on the order of 10^{-4} atm while calculations for 900 °C indicate $MgSO_4$ requires $pSO_3 \geq 10^{-2}$ atm.

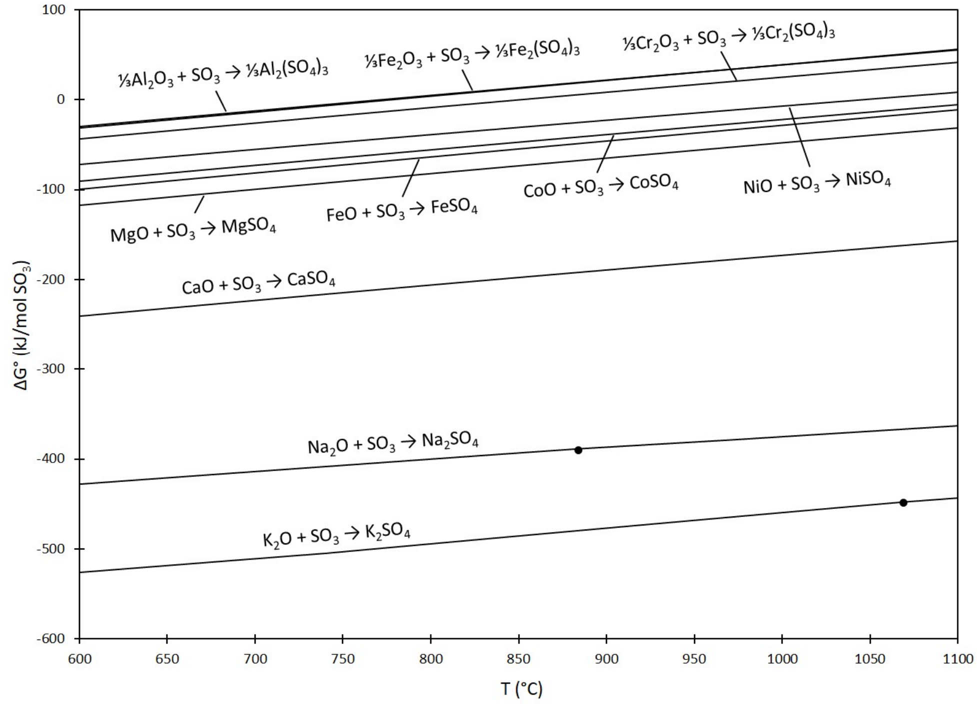

Figure 16. Ellingham diagram for sulfates relative to their corresponding oxides. The melting points of Na_2SO_4 and K_2SO_4 are indicated by circles.

The thermochemistry and limited water solubility in the ICP-OES solution of Si, Al, and Fe suggest that these are primarily present as oxides. XRD shows SiO_2 (quartz and low cristobalite), hematite (in the cooling channels), and magnetite (beneath the platform), as shown in Figure 14. This is consistent with the visual appearance of the deposits (red in the case of hematite, black for magnetite). The presence of hematite in the cooling channels and magnetite below the platform suggests a difference in pO_2 between these two turbine blade environments, with the cooling channels being a more oxidizing environment. The reaction between O_2, magnetite, and hematite is shown in Equation 15, which has an equilibrium pO_2 of approximately 1×10^{-12} atm at 700° C and 3×10^{-8} atm at 900° C as calculated with FactSage.

$$2\mathrm{Fe_3O_4(s)} + \frac{1}{2}\mathrm{O_2(g)} \leftrightarrow 3\mathrm{Fe_2O_3(s)} \tag{15}$$

Thus, the pO_2 conditions beneath the platform must be more reducing ($< 10^{-8}$ atm)

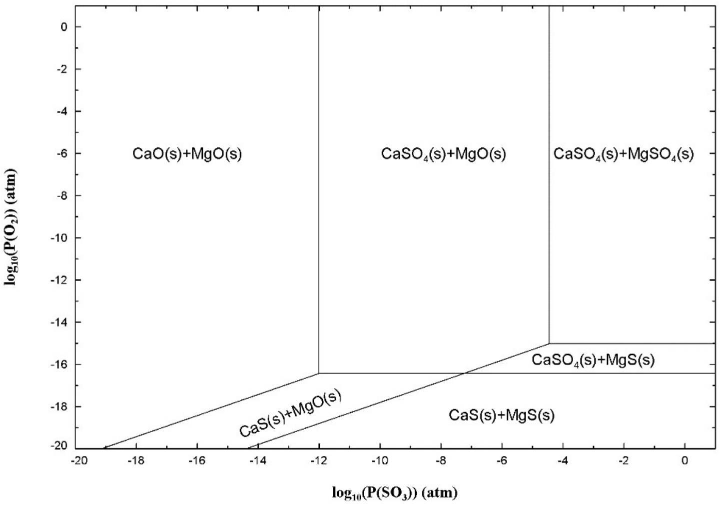

Figure 17. Predominance diagram for the Ca-Mg-O-S system at 700° C. $CaSO_4$ is stable over a larger pSO_3 range than $MgSO_4$. The diagram for 900° C is similar but $MgSO_4$ is stable at only $pSO_3 \geq 10^{-2}$ atm.

The lack of significant Na_2SO_4 in these deposits is consistent with the kinetics of its formation being slow compared to the deposition rate of ingested sand particles. Table 4 shows that Na_2SO_4 is clearly a thermodynamically favorable product of ingested seawater in the combustion stream. However, calculations do not account for the kinetics of Na_2SO_4 formation or sand ingestion, neither of which are easily modeled. The analysis of Table 4 is more applicable to the airfoil surface, where deposits are mostly Na_2SO_4. The airfoil is less likely to trap sand and dust particulates, compared to the platform and cooling channels, simply due to geometry. Therefore, the literature on Na_2SO_4 deposition and corrosion mechanisms remains relevant in the case of marine gas turbine blade airfoils [60]. Indeed, the corrosion morphology on the airfoil, as shown in Figure 8, is more reminiscent of low temperature hot corrosion pitting. This combined with the composition of the deposits in Table 2 suggests relatively well-understood mechanisms such as the localized formation of a Na_2SO_4-$NiSO_4$-$CoSO_4$ eutectic melt [16,34,54,55].

Tschinkel [61] characterized the compositions of aircraft turbine blade airfoil deposits and found higher concentrations of Ca^{2+} than in the airfoil deposits of this study. Tschinkel's Ca^{2+} concentrations are also higher than that expected from seawater as a deposit source, but not as high as in the CMAS-like deposits in this study. He explains this may be due to ingestion of Ca-rich dust and concrete particles on the runway. He also notes that $CaSO_4$ is stable up to higher temperatures than other alkali sulfates such as Na_2SO_4 and K_2SO_4, which more readily decompose and/or volatilize as aircraft engine temperatures approach 1000-1100 °C. Cycling engine temperatures to this regime will concentrate Ca^{2+} as Na^+ and K^+ compounds tend to volatilize and decompose. It is likely that engine temperatures of the shipboard turbine of this present study are lower ($\leq$ 925 °C) and thus Ca^{2+} is not concentrated on the airfoils as it is in aircraft engines. These findings illustrate that deposit Na_2SO_4 concentrations vary with service conditions. Higher temperatures, such as those in an aircraft engine, may concentrate Ca-containing compounds by volatilization of Na- and K-containing species while at the lower temperatures in a marine gas turbine, deposits with high Ca/Na ratios are more likely to derive from sand ingestion.

The mechanisms governing corrosion beneath the platform and within the cooling channels are perhaps less understood. It is likely that sulfates in a physical mixture with this crystalline CMAS-like deposit could melt while the other components (particularly SiO_2, Al_2O_3, and the iron oxides) remain solid. Additions of Na_2SO_4 to CMAS deposits may lower the CMAS melting temperature to approximately 1025 °C [50], so only the sulfate compounds may be molten at ≤ 925 °C. While the hot corrosion induced by Na_2SO_4 is a widely studied problem, the effects of mixed deposits like those observed here is not well studied. Metal oxides are soluble in molten Na_2SO_4 and may shift the acid-base equilibrium of the salt (per Equations 11 and 12) [21]. This oxide dissolution could affect the corrosion mechanism (i.e. make acidic- or basic-fluxing predominate) or cause synergistic fluxing of oxides, whereby the dissolution of one oxide shifts the acid-base equilibrium to a regime where another oxide exhibits high solubility [62,63].

Figure 18 is a plot of solubility of various oxides in molten Na_2SO_4 as a function of basicity ($-\log a_{Na2O}$) at 900 °C [21,55,64–66]. As seen in Figure 18, much of the work on oxide solubility focuses on oxides of alloying elements (e.g. Ni, Co, Cr, Al, Fe, etc.). This is because previous work studied the synergistic effects of oxides from the oxidation of alloys [21,67], rather than effects of oxides from environmental deposits. Because of this, solubilities of MgO (and, although less likely, CaO) in fused Na_2SO_4 have not been determined, although according to periodic trends it is expected that the dissolution of basic Ca and Mg oxides would promote basic fluxing. This change may explain the significant difference in corrosion morphology between the airfoil in Figure 8 (little Ca and Mg in deposits) and the cooling channel in Figure 10 (Ca- and Mg-rich deposits). However, some of the difference may also be explained by the different materials (CoNiCrAl on the exterior and uncoated Mar-M 247 in the cooling channels).

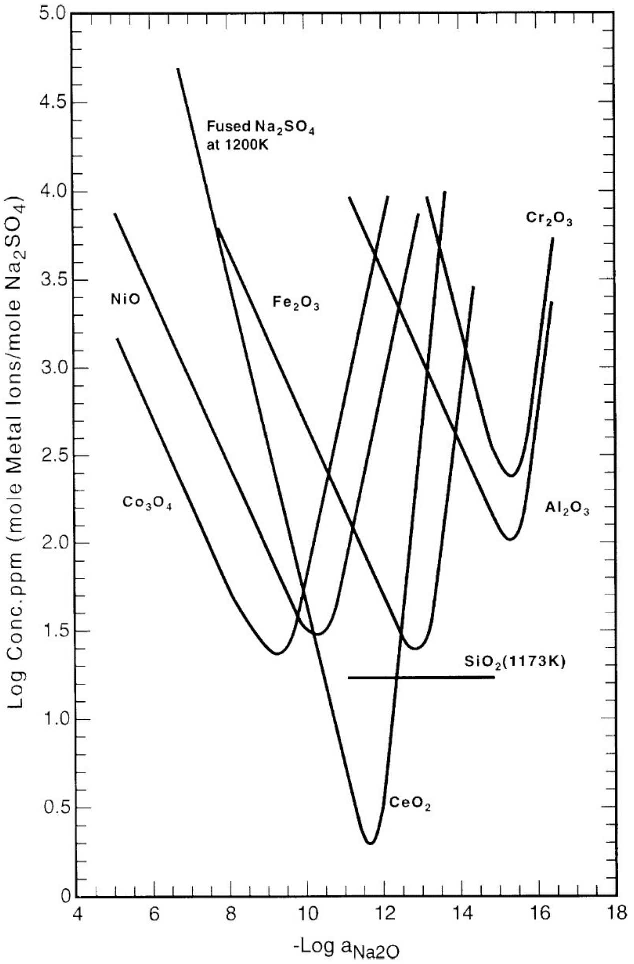

Figure 18. Solubility of oxides in Na_2SO_4 as a function of basicity (-log aNa_2O). From [10], [16], [31]-[33]. Reprinted from “Hot corrosion of materials: a fluxing mechanism?” 211, Copyright (2002) [21]*, with permission from Elsevier.*

Studies of Ca- and Mg-rich deposits inducing corrosion at relatively low temperatures are sparse. Chiang, Meier, and Perkins observed that above 850° C deposits of CaO and MgO attack Cr_2O_3-forming alloys by enhancing CrO_3 evaporation [68], although $CaSO_4$ had little effect. Al_2O_3-forming alloys suffered similar amounts of corrosion in the presence of CaO, which the authors attributed to interactions with the Cr_2O_3 formed during transient oxidation. Nagarajan, Smith, and Wright observed that nickel-base alloys are susceptible to severe corrosion, including enhanced sulfidation and scale spallation, when coated with solid deposits of CaO-$CaSO_4$, CaS-CaO, and CaS-$CaSO_4$ at 900° C and within a pO_2 range of 10^{-11}-10^{-13} atm [69]. Gheno, Gleeson, and Meier recently investigated the effects of CaO and/or $CaSO_4$ deposits on corrosion [70–72], but at higher temperatures (1100 °C) than are expected to occur within marine gas turbines. At 1100 °C, the dominant corrosion mechanism involves molten Ca chromates, which are likely solid at marine turbine temperatures. None of these studies investigate the presence of complex crystalline CMAS mixtures at lower (600-900 °C) temperatures. These effects demand further study, especially because these deposits are associated with regions of greatest metal loss.

Two mechanisms have been previously mentioned that lead to deposits with increased Ca and Mg content. One is ingestion and deposition of sand/dust particles and another is volatilization of Na_2SO_4 at high temperatures. The FactSage analysis suggests a third mechanism due to decreasing S content of the gas stream. With the low S concentrations in the cooling channels, equilibria shift to favor NaCl at the expense of Na_2SO_4. The NaCl volatilizes readily and Table 5 shows that all of it may become NaCl(g) whenever the seawater contaminant ingestion rate is low. $CaSO_4$, $MgSO_4$, and MgO, whether present from seawater or sand ingestion, do not form volatile chlorides as readily and thus conditions favor Ca- and Mg-rich deposits. Well-understood Na_2SO_4-induced hot corrosion processes are still relevant in some cases (i.e. lower-temperature marine turbine blade airfoils), but the thermochemistry, case studies, and industry trends all indicate that Ca-rich corrosive deposits are relevant as well.

One hypothesis for the corrosivity of the Mg- and Ca-rich deposits is that MgO and CaO may react with $SO_3(g)$ in the gas turbine environment, as shown previously in Equation 13. Ingested sand or dust may therefore enrich Na_2SO_4 deposits with greater amounts of $MgSO_4$ and $CaSO_4$. $MgSO_4$ and $CaSO_4$ enrichment would lower the melting temperature of the deposit [50,73], resulting in greater corrosion. Ingested sand/dust therefore may be corrosive at temperatures far below those at which CMAS glass forms because these contaminants contain CaO and MgO, which may react to form sulfate mixtures and promote melting. The hypothesized effect of MgO/$MgSO_4$ is the subject of the experimental studies.

2.1.6 Summary and conclusions

Degraded shipboard turbine blades were characterized with an emphasis on investigating the relevant corrosive deposits and implications for corrosion mechanisms. The greatest metal loss occurred beneath the platform and within the cooling channels because these are areas susceptible to accumulation of solid deposits (in addition to difficulties in coating application with poor line-of-sight). Crystalline, solid CMAS deposits formed in these locations from ingestion and accumulation of sand or dust. The oxides in the deposits deposits remain solid and crystalline because the operating temperature was lower than that required to form molten CMAS glass, although sulfates in the deposit may melt. Characterization and thermochemical calculations indicate the Si, Al, and Fe are present as oxides while Ca, Na, and K are present as sulfates. Mg may be in the form of either MgO or $MgSO_4$, depending on the pSO_3. Despite operating temperatures being too low to cause CMAS melting and glass formation, these environments resulted in significant corrosion beneath the platform that initiated cracking. It is hypothesized that the Mg- and Ca-rich deposits may contain $MgSO_4$ and/or $CaSO_4$, locally lowering the melting temperature of the deposit. The severity of the corrosion and the lack of literature on such mixed cation sulfate/oxide deposits at relatively low temperatures (≤ 700 °C) motivates the experimental studies of this dissertation in sections “4.0 Burner rig and furnace LTHC exposures” and “5.0 Deposit formation.”

3.0 Research objectives

The characterization of corroded marine turbine blades demonstrated that actual gas turbine service conditions are much more complex than a simple two-mode HTHC-LTHC Na_2SO_4 model can describe. Sulfates of Mg, Ca, and K from seawater may be present as well as CMAS and other oxides from the ingestion of dirt, sand, and/or dust. The corrosive deposits are made even more complex when sulfation of multicomponent alloys is considered. This is especially relevant for LTHC because melting and corrosion are dependent upon the formation of low melting point/eutectic mixtures. The LTHC studied in this dissertation is of this mixed-deposit corrosion, different from the LTHC by pure Na_2SO_4 shown in Figure 5.

The effect of mixed Na-Mg-containing deposits is of particular interest due to the abundance of $MgCl_2$ in seawater (see Table 3) and the Na_2SO_4-$MgSO_4$ eutectic of 666 °C. The first objective of the present study is to answer the question "Do mixed Na_2SO_4-$MgSO_4$ deposits cause more severe LTHC than pure Na_2SO_4 deposits?" Burner rig and furnace exposures of model alloys to both mixed and pure Na- and Mg-containing deposits will be conducted so that the role of mixed Na-Mg-containing salts may be determined.

The second objective is to answer the research questions "What are the effects of varying alloy composition and phase fractions on LTHC in the presence of complex Mg-containing deposits? Which alloying elements react and become incorporated into the deposit salt mixture?" This is connected to the first research question because sulfation of oxides from both the environment and alloy governs deposit chemistry and therefore deposit melting alloy corrosion. This second research question will be addressed in the same chapter as the first by varying alloy composition in addition to the deposit composition.

The third research question is “How do the complex, multicomponent deposits form from the combustion gases?” Because the composition of multicomponent deposits is significant, understanding the processes that lead to their formation and deposition is as well. The thermodynamics and kinetics of deposit formation will be investigated and related to the resulting mixed-deposit LTHC.

Lastly, prior models and previous understanding will be extended to more complex deposits containing CMAS and to more complex material systems including multilayer coatings systems. These are preliminary findings to demonstrate methods for understanding materials corrosion induced by multicomponent deposits that can be utilized for complex service environments.

4.0 Burner rig and furnace LTHC exposures

4.1 Introduction

The deposits encountered in engineering service are more complex than just pure Na_2SO_4, as demonstrated previously in section 2.1.4. For marine gas turbine applications, the concentrations of salts other than NaCl must be considered. Table 6 shows the concentration of ASTM D1141 artificial ocean water [57]. Seawater contains 4 primary cations: Na^+, Mg^{2+}, Ca^{2+}, and K^+. Of these, Mg^{2+} is the second-most abundant at greater than 10% $[Na^+]$. This ASTM standard is intended as an average seawater composition. Actual seawater composition and hardware deposit composition vary by geographic location, and therefore some deposits may contain greater or lesser amounts of Mg salts [51,74,75]. Bornstein has suggested that the $MgSO_4$ content of deposits in marine gas turbines may reach as high as 30 mol% [76].

Table 6. Composition of ASTM D1141 artificial ocean water [57]

Compound	NaCl	$MgCl_2$	Na_2SO_4	$CaCl_2$	KCl	$NaHCO_3$	KBr	H_3BO_3	$SrCl_2$	NaF
Conc. (g/L)	24.53	5.20	4.09	1.16	0.695	0.201	0.101	0.027	0.025	0.003

The existing literature contains few studies on the effects of Mg on hot corrosion and no clear conclusions may be drawn from them. Tang and Gleeson have reported that a Na_2SO_4-$MgSO_4$ mixture increased the corrosion rate of PWA 1484 by as much as 3 times that of pure Na_2SO_4 [51,75]. This led Shifler to conclude that "A mixture of $MgSO_4$ and Na_2SO_4 promotes accelerated Type II hot corrosion at 700 °C because the eutectic salt mixture melts at 666 °C" [51]. Indeed, Figure 19 [58] shows that a eutectic occurs at roughly 50 mol% $MgSO_4$ and would allow melting of the deposit even in the absence of NiO/CoO sulfation. However, Jones and Williams report that a 50-50 mol% Na_2SO_4-$MgSO_4$ mixture on CoCrAlY substrates at 700°C resulted in half the amount of corrosion from pure Na_2SO_4 [77]. Lowell, Sidik, and Deadmore performed extensive statistical analysis on burner rig data showing that the presence of Mg decreased observed corrosion rates for a variety of alloys at 900-1050 °C [78]. They noted that Mg tended to deposit in burner rigs as MgO rather than $MgSO_4$. Clearly, the effect of Mg in corrosive seawater-derived deposits on alloy corrosion remains unclear.

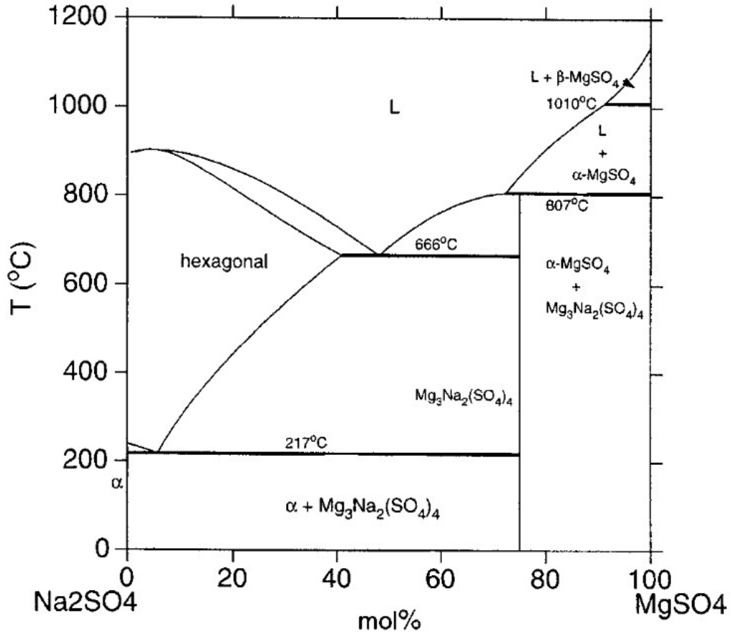

Figure 19. Assessed Na_2SO_4-$MgSO_4$ pseudobinary phase diagram showing a eutectic temperature of 666 °C at roughly 50 mol%. Reprinted by permission from Springer Nature Customer Service Centre GmbH: Springer Journal of Phase Equilibria "Thermodynamic assessment of the K_2SO_4 -Na_2SO_4-$MgSO_4$-$CaSO_4$ system" by Du, H., Copyright (2000) [58].

Even the nature of Mg-containing deposits, whether they exist as MgO or $MgSO_4$ in gas turbines at 700 °C, remains uncertain. Thermochemical analysis shown in Table 4 suggests that it is present at $MgSO_4$ at 700 °C and MgO at 900 °C. This is consistent with the Lowell, Sidik, and Deadmore observations of MgO at 900-1050 °C [78]. However, Jones and Williams did not perform their exposures in a burner rig and applied the deposits directly by spraying a water solution. It is not clear how any of these experimental methods compare to the actual deposition process in a gas turbine and whether this affects the chemical form, structure, and resulting effects on corrosivity of Mg-containing deposits.

Of course, hot corrosion cannot be understood by investigation of the environment and deposits alone. The engineering materials must be understood. Only then can knowledge of both material and environment be combined to understand their interaction. As mentioned previously, LTHC is emphasized because the most significant corrosion on marine turbine blades was observed beneath the platform and within cooling channels, which are locations of relatively low operating temperatures. For LTHC, transient oxidation and the third element effect play a significant role. The third element effect and transient oxidation affect the relative amounts of deleterious NiO/CoO (and subsequent $NiSO_4$/$CoSO_4$ required for a eutectic) and beneficial Cr_2O_3/Al_2O_3 that form [67,79]. Cr is known to be particularly beneficial for most Ni- and Co-base alloys in LTHC conditions [36], possibly because of the reduction of transient oxidation [27,80]. However, outstanding questions remain on the exact mechanisms of LTHC, especially compared to present knowledge on HTHC. The oxide scale is presumed to be attacked by acidic fluxing in most LTHC environments, but this hypothesis and the effect of changing acidity due to the presence of multiple oxides are still under investigation [63].

There are large knowledge gaps in attempting to extend hot corrosion of model alloys by pure Na_2SO_4 to multicomponent deposits and more complex engineering alloys. The interactions among these multiple components may be significant. Also, there should be renewed appreciation for studying the formation and character of the deposits themselves, without which there would be no hot corrosion.

4.2 Objectives

There are two main experimental objectives for answering questions about the effects of environment composition and material composition on the severity and mechanisms of LTHC. The first is to test the hypothesis that $MgSO_4$ (or MgO if it deposits as the oxide in the LVBR) may accelerate hot corrosion by promoting melting. This was accomplished by performing LVBR and tube furnace exposures with varying amounts of Na_2SO_4 and $MgSO_4$. The second is to examine the roles of varying alloy composition and alloy phase content with three model NiCoCrAlY alloys of varying composition. ICP-OES, SEM, and EDS were used to characterize the dependence of corrosion with alloy composition and to propose explanations of corrosion mechanisms. Together, the analyses of both the deposits and the alloys will allow for greater understanding of multicomponent material-environment interactions.

4.3 Experimental methodology

4.3.1 Materials

Model alloys with the compositions shown in Table 7 were manufactured by Sophisticated Alloys. Starting materials were vacuum induction melted (VIMed) and cast into pins 2.5” tall and 0.125” in diameter (after grinding). All alloys were hot isostatic pressed (HIPed) at 1200 °C and 100 MPa. The compositions in Table 7 were selected on the basis that they occur on the tie lines shown in

Figure 20. This selection of compositions was intended to help distinguish between the effects of alloying element composition and phase content on hot corrosion performance and mechanisms. Alloy 1 and Alloy 2 have similar Al content while Alloy 2 and Alloy 3 have similar Cr content. Note that the 0.125” diameter pins have greater reservoirs of Al and Cr compared to 50-100 µm coatings, and so greater corrosion is expected to occur on NiCoCrAlY coatings in service. The positions of the Alloy 1 and Alloy 2 compositions are such that they are expected to have similar β and γ content while Alloy 3 is richer in β and less rich in γ. All three alloys are primarily Al_2O_3-formers. EDS of alloys oxidized in the absence of corrosive deposits confirms the scales are primarily Al_2O_3 with some Cr_2O_3 (particularly above the γ phase).

Table 7. Compositions of Alloys 1-3 (wt%)

Alloy	Ni	Co	Cr	Al	Y
Alloy 1	27.9	30	30	12	0.1
Alloy 2	43.6	25.6	16.4	14.3	0.1
Alloy 3	36.4	21.4	17.6	24.5	0.1

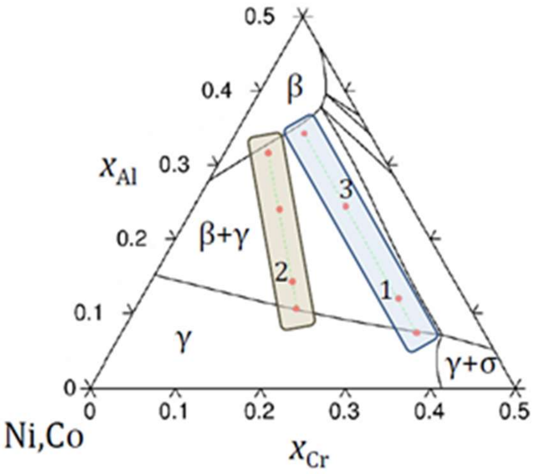

Figure 20. Ni,Co-rich portion of (Ni, Co)-Cr-Al schematic ternary phase diagram showing compositions of Alloys 1-3. Ternary phase diagram provided by Dr. Brian Gleeson.

4.3.2 LVBR exposures

A low velocity burner rig (LVBR), shown in Figure 21, allowed for exposure of samples to corrosive environments similar to those found in gas turbines. The isometric drawing in Figure 22 and the cross-sectional drawing in Figure 23 identify the components of the LVBR. The test samples were upright pins inserted into castable ceramic on a carousel, shown in Figure 24, that rotated at approximately 60 rpm within the furnace test chamber to ensure equal exposure of samples to combustion gases. The furnace test chamber was maintained at 700 °C for all experiments. Air and fuel introduction, combustion, and salt solution contaminant injection all occurred at the burner inlet of the burner duct. F-76 marine diesel doped with 0.5 wt% S was combusted with an air fuel ratio (AFR) of 30:1 by mass. A salt solution contaminant was injected into the gas stream through a 0.0325" ID stainless steel capillary in flowing air with a backpressure of 5 psi for solution atomization. Samples were thermally cycled to room temperature for every 1 of 24 h via removal and reinsertion using the movable carriage illustrated in Figure 25.

Figure 21. Photo of the LVBR

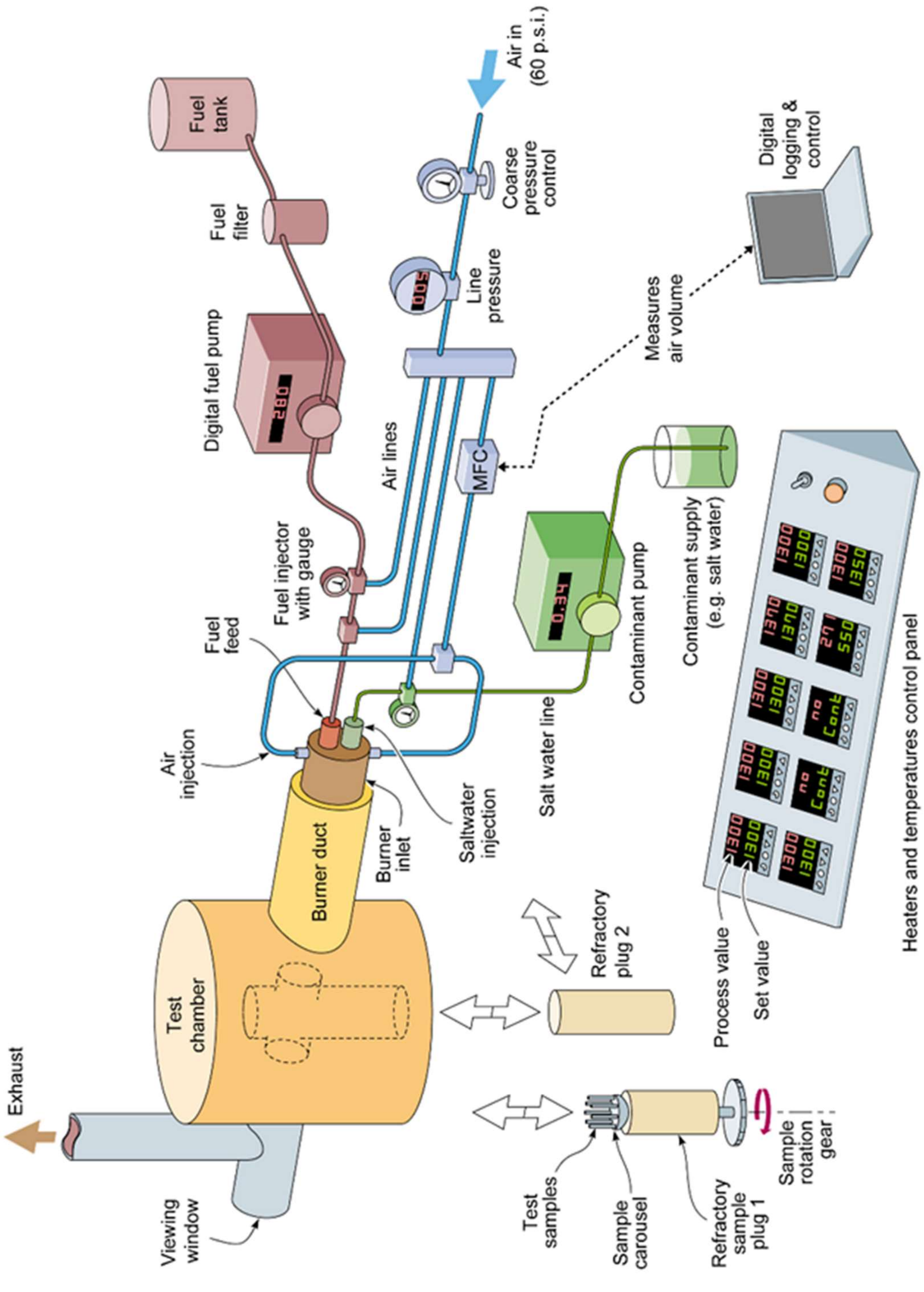

Figure 22. Isometric schematic of the LVBR

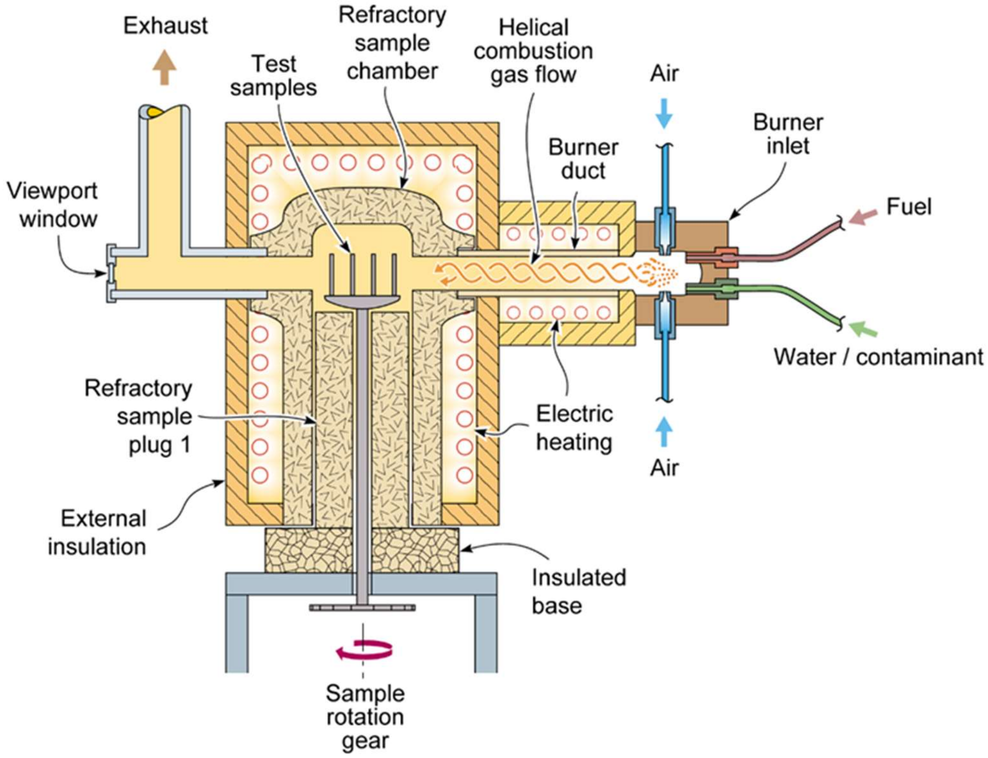

Figure 23. Schematic cross-section of the LVBR

Figure 24. A photo of a carousel containing pin samples embedded in castable ceramic. Each pin is 2.5 in. tall

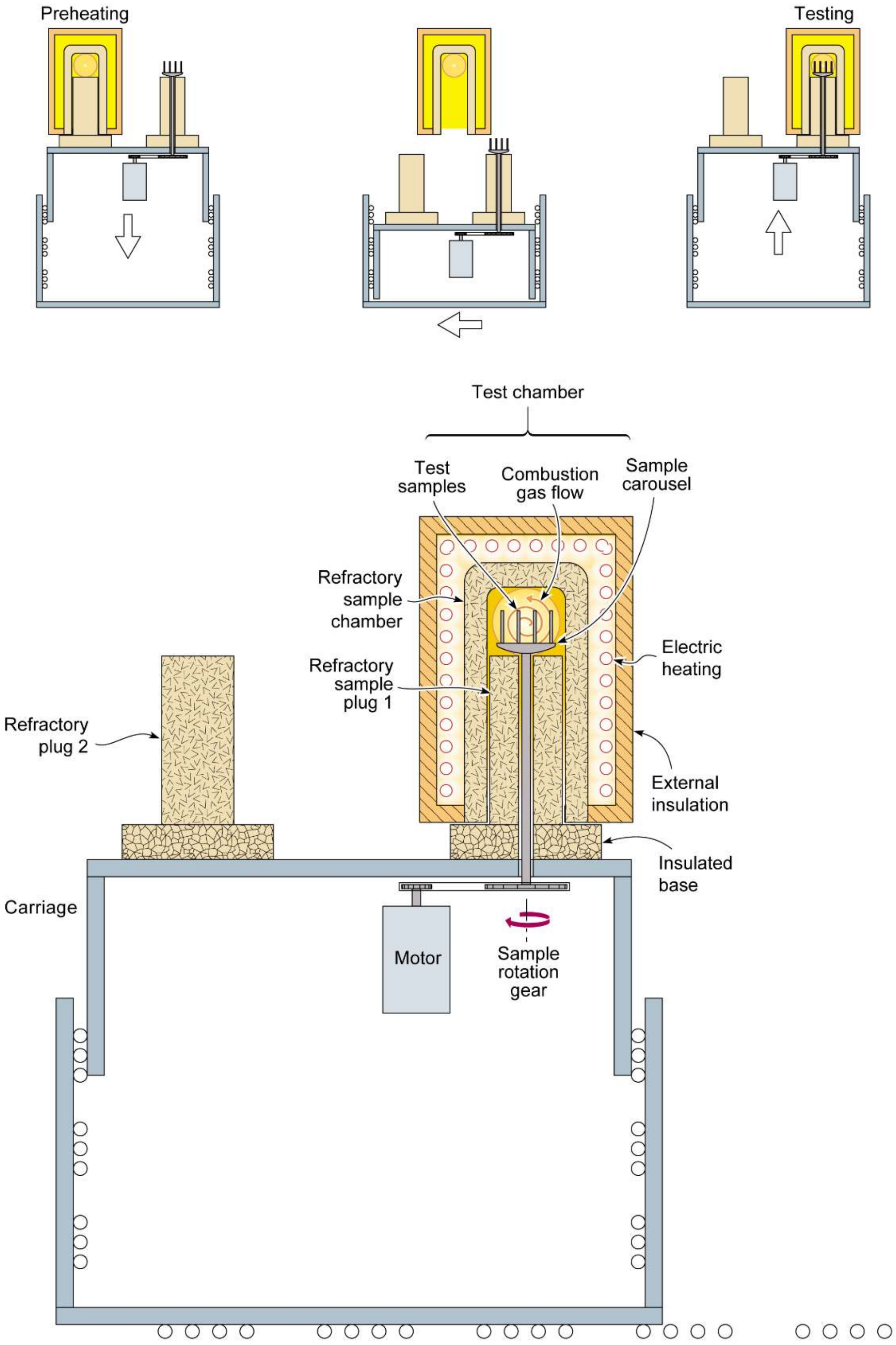

Figure 25. Illustration of automated sample plug removal and insertion

The samples were pins 1/8” in diameter and 2.5” tall. Sample carousels held 27 pins total, including 10 alloy pins (allowing for 3 or 4 samples of each of the three alloys used in the present study), 16 Al_2O_3 pins, and one Pt pin. The Pt pin and Al_2O_3 pins were used as relatively inert substrates for the characterization of deposits in the absence of reactions with alloys. The Pt pin was added to catalyze SO_3 formation and to allow for characterization of differences in deposition between metallic and Al_2O_3 substrates. The samples were mounted on the carousel by inserting the bottom 1 cm of the pins into a castable ceramic. The carousel was then left to harden in lab air for at least 24 hours prior to LVBR exposure. Al_2O_3 pins were removed at various exposure times during the 500 h exposures in order to characterize the time evolution of deposits.

Four different LVBR exposures, each lasting 500 h total, were conducted with four different injected salt solution compositions. The salt solution for the first exposure consisted of ASTM D1141 artificial ocean water [57] (see Table 6 for the composition) diluted by a factor of 20 in order to obtain 5 ppmw Na in the gas stream. The salt solutions for the other three exposures are shown in Table 8. These concentrations were chosen to keep the total molar flow rate of salt cations constant between all four exposures.

Table 8. Compositions of solutions injected into LVBR gas stream

	Concentration (M)	
Run	NaCl	$MgCl_2$
1	0.30	0.00
2	0.00	0.30
3	0.15	0.15

Pump rate: 21.5 ± 1.2 g/h

After LVBR exposures, sample were digested in DI water and characterized by SEM/EDS. The water digestion was performed by inserting the top 4 cm of each pin into 4 mL DI water for 30 min, with the bottom 2 cm remaining above the solution surface to prevent digestion of the sections that were embedded in the castable ceramic.

4.3.3 Tube furnace exposures

LTHC exposures of model NiCoCrAlY alloys were performed to understand the corrosion of alloys in the presence of mixed Na_2SO_4-$MgSO_4$ deposits. A schematic cross-section of the horizontal tube furnace setup is shown in Figure 26. Samples with their deposits were placed on an alumina boat and inserted into the hot section of the furnace, preheated to 700 °C. The temperature in the hot section was monitored with a Type K thermocouple. The gas environment consisted of 0.1 wt% SO_2 in O_2 flowing at 50 sccm through a Pt mesh catalyst to establish an estimated pSO_3 of 3.6×10^{-4} atm. The gases flowed through a dessicant upstream of the furnace to reduce the amount of water vapor. Samples were removed directly from the 700 °C hot zone into room temperature lab air after 48 h of isothermal exposure. The relatively short exposure time of 48 h was selected because the tube furnace testing is an accelerated test compared to the LVBR and gas turbine environments.

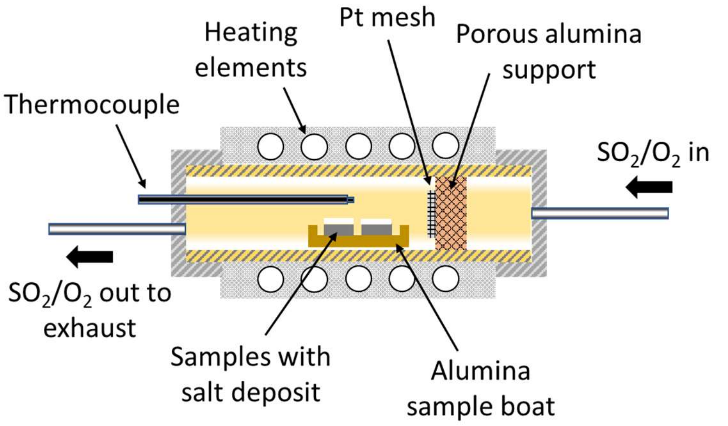

Figure 26. Schematic cross-section of the horizontal tube furnace assembly

The samples were created by sectioning the model alloy pins, resulting in cylindrical button samples 0.125 in. in diameter. An image of salt-loaded samples with in an Al_2O_3 sample boat is shown in Figure 27. Note that the salt loadings were not uniform, but multiple furnace exposures confirmed uniform corrosion morphologies. A thin layer of Na_2SO_4 covers the surfaces even where none is visible in the macro photographs. It is believed that upon melting, the salt deposits wet the sample surfaces uniformly.

Figure 27. Model alloy button samples on a sample boat. Each sample is 0.125 in. in diameter. Note that uniform corrosion was observed despite uneven salt distribution, likely due to the melting of the salt at 700 °C and wetting of the surface

Salt loadings were deposited via pipetting an aqueous salt solution on each sample followed by evaporation in a convection furnace at 104 °C. The pure Na_2SO_4 salt loadings were 2 mg/cm^2, corresponding to approximately 2.8×10^{-5} mol Na^+ per cm^2. Deposit weights of pure $MgSO_4$ and 50-50 mol% Na_2SO_4-$MgSO_4$ were set such that the amount of salt cations remained constant at 2.8×10^{-5} mol/cm^2. Table 9 shows the salt loading compositions used for the tube furnace exposures. After exposure, samples were digested in DI water for ICP-OES analysis and characterized by SEM/EDS. ICP-OES digestion was performed by immersion of the entire button sample into deionized water for 30 min.

Table 9. Compositions of salt deposits applied to NiCoCrAlY samples for tube furnace exposures

	Amount (mol/cm^2)	
Run	Na_2SO_4	$MgSO_4$
1	1.4×10^{-5}	0.00
2	4.6×10^{-6}	9.3×10^{-6}
3	0.00	2.8×10^{-5}

4.3.4 Characterization methods

All scanning electron microscopy, energy dispersive X-ray spectroscopy, and X-ray diffraction were performed at the Nanoscale Materials Characterization Facility (NMCF) at UVA.

4.3.4.1 Scanning electron microscopy and energy dispersive X-ray spectroscopy

Cross sections of samples were prepared using a diamond cutoff wheel. Pins were sectioned at three locations: top (6.5 mm from tip), middle (20 mm from tip), and bottom (40 mm from tip). Cross-sections were ground with 320, 500, and then 1200 SiC paper and polished with 9, 3, 1, and 0.25 μm diamond suspension. Samples that were digested in deionized water for ICP-OES were sectioned and polished using water. Some samples were cut using ethylene glycol and polished using nonaqueous diamond suspensions and lubricants to preserve water-soluble deposits and corrosion products. Scanning electron microscopy (SEM) was performed using an FEI Quanta 650 field emission gun SEM. Energy-dispersive spectroscopy (EDS) was performed using an Oxford Instruments X-Max 150 Energy Dispersive X-ray Spectroscopy (EDS) detector. For each pin, the entire circumference of all three cross-section locations were observed, and images were taken at locations with representative corrosion products. Oxford Aztec software was used for all EDS analysis and postprocessing.

4.3.4.2 X-ray diffraction

X-ray diffraction (XRD) was performed using a Malvern-Panalytical Empyrean X-ray diffractometer with a Cu Kα X-ray source and a GaliPIX3D detector. High temperature XRD of salt mixtures was performed in the Empyrean by loading salts onto a Pt foil and heating in an Anton Paar HTK1200N oven. Data acquisition occurred after a 5 min isothermal hold at the desired temperatures. Malvern Panalytical Highscore [56] software was used for data analysis.

4.3.4.3 Inductively-coupled plasma optical emission spectroscopy

A Thermo Scientific iCAP 6000 spectrometer was used for inductively-coupled plasma optical emission spectroscopy (ICP-OES) measurements of water soluble Na, Mg, Ca, K, S, Ni, Co, Cr, Al, and Y species on sample surfaces. Table 10 lists the optical emission wavelength used for each element.

Table 10. Optical emission wavelengths used for ICP-OES analysis

Element	Na	Mg	Ca	K	S	Ni	Co	Cr	Al	Y
Wavelength (Å)	8183	2795	3158	7664	1820	2316	2388	2835	3092	2422

Pin samples were digested in 4 mL of deionized (DI) water for 30 min with occasional gentle agitation. Only the top 4 cm of the pins were immersed, preventing contamination of the solution by leftover moldable ceramic at the base of the pins. Furnace button samples were digested in 1 mL DI water for 30 min and gentle agitation. All digestion solutions were diluted 10x with DI water and 1 mL HCl to dissolve any particles. Calibration curves for the ten previously mentioned elements were created using 100, 10, 1, and 0.1 ppmw standards. A blank DI water standard was used to set the zero/baseline concentrations. A 10 ppmw In internal standard and the In 3039 Å emission wavelength were used.

Al^{3+} proved difficult to measure, particularly because it was present in relatively small quantities on alloy surfaces. $Al_2(SO_4)_3$ is also the least stable of all the sulfates shown in Figure 16 and so there may not have been enough water-soluble Al compounds to allow for accurate measurement. The minimum detection threshold for this ICP-OES analysis was 0.1 ppm. Concentrations are omitted in all figures for which the measurement is suspect.

4.5 Results

4.5.1 Characterization of as-received model alloys

As-received model alloy specimens were cross-sectioned and imaged with SEM/EDS using a concentric ring backscattered electron detector. Figure 28, Figure 29, and Figure 30 show backscattered electron images of Alloy 1, Alloy 2, and Alloy 3, respectively. Phases were identified by EDS and grayscale thresholding using ImageJ [81,82] was used to determine the area phase area fraction, shown in Table 11. It is assumed that the alloys are sufficiently isotropic so that the phase area fraction is equivalent to the phase volume fraction. Alloys 1 and 2 consist primarily of β dendrites and interdendritic γ. Alloy 1 also consists of about 7.4 vol% σ distributed within β as precipitates approximately 1 μm in diameter. Submicron precipitates of γ occur within the β dendrites of Alloy 2. Alloy 3 consists primarily of β grains with α precipitates decorating grain boundaries. All three alloys had Ni-Al-Y intermetallic precipitates with composition between $(Ni, Al)_5Y$ and $(Ni, Al)_4Y$ as determined by EDS. These precipitates will be referred to as "yttrides" as their exact structure and composition could not be determined.

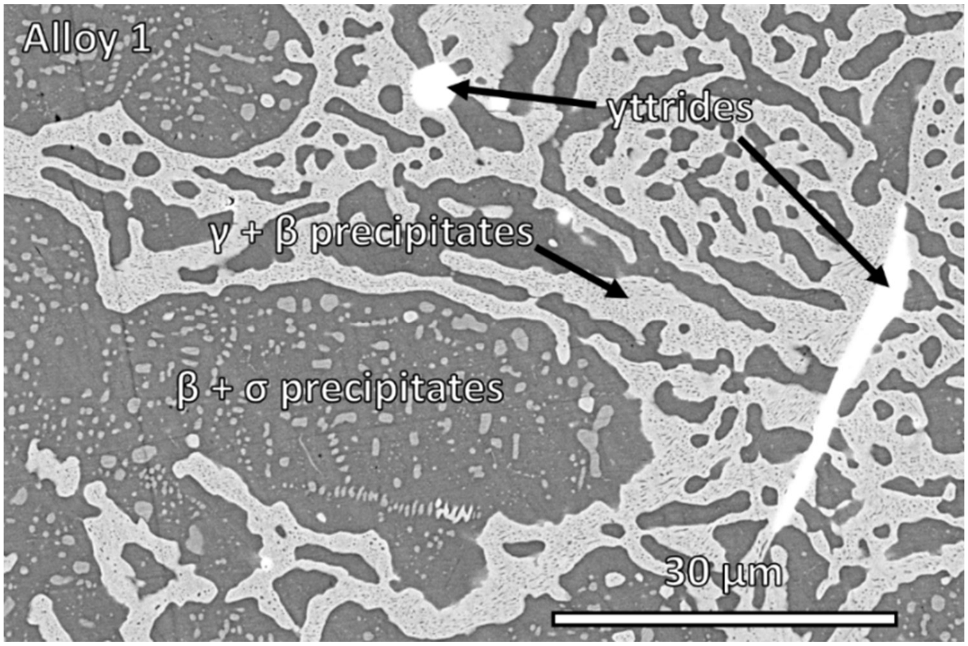

Figure 28. BSE micrograph of Alloy 1

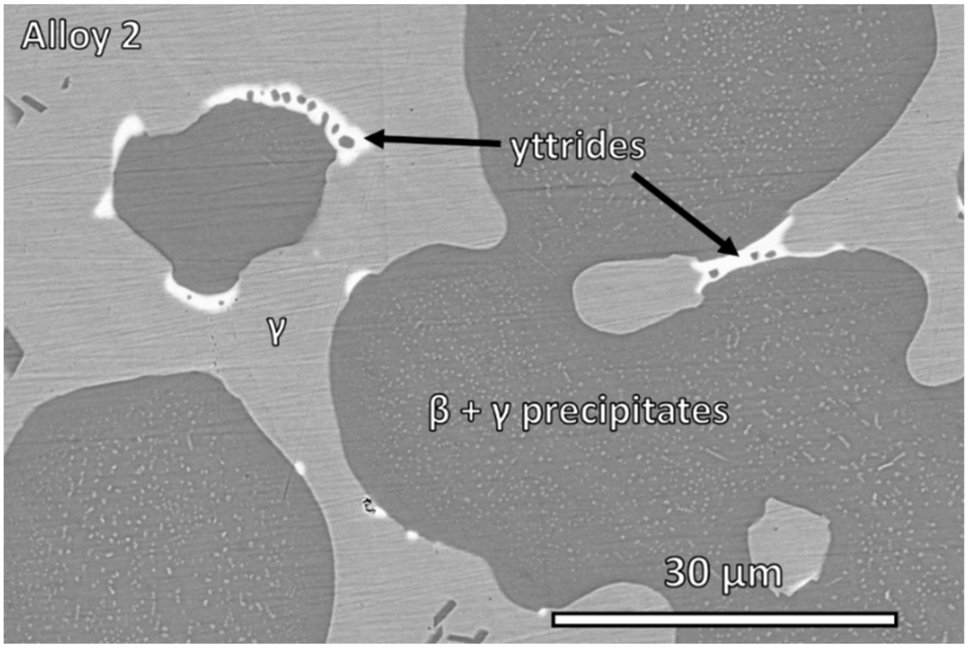

Figure 29. BSE micrograph of Alloy 2

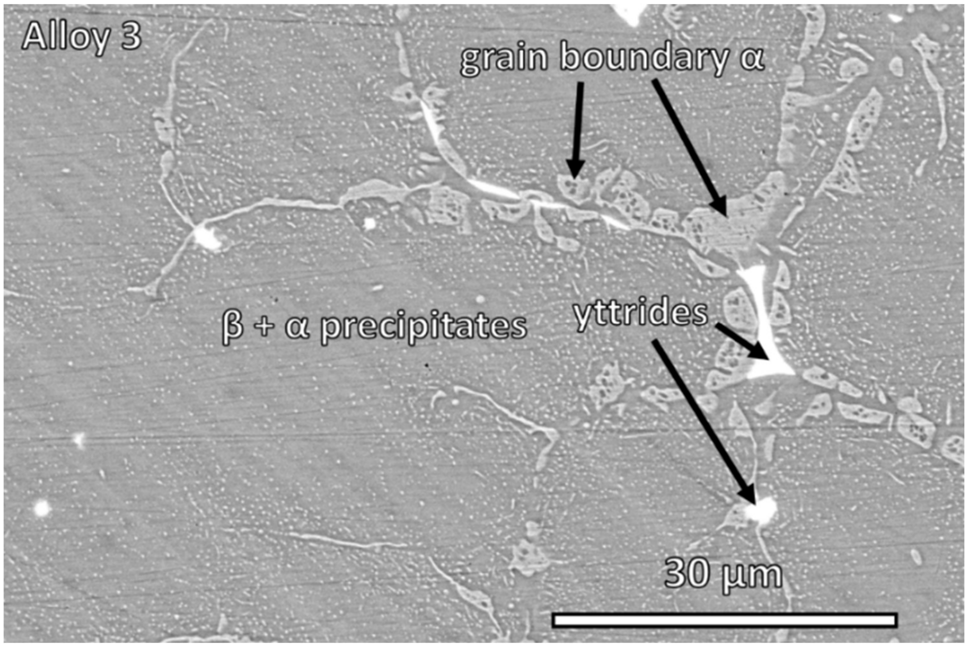

Figure 30. BSE micrograph of Alloy 3

Table 11. Phase fraction (area %) of Alloys 1-3 from ImageJ analysis

	γ	β	α	σ	Y ppt
Alloy 1	40.6	50.5	-	7.4	1.5
Alloy 2	21.1	78.4	-	-	0.5
Alloy 3	-	85.4	10.5	-	4.1

Comparison of Table 11 with Figure 20 shows that the model alloys do not have the predicted phase content. Note that Alloy 1 contains significantly more γ than Alloy 2. The yttride content of Alloy 3 is significantly higher than that of Alloy 1 and Alloy 2. The distribution of the yttrides is also significantly different for Alloy 3. Yttrides in Alloy 3 tend to occur in discrete "colonies" with diameters on the order of 200 μm, as shown in Figure 31. The separation between nearest Alloy 3 colonies range between hundreds of micrometers to 1-2 millimeters. In contrast, Alloys 1 and 2 contain significant amounts of of β-γ interfacial area, resulting in the more homogenous precipitation of smaller yttrides (≤ 30 μm along the longest axis) along these phase boundaries.

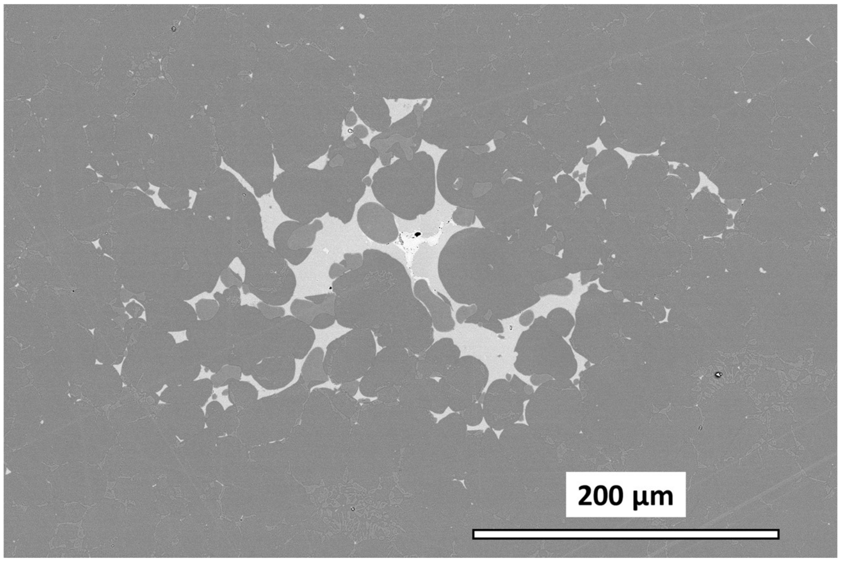

Figure 31. BSE micrograph showing Alloy 3 yttrides

ThermoCalc [83] 2021a and the TCNI9 nickel alloy database were used to understand the observed microsctructures. A single point equilibrium calculation (Gibbs energy minimization) at 1000 °C predicts an $(Ni,Al)_5Y$ phase fraction of 0.3 volume percent for all three model alloy compositions. This suggests that non-equilibrium processes during processing determine the yttride phase fractions. The presence of yttrides within the interdendritic γ phase of Alloys 1 and 2 suggests that β solidifies first, followed by γ, and lastly yttrides. This suggests that Y may be rejected from the solidifying phases, becoming enriched in the liquid. The phase fraction of yttrides would then be determined by the amount of Y enrichment in the last remaining liquid. A Scheil solidification simulation of all three alloy compositions was performed in ThermoCalc. The mass percent of Y remaining in the liquid as a function of temperature is shown in Figure 32. The Scheil simulation confirms that Y in the liquid is enriched by greater than one order of magnitude for all alloys at solidification of the final liquid. However, solidification of Alloy 3 results in nearly twice the Y enrichment predicted for Alloys 1 and 2.

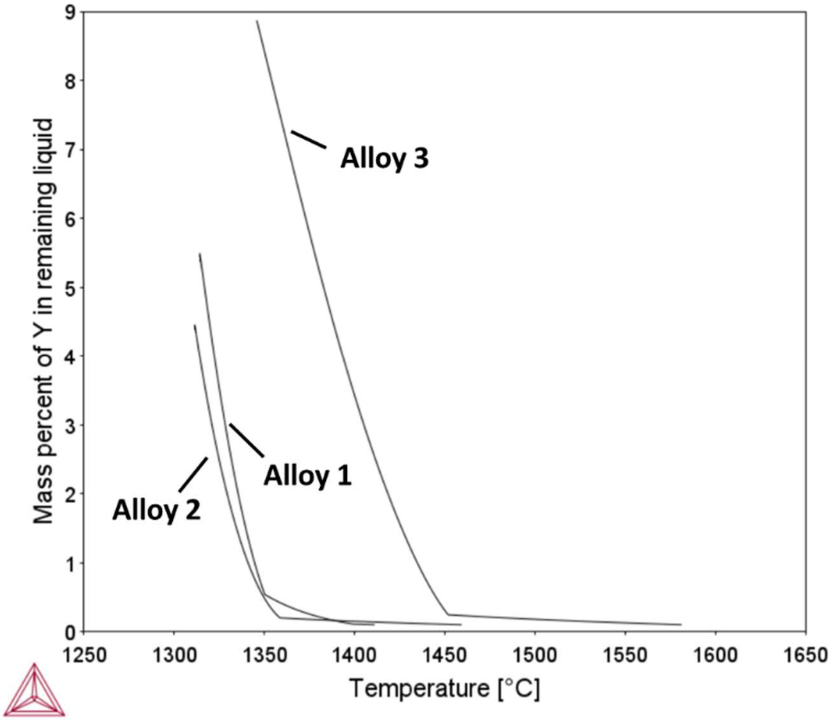

Figure 32. Results of a Scheil solidification simulation showing amount of Y in remaining liquid (wt%) for Alloys 1-3 as a function of temperature. "Solidification of the last remaining liquid" refers to the leftmost point on each curve, which occurs at different temperatures for different alloy compositions

A linear regression of the estimated phase fractions (from image analysis) with the final mass fraction of Y in the liquid is shown in Figure 33. An R^2 of 0.998 shows that the final Y content of the liquid is an accurate predictor of the amount of yttrides in the cast alloys. This is consistent with non-equilibrium solidification being the determining factor for Y enrichment during the casting process. MCrAlY coatings applied via high-velocity oxy-fuel spraying (HVOF) [84], air plasma spraying (APS) [85], and electron beam physical vapor deposition (EB-PVD) [86] exhibit smaller and more homogeneously distributed yttride precipitates than the cast alloys in the present study. This is probably because alloys formed by HVOF and APS solidify more quickly than cast alloys, reducing rejection of Y from the solidifying phases. EB-PVD eliminates non-equilibrium solidification issues entirely. MCrAlY coatings are applied via HVOF, APS, or EB-PVD for engineering applications, and so the cast model alloys have significantly more yttrides than the materials used in service.

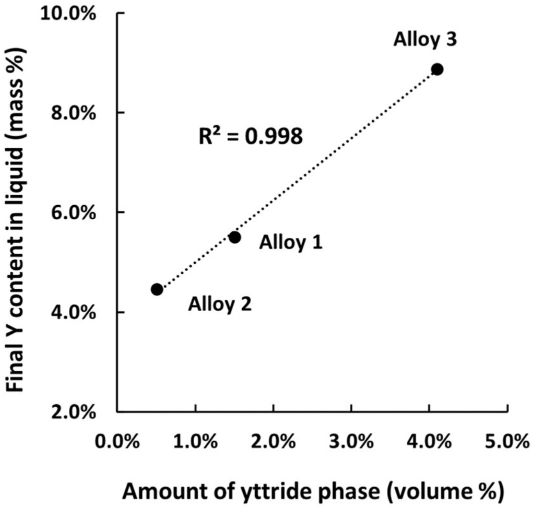

Figure 33. Correlation between the amount of yttride phase and the liquid Y content at solidification of the last remaining liquid predicted by the Thermocalc Scheil simulation

4.5.2 Artificial ocean water LVBR exposure

Cross-sectional SEM images for Alloys 1-3 after 500 h LVBR exposure to artificial ocean water are shown in Figure 34. Alloys 1 and 2 showed no detectable sign of corrosion. Alloy 3 exhibited significant localized corrosion (> 100 μm penetration depth in some locations) where yttrides were close to the surface. The bright phases below the dark corrosion product in Alloy 3 of Figure 34 are yttrides, and the corrosion product extends deeper along this network of precipitates than through the matrix.

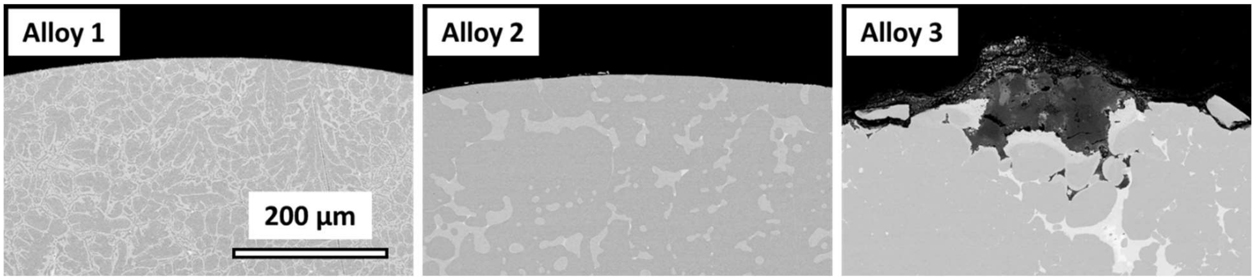

Figure 34. BSE SEM cross-sections of model alloy LVBR exposures to ASTM artificial ocean water in the LVBR for 500 h at 700 °C with cycling to room temperature for 1 h once per day

Plan views of Alloy 3 before and after water digestion are shown in Figure 35 and Figure 36, respectively. The darkest phase in Figure 35 is Na_2SO_4 and is present on the surfaces of all specimens. The brightest phase is only observed on Alloy 3 and is rich in Y, S, and O, suggesting it is likely $Y_2(SO_4)_3$ or $Y_2O_2SO_4$. Figure 36 (note the lower magnification) shows corrosion product nodules on Alloy 3. The nodule diameter and distribution suggest that these are the localized oxidation products of corroding yttride colonies. The nodules are surrounded by bright spots of bare metal where oxide has spalled off. Dark oxide flakes were observed on the white castable ceramic below Alloy 3 pins upon removal from the furnace for cycling to room temperature. Spallation was not observed on Alloys 1 and 2, suggesting that Alloy 3 exhibits enhanced scale spallation around the nodules.

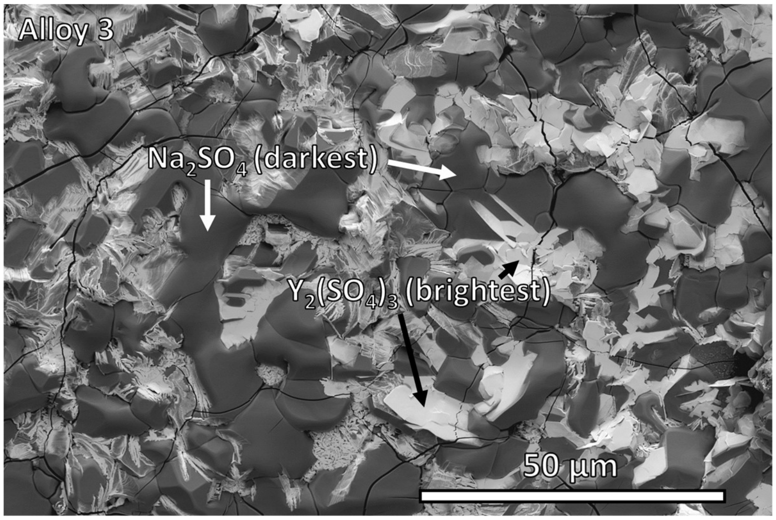

Figure 35. Mixed SE-BSE SEM plan view of Alloy 3 surface prior to water digestion showing Na_2SO_4 *deposits with* $Y_2(SO_4)_3$ *(Conditions: ASTM artificial ocean water in the LVBR for 500 h at 700 °C with cycling to room temperature for 1 h once per day)*

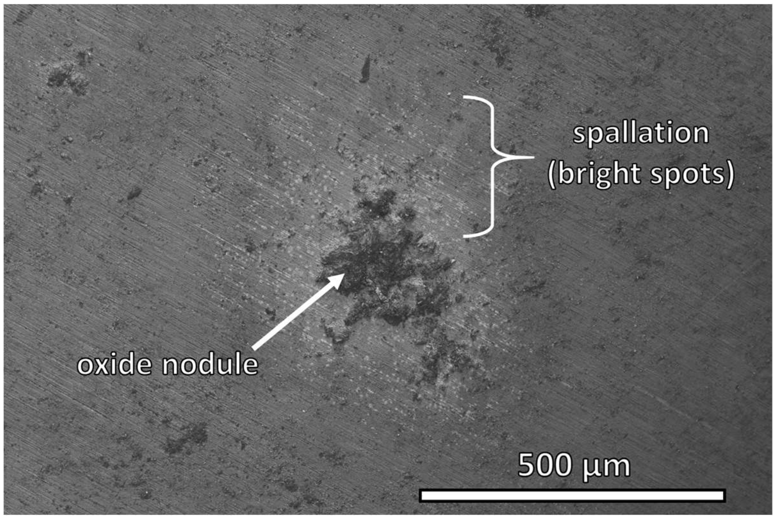

Figure 36. Mixed SE-BSE SEM plan view of Alloy 3 surface after water digestion showing scale spallation around corroding yttrides (Conditions: ASTM artificial ocean water in the LVBR for 500 h at 700 °C with cycling to room temperature for 1 h once per day)

The water-soluble deposit mass per area, shown in Figure 37, was calculated from the ICP-OES concentration measurements. Note that the y-axis on Figure 37 is logarithmic because concentrations varied by 3-4 orders of magnitude. Alloy 3, the only alloy to visibly corrode, shows elevated concentrations of Ni^{2+}, $Co^{2+/3+}$ and Y^{3+}. Y^{3+} was the most concentrated water-soluble alloying element species for all model alloys despite making up only 0.1 wt% of the alloys by mass. The detected Y^{3+} concentrations increased with increasing yttride phase fractions, as demonstrated in Figure 38. $Cr^{3+/6+}$ and Al^{3+} (when Al^{3+} could be measured accurately) were the least concentrated alloying species detected. All these water-soluble deposits may be assumed to be sulfates because of their water solubility and their known stability in SO_3-containing LTHC conditions.

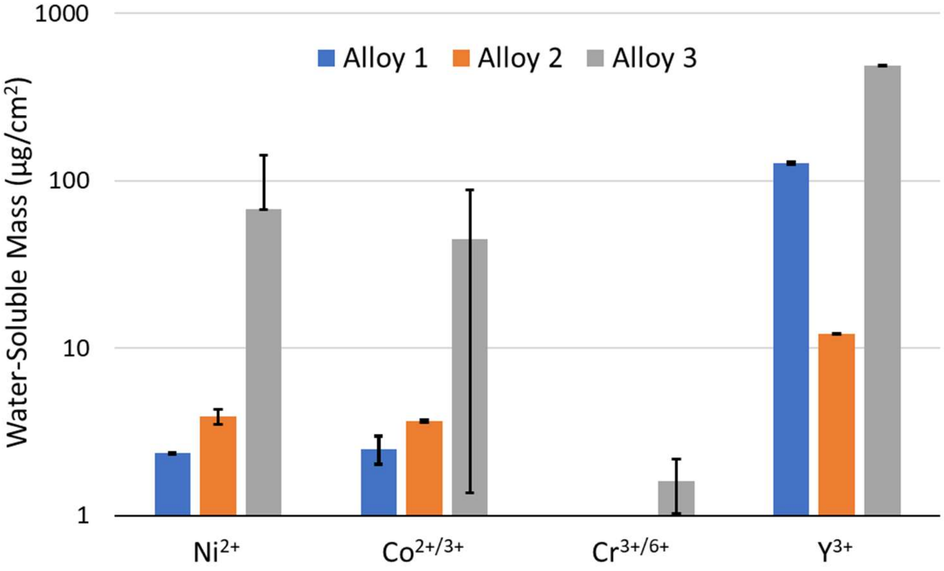

Figure 37. ICP-OES results for model alloys exposed to ASTM artificial ocean water in the LVBR for 500 h at 700 °C with cycling to room temperature for 1 h once per day

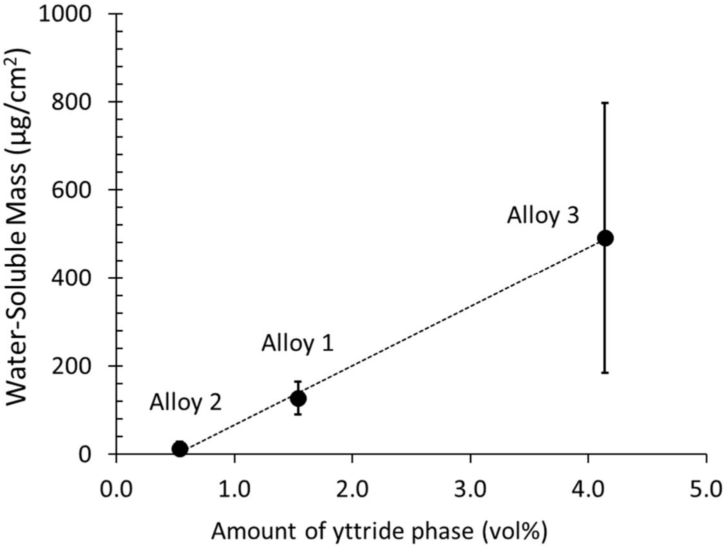

Figure 38. Plot showing the relationship between yttride phase fraction and concentration of water-soluble Y^{3+} *on sample surfaces*

4.5.3 Na^+, Mg^{2+}, and mixed Na^+-Mg^{2+} LVBR exposures

Representative backscattered electron images of Alloys 1-3 exposed to the NaCl, $MgCl_2$, and mixed NaCl-$MgCl_2$ salt solutions injected into the LVBR are shown in Figure 39. Note that EDS of the deposits prior to water digestion show that they are mostly Na_2SO_4 and/or $MgSO_4$ because the chlorides reacted with SO_x to form sulfates. The different experimental conditions are referred to as "Na^+," "Mg^{2+}," and "Na^+-Mg^{2+} to avoid confusion due to the difference in the chemistry of the injected salt solutions, the resulting deposits, and the fact that Mg compounds may be either MgO or $MgSO_4$. The samples exposed to Na^+ exhibit the same corrosion results as the artificial ocean water exposures, with localized corrosion of yttrides in Alloy 3 and no detectable corrosion on Alloys 1 and 2. The Mg^{2+} exposures resulted in no detectable corrosion on any samples, even at Alloy 3 locations containing yttrides near sample surfaces. Corrosion was detected for all alloys exposed to mixed Na^+-Mg^{2+}. The corrosion penetration depth on Alloy 1 is ≤ 10 μm and is therefore barely visible in Figure 39 (see Figure 44 for a higher magnification image of the same location). The Na^+-Mg^{2+}-induced corrosion morphology of Alloy 2 is that of nodules ≤ 500 μm in diameter. The corrosion of Alloy 3 exposed to Na^+-Mg^{2+} is more uniform than that observed on the Na^+-only and artificial ocean water samples and is not localized to yttrides.

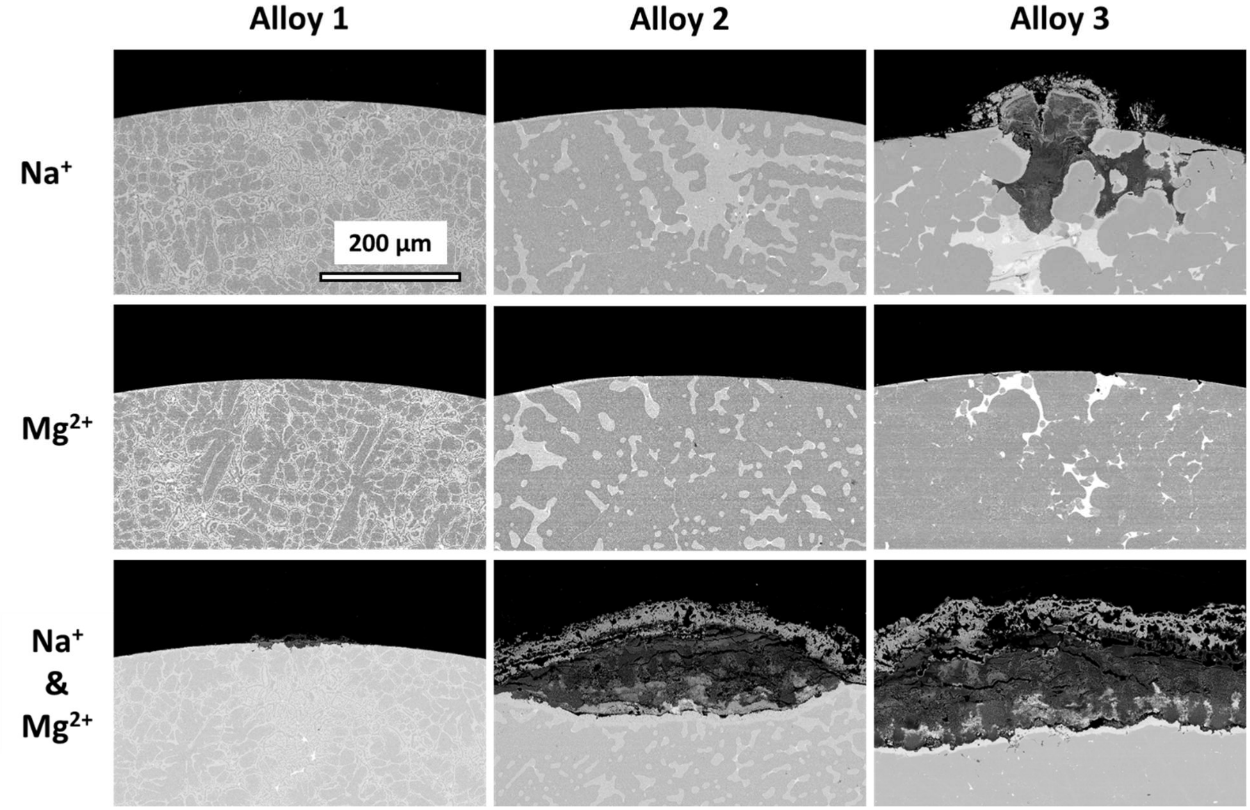

Figure 39. BSE SEM cross-sections of model alloy exposures to Na^+ and/or Mg^{2+} in the LVBR for 500 h at 700 °C with cycling to room temperature for 1 h once per day

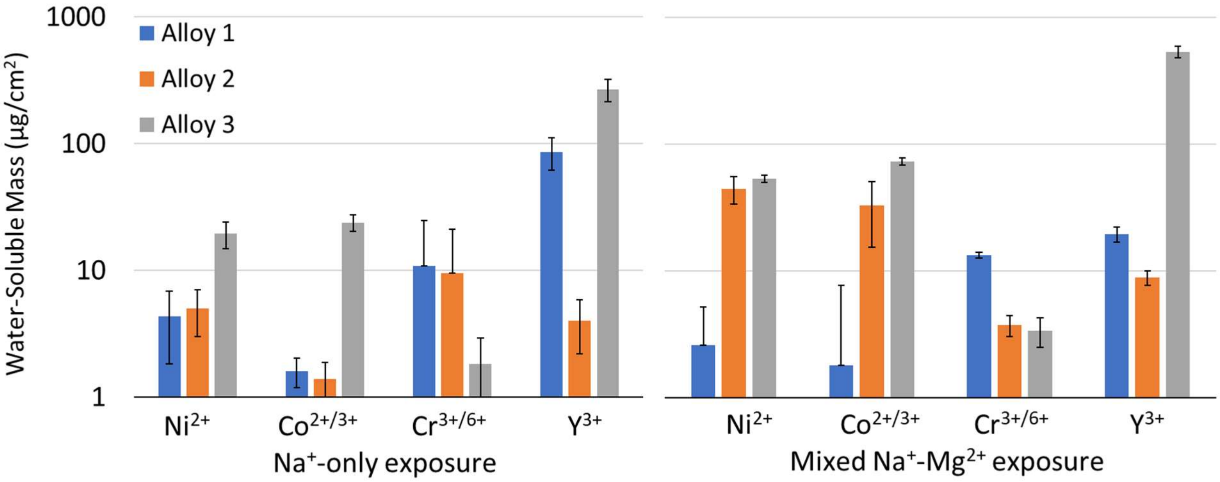

Figure 40. ICP-OES results for water-soluble alloying elements exposed in the LVBR at 700 °C for 500 h to injected contaminant solutions containing Na^+*-(left) and mixed* Na^+*-*Mg^{2+}*-(right)*

4.5.4 Characterization of Alloy 3 LVBR corrosion by exposure to Na^+

EDS of the corrosion product for Alloy 3 exposed to Na^+ is shown in Figure 41. The dark corrosion product consists of mostly oxides, sulfides, and/or sulfates of Al and, to a lesser extent, Ni. Sulfides/sulfates are located at the oxide-metal interface. The corrosion product is topped by a layer of NiO/CoO and then an outermost layer rich in Y, S, and O. The Y-S-O layer suggests that there is either residual $Y_2(SO_4)_3$/$Y_2O_2SO_4$ even after water digestion or mixed oxides and sulfides of Y. The O map, S map, and SEM image show that corrosion penetrated along a network of connected or nearly-connected yttrides.

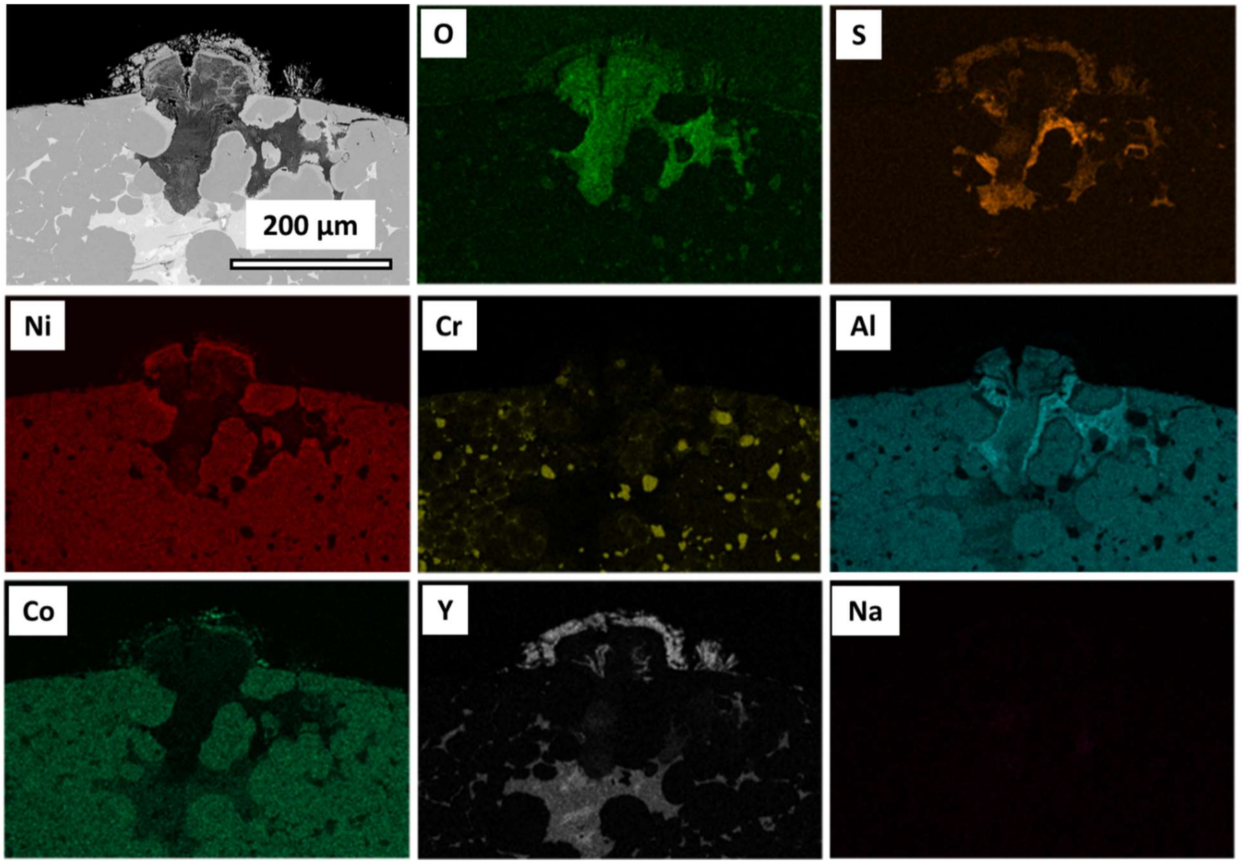

Figure 41. EDS images of Alloy 3 corrosion by Na$^+$ in the LVBR for 500 h at 700 °C with cycling to room temperature for 1 h once per day

Figure 42 shows an enlarged image of the corrosion morphology in Figure 41. There is an Al-depleted region in the alloy near the metal-corrosion product interface where β converted to γ' and even γ. An yttride decomposition region is visible where O and S reach the partially-decomposed precipitates at the image bottom. Figure 43 is a higher resolution image of this decomposition region and shows that it actually consists of two distinct regions. Further away from the Al-rich corrosion product it consists of irregular sulfides of Ni and Y in a β metallic solid solution. Closer to the Al-rich corrosion product it consists of Ni/Y sulfides and γ'. The Y, Ni, and S ratios of the sulfides are not consistent, possibly indicating nonstoichiometry.

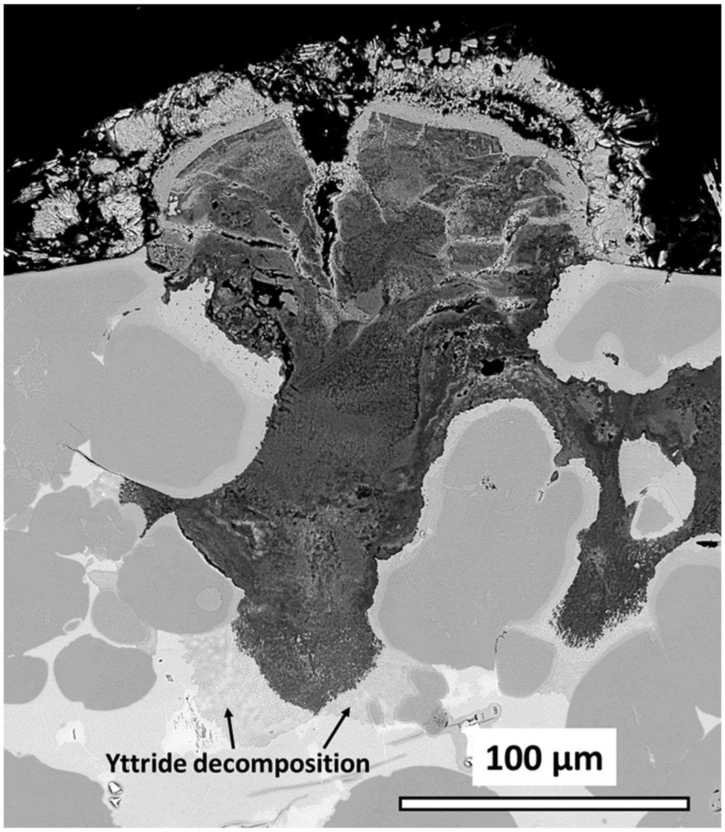

Figure 42. Detail of Alloy 3 corrosion morphology with NaCl contaminant in the LVBR for 500 h at 700 °C, cycling to room temperature for 1 h once per day

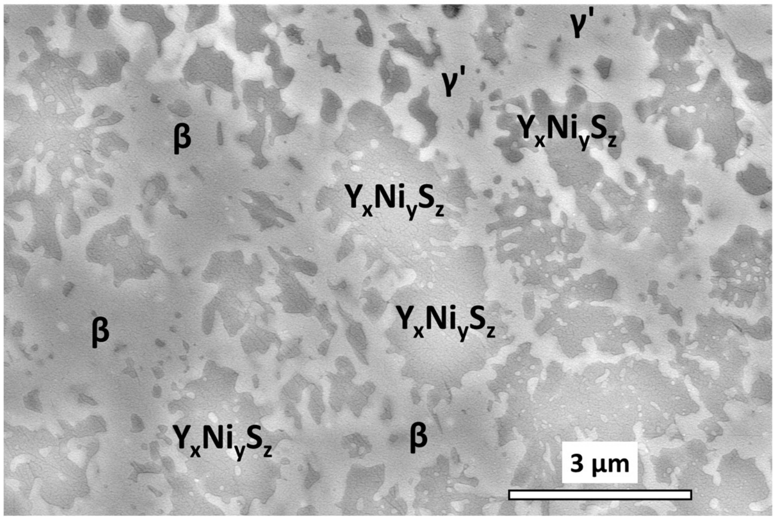

Figure 43. Higher magnification BSE image of the decomposing yttrides (Alloy 3) indicated in Figure 42

4.5.5 Characterization of LVBR corrosion of Alloys 1, 2, and 3 exposed to Na^+-Mg^{2+}

Alloy 1 exposed to Na^+-Mg^{2+} corroded significantly less than that of Alloys 2 and 3 in the same environment (note the higher magnification for Alloy 1). The corrosion morphology of Alloy 1 resembled pitting as the metal-corrosion product interface is hemispherical. Corrosion of Alloy 1 only occurred at regions relatively rich in β and poor in γ. The composition of the corrosion product also varies with the relative amounts of γ and β in the vicinity. The inner layer of the corrosion product consists of Cr_2O_3-Al_2O_3 but is poor in Al_2O_3 directly above the γ phase. Sulfides or sulfates or Al and Cr decorate the metal-oxide interface. The outer layer consists of MgO.

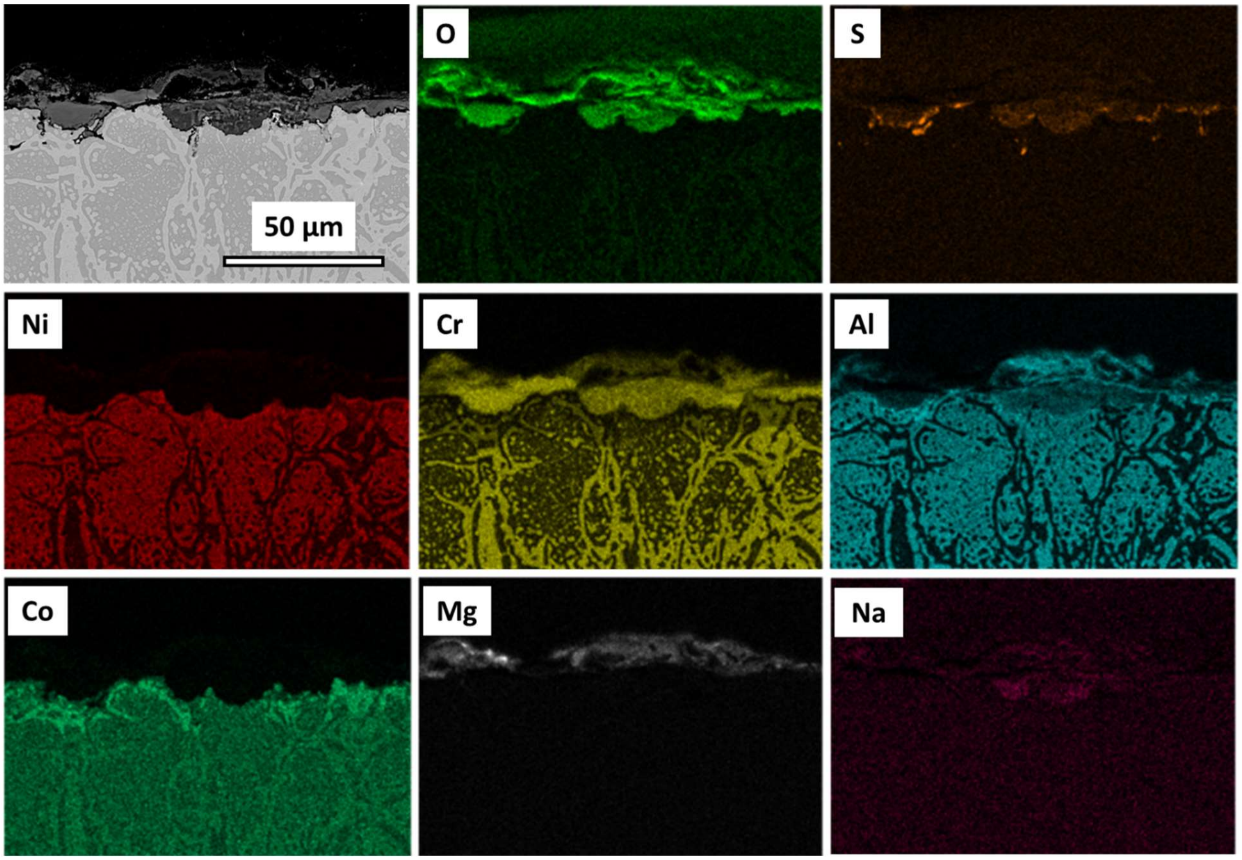

Figure 44. EDS of Alloy 1 corrosion with Na^+-Mg^{2+} mixed contaminant in the LVBR for 500 h at 700 °C, cycling to room temperature for 1 h once per day (note the higher magnification to show detail)

Alloy 2 did not corrode in either the pure Na^+ or pure Mg^{2+} exposures. However, Alloy 2 corroded in mixed Na^+-Mg^{2+} with a nodular corrosion morphology, as shown in Figure 45. The corrosion product is mostly Al_2O_3-Cr_2O_3, with a thin layer of sulfides of Al and Cr at the metal interface. Cr and Al are depleted near the metal-corrosion product interface. The outermost layer consists of mixed NiO-CoO-MgO.

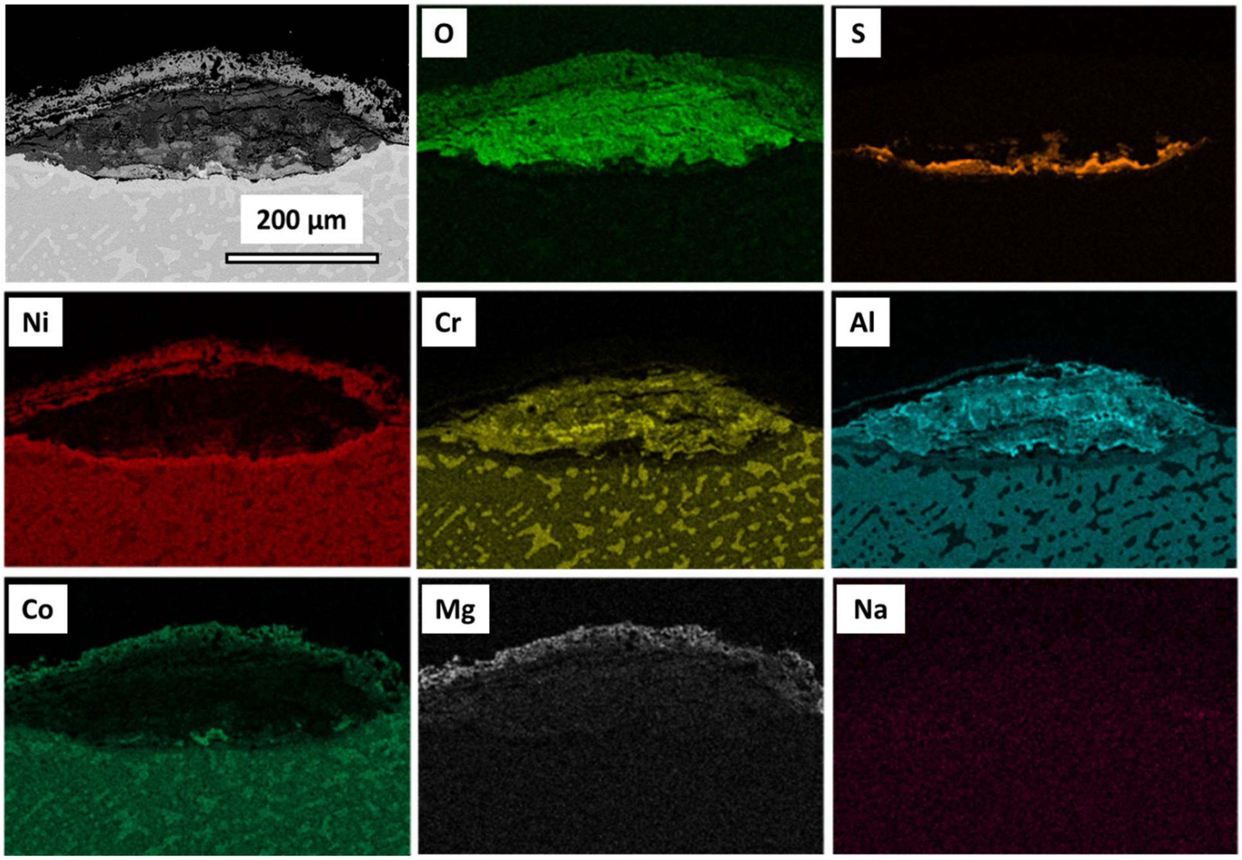

Figure 45. EDS of Alloy 2 corrosion with NaCl/$MgCl_2$ mixed contaminant in the LVBR for 500 h at 700 °C, cycling to room temperature for 1 h once per day

Figure 46 shows an Alloy 3 corrosion morphology that is noticeably more uniform than that of Alloy 3 exposed only to Na^+ or artificial ocean water. Corrosion is also not localized to locations with yttrides near the interface, as is the case with exposure to Na^+ and artificial ocean water. Like

Alloys 1 and 2, the bulk of the corrosion product is Al_2O_3-Cr_2O_3. There are significantly more sulfides and/or sulphates at the metal-corrosion product interface than there are in Alloys 1 and 2. These S-rich phases contain Ni and Co in addition to Al. The outer corrosion layer consists of mixed NiO-CoO-MgO, although with possibly less MgO than on Alloy 2.

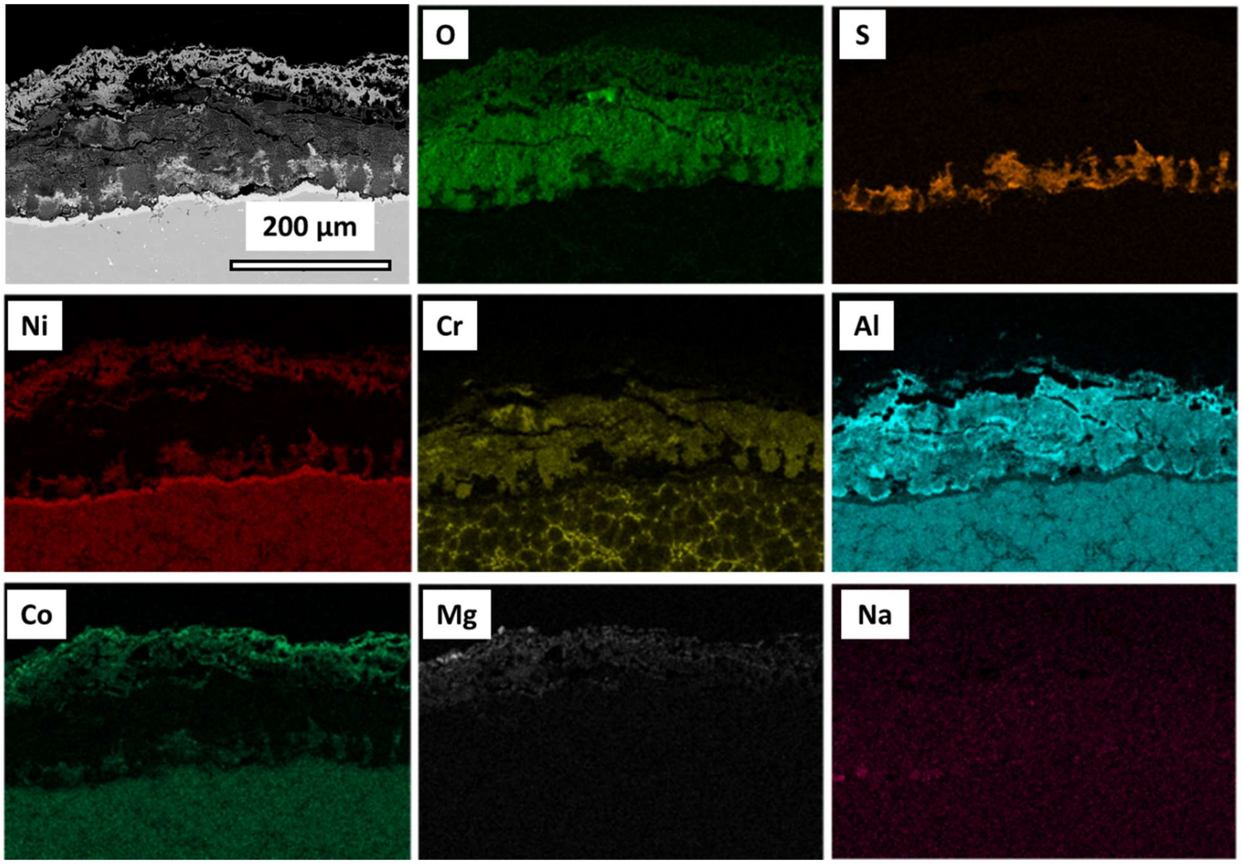

Figure 46. EDS of Alloy 3 corrosion with NaCl/$MgCl_2$ mixed contaminant in the LVBR for 500 h at 700 °C, cycling to room temperature for 1 h once per day

4.5.6 Furnace exposures of model alloys to Na_2SO_4

Figure 47 shows cross-sectional SEM images of Alloys 1, 2, and 3 after 48 h tube furnace exposure with 2 mg/cm^2 of Na_2SO_4. Alloy 1 exhibits pitting and selective corrosion of γ. Alloy 2 has a relatively uniform corrosion front with penetration depths of approximately 60-100 µm. Al depletion below the corrosion front resulted in a 30 μm thick layer of γ. This γ layer contains sulfides, particularly at the metal-oxide interface. The corrosion front of Alloy 3 is less uniform than that of Alloy 2 but more irregular than the hemispherical pitting of Alloy 1. Figure 48 shows the post-exposure weight changes of the model alloys. The weight change of Alloy 2 is significantly greater than the Alloy 1 and 3 weight changes. The weight change measurements appear to be consistent with the amount of metal consumption observed in the cross-sections.

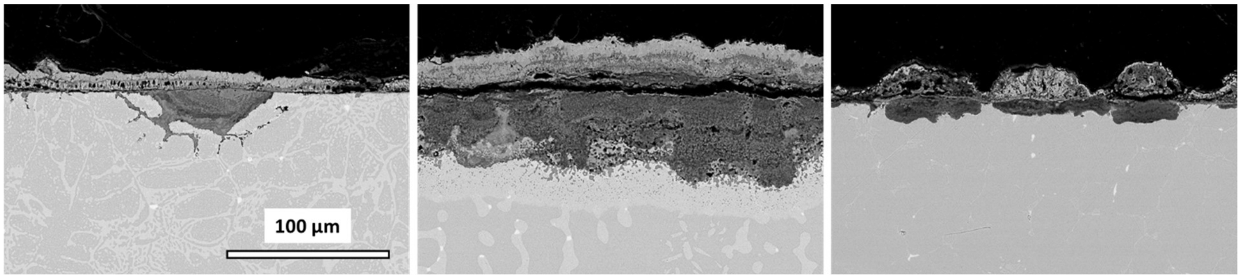

Figure 47. BSE cross-sections of Alloy 1 (left), Alloy 2 (center), and Alloy 3 (right) after tube furnace exposure at 700 °C with 1.4 x 10^{-5} mol/cm^2 Na_2SO_4 and 1000 ppm SO_2 in O_2 with Pt catalyst for 48 h

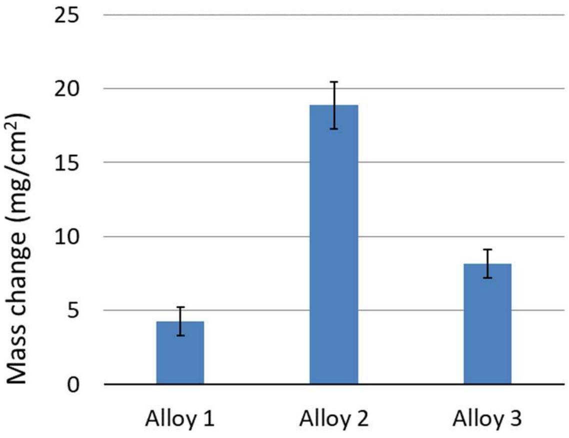

Figure 48. Post-water-digestion weight changes of Alloys 1-3 after tube furnace exposure at 700 °C with 2 mg/cm^2 Na_2SO_4 and 1000 ppm SO_2 in O_2 with Pt catalyst for 48 h

EDS maps of the Alloy 1 cross-section are displayed in Figure 49. The corrosion product in the pits are mostly composed of Cr_2O_3, with Cr and Al sulfides/sulfates near the pit-metal interface. Sulfides, oxides, and/or sulfates of Cr and Al selectively penetrate along γ channels. The outermost corrosion layer is more uniform than the pitting and consists of oxides of Ni and, to a lesser extent, Cr and Al.

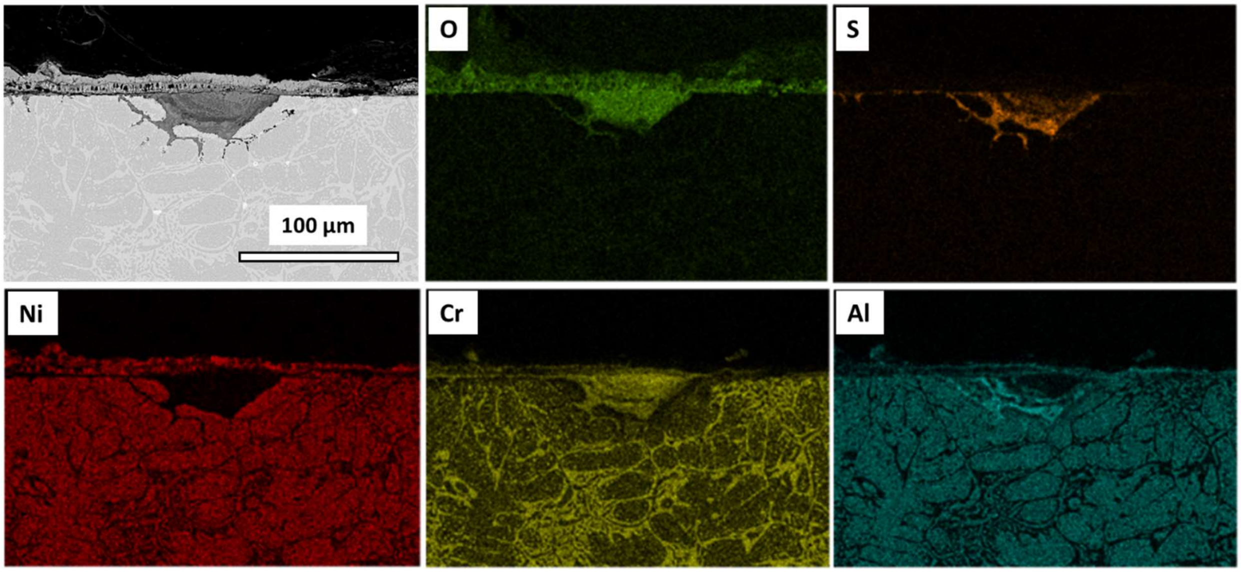

Figure 49. EDS of Alloy 1 corrosion after tube furnace exposure at 700 °C with 1.4×10^{-5} mol/cm^2 Na_2SO_4 and 1000 ppm SO_2 in O_2 with Pt catalyst for 48 h

The EDS maps of Figure 50 show that the Alloy 2 corrosion product is mostly Cr_2O_3 and Al_2O_3. The γ depletion layer is poor in both Cr and Al. The distribution of Cr and Al in the scale is inhomogeneous, possibly reflecting the relatively coarse distribution of β and γ in the alloy. The sulfides are primary Cr_xS and are detected in the metallic γ layer and within the Al/Cr oxides close to the oxide-metal interface. The outer part of the scale, which is partially detached, consists of an inner layer oxide rich in Al and an outer layer of NiO/CoO.

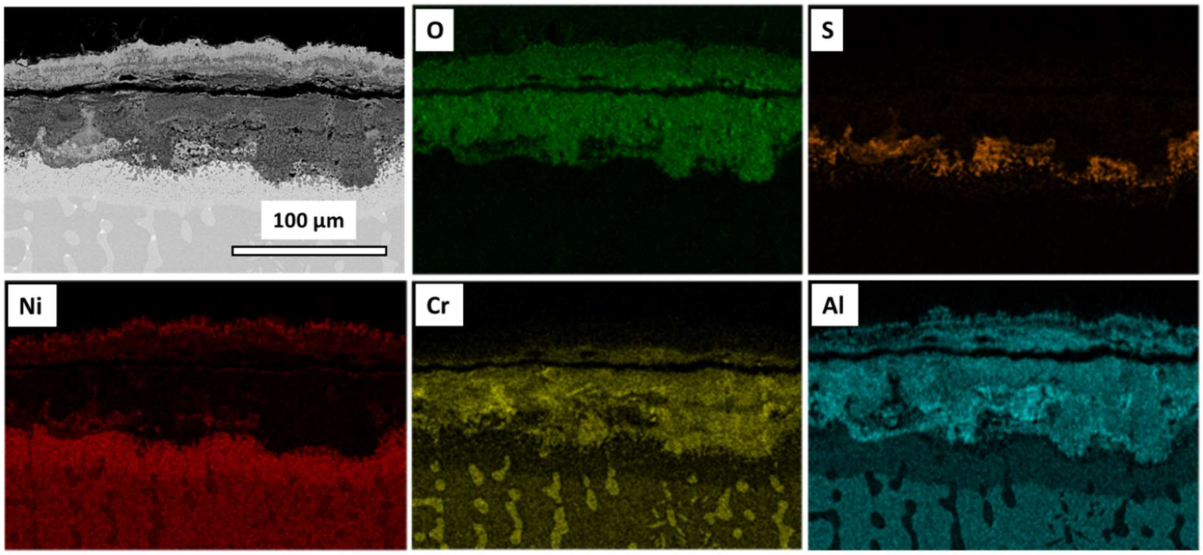

Figure 50. EDS of Alloy 2 corrosion after tube furnace exposure at 700 °C with 1.4 x 10^{-5} mol/cm^2 Na_2SO_4 and 1000 ppm SO_2 in O_2 with Pt catalyst for 48 h

Figure 51 shows more Al than Cr in the Alloy 3 reaction products. Al_2O_3 is a likely the main reaction product, with sulfides and/or sulfates of Al enriched at the metal-oxide interface. The outer scale consists of NiO/CoO. There is no Al or Cr detectable depletion layer.

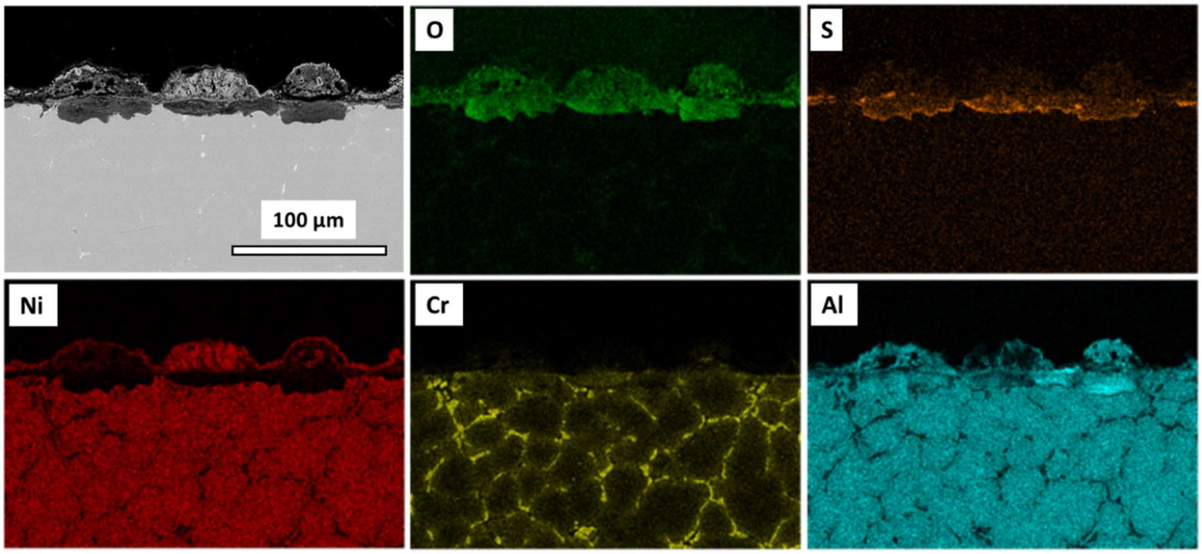

Figure 51. EDS of Alloy 3 corrosion after tube furnace exposure at 700 °C with 1.4 x 10^{-5} mol/cm^2 Na_2SO_4 and 1000 ppm SO_2 in O_2 with Pt catalyst for 48 h

Yttrides in Alloy 3 selectively corroded in the tube furnace environment, consistent with the LVBR results. Figure 52 is another cross-sectional image of Alloy 3, showing increased amounts of corrosion products above reacting yttrides. The scale above the corroding yttrides is buckled and cracked.

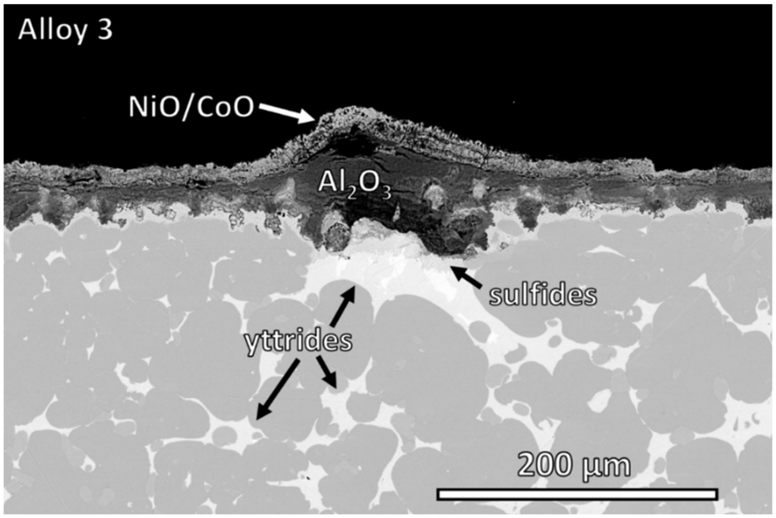

Figure 52. Corroding yttride disrupting the scale on Alloy 3 after tube furnace exposure at 700 °C with 1.4 x 10^{-5} *mol/cm*^{2} Na_2SO_4 *and 1000 ppm* SO_2 *in* O_2 *with Pt catalyst for 48 h*

The ICP-OES results for the Na_2SO_4 furnace exposures are shown in Figure 53. Ni^{2+} and $Co^{2+/3+}$ salts are the primary water-soluble reaction products for all three model alloys. The measured concentration of Ni^{2+} and $Co^{2+/3+}$ corresponds roughly to the amount of corrosion as measured by weight gain, with Alloy 2 having significantly higher amounts of water-soluble Ni^{2+} than that of Alloys 1 and 3. The Y^{3+} concentrations are comparable to the relatively low $Cr^{3+/6+}$ concentration. This is a significant difference from the LVBR results shown in Figure 37, as Y^{3+} is the most concentrated water-soluble cation for all three alloys exposed in the LVBR. The ICP-OES results shown in Figure 53 are qualitatively similar to the LVBR results with the exception of Y^{3+}.

The absolute concentration of cations as measured by ICP-OES is a function of both the alloying elements' tendencies to form water-soluble reaction products and their concentration in the alloy. The effect of alloy composition is removed or reduced via normalization of the measured ICP-OES concentrations by the concentration of the corresponding element in the alloy. This composition-normalized quantity is intended to more closely reflect the tendency of each alloying element to react and form a salt. Figure 54 shows these normalized quantities for all three alloys exposed to Na_2SO_4. Y^{3+} noticeably has the highest tendency to form a salt, followed by $Co^{2+/3+}$, Ni^{2+}, and lastly $Cr^{3+/6+}$. The normalized values do not vary as much from alloy to alloy compared to the absolute concentrations, and so the averages of all alloys are shown with white bars.

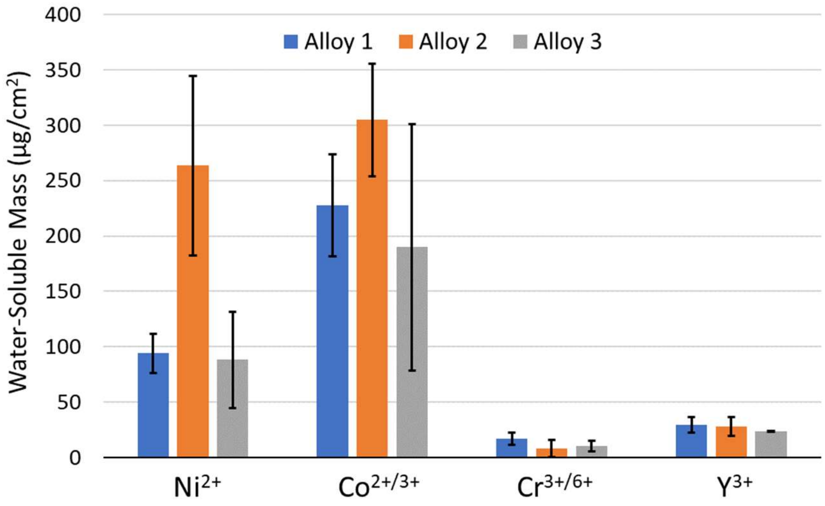

Figure 53. ICP-OES results for Alloys 1-3 for water-soluble compounds after tube furnace exposure at 700 °C with 2 mg/cm^2 Na_2SO_4 and 1000 ppm SO_2 in O_2 with Pt catalyst for 48 h

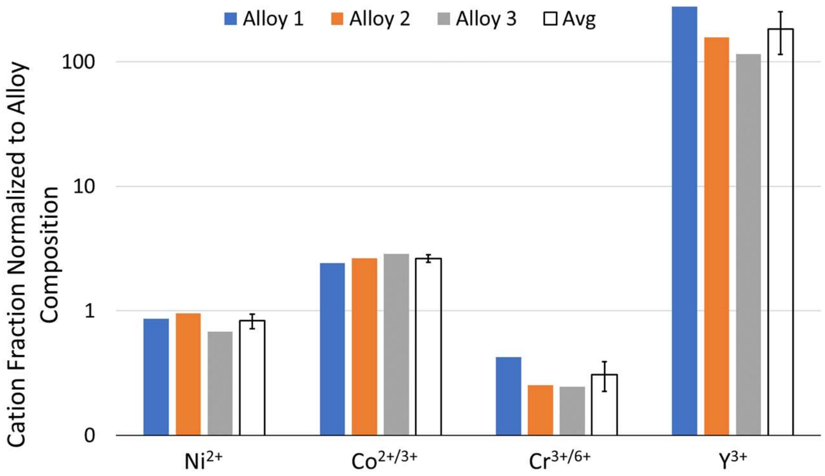

Figure 54. ICP-OES results normalized by concentration of corresponding alloying element for Alloys 1-3 for water-soluble compounds after tube furnace exposure at 700 °C with 2 mg/cm^2 Na_2SO_4 and 1000 ppm SO_2 in O_2 with Pt catalyst for 48 h

The water-soluble salts may be assumed to be sulfates because of the relatively high pSO_3 of the flowing catalyzed gas. The stabilities of the sulfates may be quantified with the Gibbs energies of reaction for the formation of sulfates from the corresponding oxides, normalized by the moles SO_3 consumed. This is analogous to the method used by Ellingham [1] for comparing the relative stabilities of oxides. Free energies of reaction were calculated using thermochemical data from the FactSage [38] Pure Substances database. Figure 55 is a plot of the normalized Gibbs energy of reaction for the alloying elements versus the average salt:alloy ratios from Figure 54. There is a good exponential correlation between the thermodynamic data and the normalized ICP-OES measurements (note the logarithmic scale for the salt:alloy ratio).

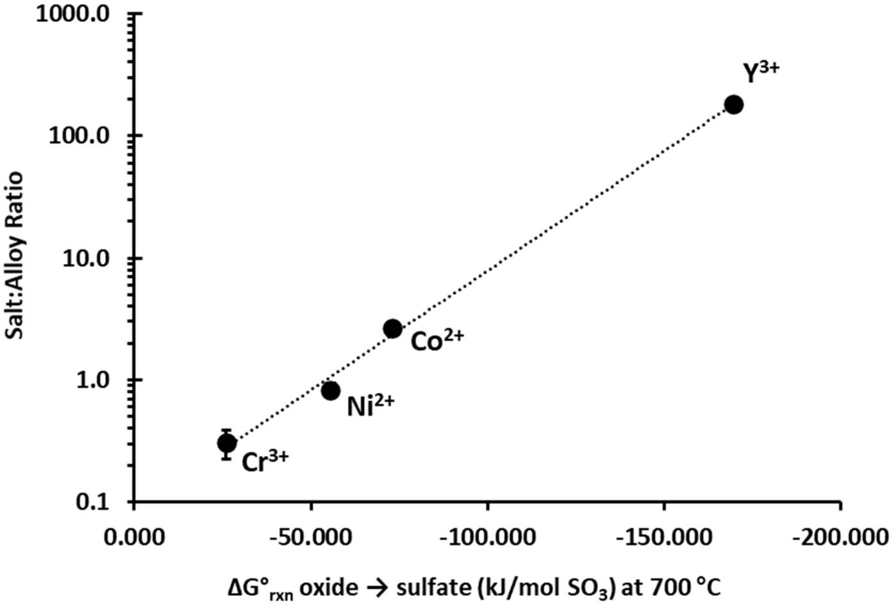

Figure 55. Correlation between the experimentally observed average normalized concentration from Figure 54 and the Gibbs energy of sulfation per mole of SO_3. Note the log scale for the y-axis

4.5.7 $MgSO_4$ and mixed Na_2SO_4- $MgSO_4$ tube furnace exposures

There is no detectable corrosion of the model alloys exposed in the tube furnace with a pure $MgSO_4$ deposit. This behavior was expected because pure $MgSO_4$ is solid at the 700 °C test temperature.

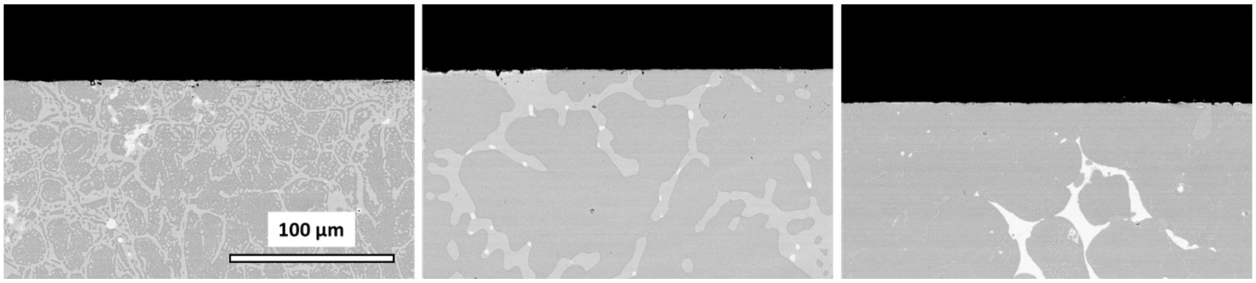

Figure 56. BSE cross-sections of Alloy 1 (left), Alloy 2 (center), and Alloy 3 (right) after tube furnace exposure at 700 °C with 2.8 x 10^{-5} mol/cm^2 $MgSO_4$ and 1000 ppm SO_2 in O_2 with Pt catalyst for 48 h

Cross-sectional SEM images of model alloys after tube furnace exposure to mixed Na_2SO_4-$MgSO_4$ deposits are shown in Figure 57. Notably, here corrosion is less than that observed in the LVBR. Higher magnification images of the same samples in Figure 58 show that there are thin reaction products and/or water-insoluble deposits. Alloy 1 has a scale approximately 2 µm thick except for where it penetrates several µm further along the γ phase. Alloys 2 and 3 both possess an inner scale layer less than 1 µm thick. A second, thicker layer (5-10 µm) is above the thin scale. The backscattered electron contrast suggests that this layer may Na- and Mg-rich and insoluble in water, as it remained intact after water digestion.

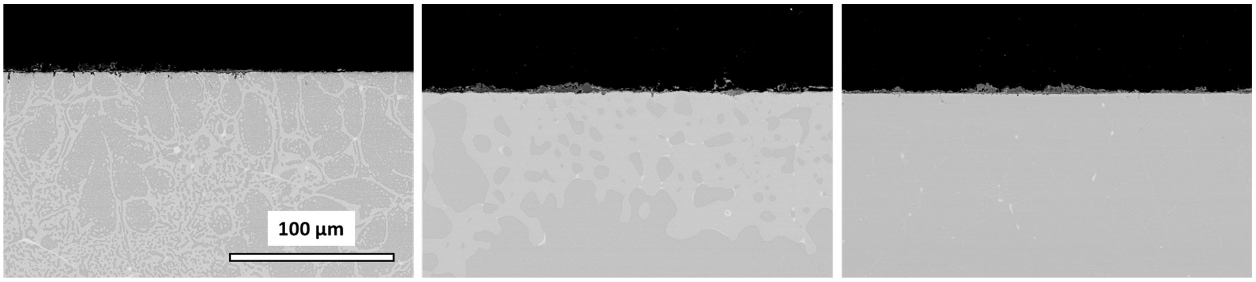

Figure 57. BSE cross-sections of Alloy 1 (left), Alloy 2 (center), and Alloy 3 (right) after tube furnace exposure at 700 °C with 4.6 x 10^{-6} mol/cm^2 Na_2SO_4 + 9.3 x 10^{-6} mol/cm^2 $MgSO_4$ and 1000 ppm SO_2 in O_2 with Pt catalyst for 48 h

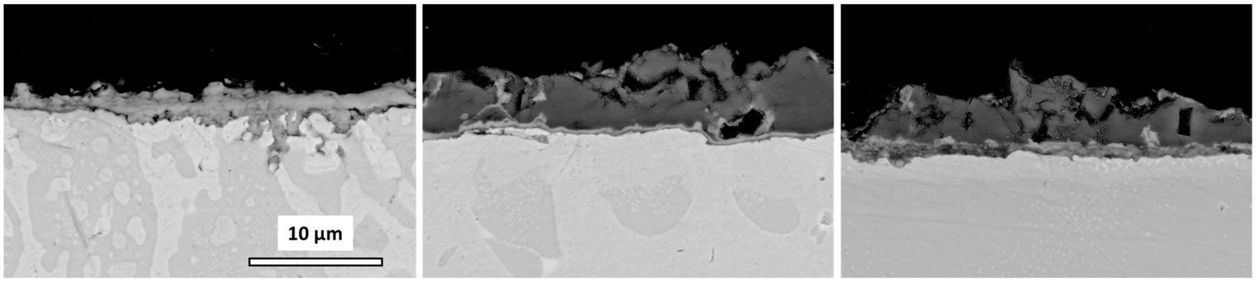

Figure 58. Higher magnification of Figure 57 (BSE cross-sections of Alloy 1 (left), Alloy 2 (center), and Alloy 3 (right) after tube furnace exposure at 700 °C with 4.6 x 10^{-6} mol/cm^2 Na_2SO_4 + 9.3 x 10^{-6} mol/cm^2 $MgSO_4$ and 1000 ppm SO_2 in O_2 with Pt catalyst for 48 h)

EDS of Alloy 1 in Figure 59 shows that the scale is primarily Cr_2O_3. Cr is content is reduced in the γ phase below the scale. There is no detectable Al or Ni signal within the oxide and no observed depletion of either Al or Ni from the alloy. Either $Cr_2(SO_4)_3$ or a mixture of oxides and sulfides of Cr is present where there is selective reaction with the γ phase.

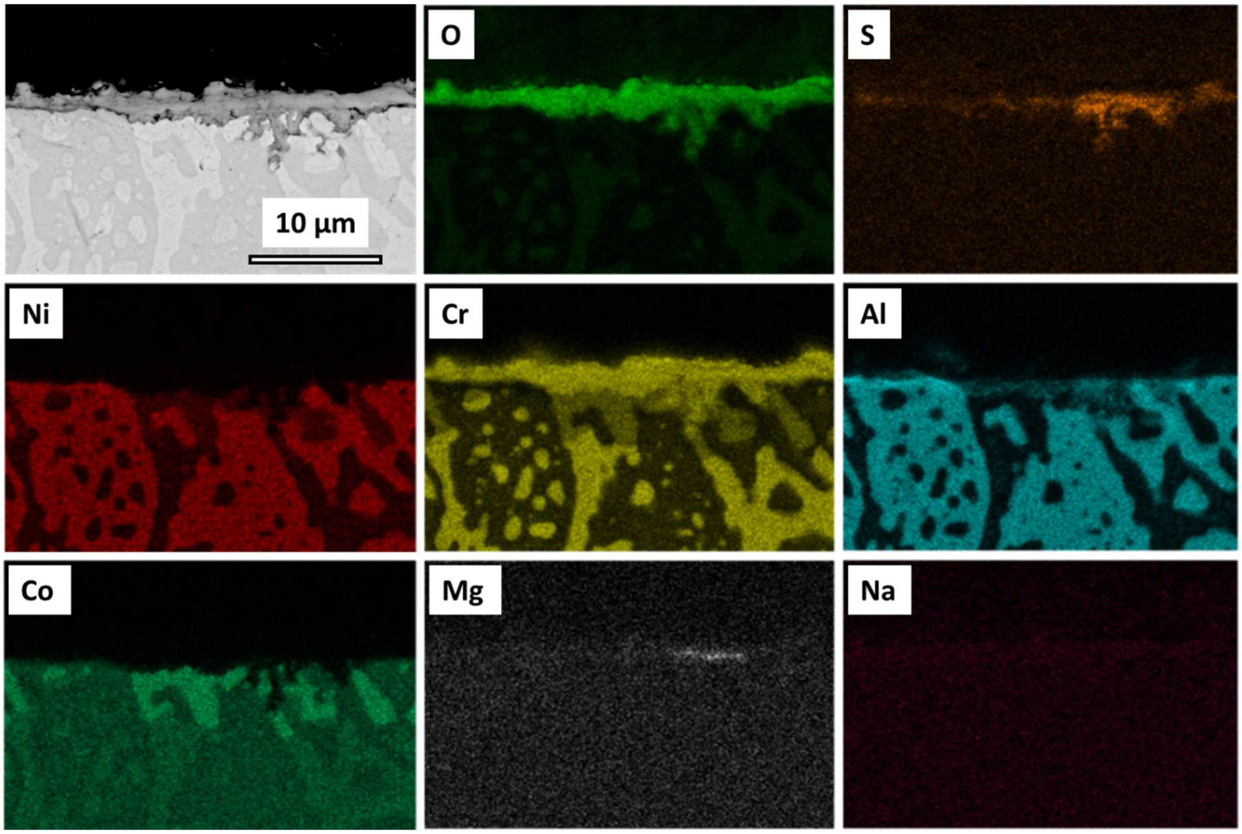

Figure 59. EDS of Alloy 1 after tube furnace exposure at 700 °C with 4.6 x 10^{-6} *mol/cm*^{2} Na_2SO_4 *+ 9.3 x* 10^{-6} *mol/cm*^{2} $MgSO_4$ *and 1000 ppm* SO_2 *in* O_2 *with Pt catalyst for 48 h*

Figure 60 shows that the scale of Alloy 2 is mixed Cr_2O_3-Al_2O_3. Both Cr and Al are depleted in the alloy near the metal-oxide interface, enriching this interface with Ni and Co. The dark layer above the oxide scale appears to be residual Na_2SO_4 and $MgSO_4$ containing Cr and Al compounds. The Cr, Al, S, and O maps suggest that some of the Cr and possibly some Al in the remaining sulfate are oxides.

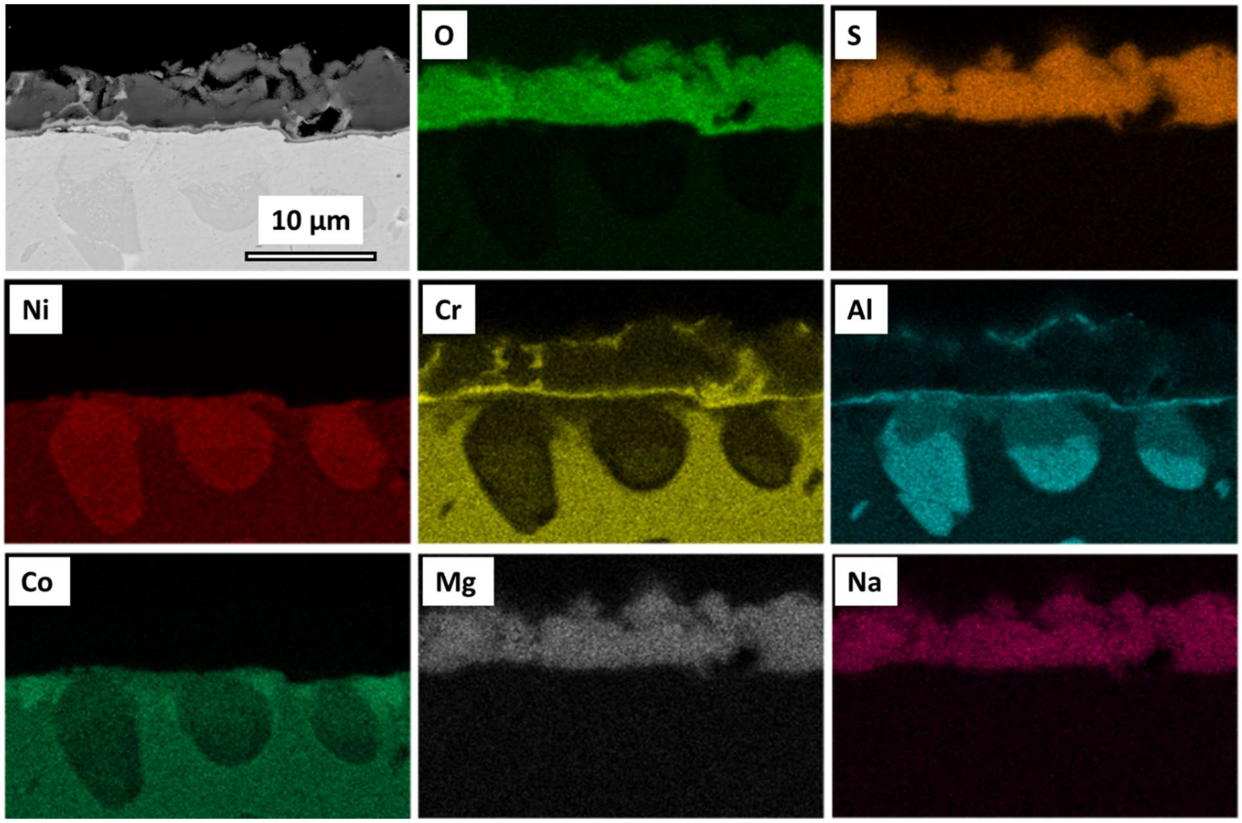

Figure 60. EDS of Alloy 2 after tube furnace exposure at 700 °C with 4.6 x 10^{-6} mol/cm^2 Na_2SO_4 + 9.3 x 10^{-6} mol/cm^2 $MgSO_4$ and 1000 ppm SO_2 in O_2 with Pt catalyst for 48 h

Figure 61 shows that Alloy 3 forms a primarily Cr_2O_3 scale. While Al is not detected in the thin oxide, both Cr and Al are present in the thicker Na_2SO_4-$MgSO_4$ layer above. The EDS maps suggest some Cr and Al in the sulfate are oxides, like in the Alloy 2 EDS maps. There is an Al depletion layer that is approximately 3 µm deep in the alloy below the scale. The alloy at this interface is slightly enriched with Ni and Co.

All alloys exposed to $MgSO_4$ and mixed Na_2SO_4-$MgSO_4$ deposits in the tube furnace for 48 h showed no water-soluble Ni^{2+}, $Co^{2+/3+}$, $Cr^{3+/6+}$, Al^{3+}, or Y^{3+} above the ICP-OES detection threshold (0.1 ppm in the water digestion, corresponding to 1.25 µg/cm^2). Water soluble Na^+ and Mg^{2+} were detected by ICP-OES, as expected for sulfates.

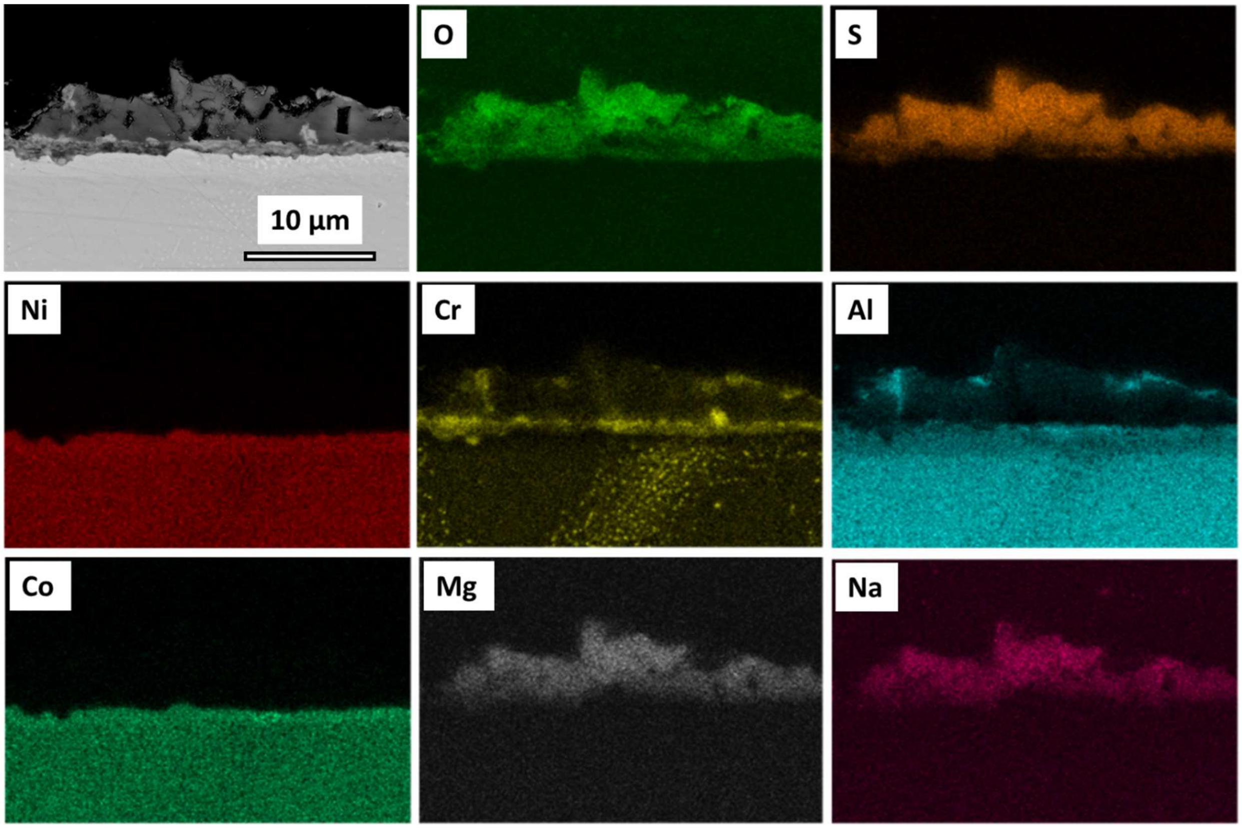

Figure 61. EDS of Alloy 3 after tube furnace exposure at 700 °C with 4.6 x 10^{-6} mol/cm^2 Na_2SO_4 + 9.3 x 10^{-6} mol/cm^2 $MgSO_4$ and 1000 ppm SO_2 in O_2 with Pt catalyst for 48 h

4.5.8 Differential scanning calorimetry of salt mixtures with and without $Y_2(SO_4)_3$

Differential scanning calorimetry (DSC) cooling curves for a salt mixture with and without $Y_2(SO_4)_3$ are shown in Figure 62. The salt composition of 65.1 Na_2SO_4, 27.1 $MgSO_4$, 5.7 $CaSO_4$, and 2.2 K_2SO_4 (mol%) was determined empirically by ICP-OES measurements of deposits on Al_2O_3 samples exposed in the LVBR to artificial ocean water for 336 h (2 weeks). DSC measurements during cooling proved more accurate than during heating due to the homogenization of the salt mixtures upon melting. The addition of $Y_2(SO_4)_3$ reduced the solidification temperature of the mixture by approximately 70°, from 790 °C to 720°C.

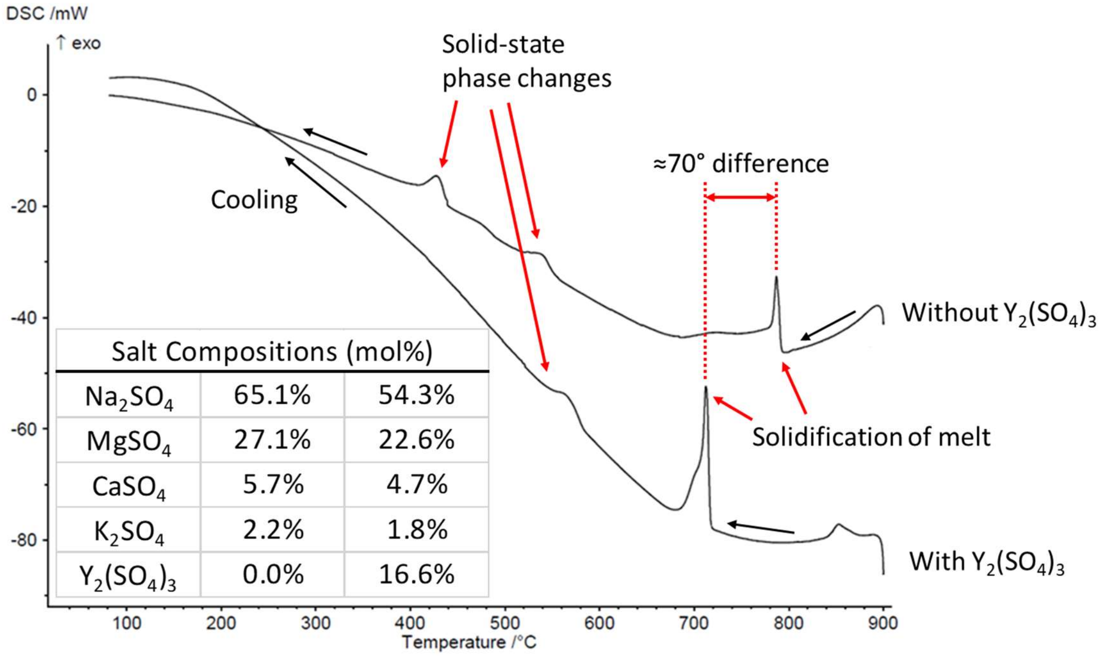

Salt Compositions (mol%)		
Na_2SO_4	65.1%	54.3%
$MgSO_4$	27.1%	22.6%
$CaSO_4$	5.7%	4.7%
K_2SO_4	2.2%	1.8%
$Y_2(SO_4)_3$	0.0%	16.6%

Figure 62. DSC cooling curves showing solidification of salt melts with and without addition of $Y_2(SO_4)_3$

4.6 Discussion

4.6.1 The effect of Al, Cr, and relative amounts of γ and β on alloy LTHC in complex deposits

The excellent performance of Alloy 1 is consistent with previous understanding that increasing Cr concentrations are generally beneficial for resistance against LTHC [34,36,54,79,87–89]. While Alloy 1 has half the Al concentration of Alloy 3, it is nevertheless better able to maintain a protective scale than the relatively Al-rich, Cr-poor Alloy 3. This is consistent with the third element effect [5–7,90], as described in the introduction. Alloy 2, with the least amount of Cr + Al, was the worst performing alloy in all furnace exposure conditions. Alloy 3 was the worst performing material in all the LVBR exposures. This is consistent with it having the lowest Cr content as well as its high yttride phase fraction. The phase fraction of yttrides, and therefore resulting corrosion, depends partly on the β and Al content of the alloy. However, the effect of yttrium/yttrides and the secondary dependence on alloy composition will be discussed in the next section.

Strangely, Figure 49 and Figure 59 (Alloy 1) show preferential attack of the Cr-rich γ phase over the Al-rich β phase. Figure 59 shows that the reaction product is rich in Cr, O, and S. This could simply be a result of the high Co content in γ, resulting in more $CoSO_4$ locally and thus more corrosion. Another possibility is that while Cr is globally beneficial, it may have some deleterious effects on the microstructural length scale. Recently, a synergistic fluxing model has been proposed in which dissolution of Cr_2O_3 raises the pSO_3 at the solid-melt interface, increasing the acidic fluxing of NiO and CoO [67,91]. It may be possible that local conditions in the melt above γ phase, where more Cr_2O_3 is present, is more acidic. The problem may be compounded by the enrichment of Co within γ due to Cr depletion, resulting in greater susceptibility to the formation of CoO and $CoSO_4$ in a locally acidified environment. However, Al_2O_3 has a similar acid-base character to Cr_2O_3 [29,30,92] and so it is not clear why Cr_2O_3 would cause more significant synergistic fluxing.

Nevertheless, Cr is a net benefit to the LTHC resistance of the model alloys. Acid-base reactions, third element effects, and many other processes, some competing, occur simultaneously during hot corrosion. The net effect of changing a variable, such as Cr content, is of most interest in technological applications. The LVBR and furnace exposures demonstrate the requirement for Cr in service, although Cr may play a subtle, deleterious role on initiation mechanisms and local conditions on the microstructure scale. The present study suggests that the more recent and more nuanced understanding of Cr is worthy of consideration.

4.6.2 The effects of yttrium and yttrides

The effect of alloying with Y on LTHC exposures was a function of the yttride phase fraction. While all model alloys contained 0.1 wt% Y and yttride precipitates, only the yttrides of Alloy 3 were observed to be initiation sites for corrosion. This shows that the effect of Y on LTHC is dependent on the amount of Y dispersed in metallic solid solution phases (e.g. β and γ) compared to the amount present in Y-rich intermetallic or oxide phases within the metal. Y proved to be detrimental when present as Y-rich precipitates due to these phases' strong reactivity to form oxides, sulfides, and/or sulfates. The importance of the Y distribution and the dangers of "over-doping" with Y have been recognized in past studies. Kuenzly and Douglass observed the formation of yttrium-aluminum garnet (YAG) on Ni_3Al-0.5 wt% Y during oxidation in air at 900-1200 °C [93]. They reported enhanced spallation and thus faster oxidation kinetics when YAG was present near the metal-oxide interface, which they attributed to increased stresses in the scale due to YAG formation. Gheno and Gleeson observed an analogous effect due to Y-Al oxide particles in NiCoCrAlY exposed to fly ash at 1100 °C [72]. Task, Gleeson, Pettit, and Meier report initiation of corrosion at Y- and Hf-rich phases in NiCoCrAlY and NiCoCrAlY + Si, Hf alloys at 700 °C LTHC conditions [79].

The quantitative ICP-OES results in the present study expand on these previous observations. The agreement between enrichment of an element in the salt deposit/corrosion product and its corresponding stability, as shown in Figure 55, suggests that the alloying elements form sulfates under the LTHC test conditions. The formation of sulfates corresponds to primarily acidic fluxing of oxides, as expected at the relatively high pSO_3 of 3.6×10^{-4} atm in the furnace environment. The exponential dependence of sulfate concentrations on the free energies of reaction likely reflects the exponential dependence of the sulfation reaction's equilibrium constant. However, an actively corroding system is not yet at equilibrium. Lack of activities for the sulfates in solution with Na_2SO_4 would also make an equilibrium constant calculation dubious.

Jones, Nordman, and Gadomski demonstrated that Y_2O_3 formed $Y_2(SO_4)_3$ in at 850-950 °C and 6 x 10^{-6} atm SO_3 only in the presence of a Na_2SO_4 deposit [94]. Y_2O_3 formed $Y_2O_2SO_4$ in the absence of a deposit in the same conditions. These results justify the use of $Y_2(SO_4)_3$ thermochemical data for Figure 55 instead of that for $Y_2O_2SO_4$. The fit to the trendline also suggests that $Y_2(SO_4)_3$ is the reaction product, although data for $Y_2O_2SO_4$ formation at 700 °C are not available for comparison.

The elevated $NiSO_4$ and $CoSO_4$ content for alloys that corroded confirms the importance of Ni and Co sulfation on establishing a low-melting mixture for subsequent LTHC. The $Y_2(SO_4)_3$ content of the LVBR sample surfaces is greater than that of $NiSO_4$ and $CoSO_4$, while the $Y_2(SO_4)_3$ content of the furnace samples is lower than that of $NiSO_4$ and $CoSO_4$. This result likely has two explanations. The first is because the LVBR exposures were thermally cycled, they exhibited greater spallation around corroding yttrides and therefore greater sulfation at locations containing yttrides. Figure 52 is representative of the corroding furnace sample Y-rich phases in that the oxide scale buckled but did not spall. Reduced spallation around yttrides in furnace testing likely resulted in reduced formation of $Y_2(SO_4)_3$. The second explanation for greater $Y_2(SO_4)_3$ in the LVBR than the furnace is that corrosion in the LVBR was typically localized at yttride phases while furnace corrosion was more uniform. The reason for localized LVBR corrosion and uniform furnace corrosion is probably due to the formation of an oxide in the LVBR prior to the buildup of a significant Na_2SO_4 deposit. Therefore, corrosion selectively initiates only at locations where the pre-existing scale is disrupted, such as at reacting yttrides. Furnace exposures with deposits present at the beginning of testing likely never had to time to develop a protective scale in the first place and were therefore not as susceptible to factors that disrupt pre-existing scales.

The effect of corroding Y-rich phases buckling and spalling the scale is clear. A second possible effect of Y on LTHC is the reduction of the deposit melting point. The role of $NiSO_4$ and $CoSO_4$ on sulfate melting point reduction is well-established. The significant $Y_2(SO_4)_3$ contents reported in Figure 37 and Figure 53, which rivals concentrations of $NiSO_4$ and $CoSO_4$, suggest a greater role for $Y_2(SO_4)_3$ on deposit chemistry than previously believed. Note that the ICP-OES results are for concentrations averaged over the entire specimen surface. The salt chemistry varies across the sample surface and this is especially likely for $Y_2(SO_4)_3$ because it originates from localized yttride phases. Local $Y_2(SO_4)_3$ concentrations may be greater than the reported averages. This makes it difficult to estimate a realistic $Y_2(SO_4)_3$ concentration, but the DSC results in Figure 62 show that even just 15 mol% $Y_2(SO_4)_3$ lowered the solidification temperature of a mixed sulfate from 790 °C to 720 °C.

There is no complete $Y_2(SO_4)_3$-Na_2SO_4 phase diagram in the published literature. Eysel, Höfer, Keester, and Hahn report a partial, preliminary $Y_2(SO_4)_3$-Na_2SO_4 phase diagram that shows a eutectic temperature of 785 °C (99 °C lower than the melting point of pure Na_2SO_4) at 20 mol% $Y_2(SO_4)_3$ [95]. Jones, Nordman, and Gadomski report a melting point of approximately 800 °C for 25 mol% $Y_2(SO_4)_3$ – 75 mol% Na_2SO_4 [94]. These results are similar to the present study's 70° C melting point depression for 16.6 mol% $Y_2(SO_4)_3$ in a mixed sulfate despite the differences in salt composition. Figure 62 shows that $Y_2(SO_4)_3$ in a mixed sulfate deposit (containing Na_2SO_4, $MgSO_4$, $CaSO_4$, and K_2SO_4 from seawater) may lower the melting point to nearly 720 °C, even without $NiSO_4$ and $CoSO_4$. This may reduce the Ni and Co sulfation necessary for a melt at 700 °C, increasing corrosion. It also raises the possibility of melting at LTHC conditions in the absence of $NiSO_4$ and $CoSO_4$, although such a melt may be limited to only locations with a sulfated yttrium precipitate.

Microscopy of partially corroded yttrides reveals clues about the mechanism by which yttrides decompose. Figure 43 shows that Alloy 3 yttrides decompose into Y- and Ni-rich sulfides and a β metallic solid solution as S diffuses into the alloy. Al_2O_3 is formed as O diffuses inward, causing a flux of Al outward. This causes depletion of Al in the sulfide-metal reaction product that has not yet oxidized, transforming the β matrix into γ'. Further inward diffusion of O results in the sulfation of the Y-rich sulfides. The enrichment of $Y_2(SO_4)_3$ at the solid-gas interface suggests an outward diffusion of $Y_2(SO_4)_3$ through the porous, nonprotective corrosion product, where it may encounter sulfates (both from the environment and from the alloy) and assist in maintaining a melt. In summary, the corrosion morphology and elemental distribution in Figure 41 and Figure 42 may be explained by the following proposed reaction sequence: decomposition of the yttrides by S to Y-rich sulfides in the interior of the alloy, subsequent sulfation by the inward diffusion of O, and lastly transport of $Y_2(SO_4)_3$ upwards through the cracked and defective corrosion product towards the solid-gas interface. Near the solid-gas interface, $Y_2(SO_4)_3$ contributes to lowering the melting temperature of the sulfate deposit. Simultaneously, the volume expansion resulting from oxidation, sulfidation, and sulfation disrupt the formation and reformation of a protective scale.

The yttride problem is related to the metallurgy of the NiCoCrAlY alloys. Alloys 1 and 2 demonstrate that the phase fraction of yttrides may be reduced with reduced Al and β content. The Scheil solidification simulation in Figure 32 suggests that γ solidification is less prone to rejection of Y into the liquid than β solidification. This also means that the amount of Y enrichment in the liquid is sensitive to processing conditions and coating application methods that differ in rates of cooling. The favorable Alloy 1 and Alloy 2 results, with a more homogeneous distribution of Y than in Alloy 3, suggest that Y may not necessarily be detrimental in LTHC conditions. However, LTHC is particularly sensitive to the Y distribution because of the tendency to form Y sulfates.

4.6.3 The effect of Mg^{2+}

The differences between the LVBR and furnace testing results with mixed Na^{+}-Mg^{2+} suggest that the effect of Mg^{2+} is not straightforward. The published literature also implies a complex Mg^{2+} effect that may vary dramatically with different materials and exposure conditions. Jones and Williams performed thermogravimetric analysis (TGA) of CoCrAlY coupons in SO_3-containing atmospheres at 700 °C with pure Na_2SO_4 deposits and 50 mol% $MgSO_4$-50 mol% Na_2SO_4 deposits [77]. They observed that 50 mol% $MgSO_4$-50 mol% Na_2SO_4 deposits resulted in half the corrosion rate of pure Na_2SO_4 within the first 24 h of exposure. The corrosion rates for both deposits then became roughly equal between 24 and 48 h. The authors attributed this to delayed sulfation of Co_3O_4 in the presence of $MgSO_4$. Rahmel, Wu, Schmidt, and Schorr performed electrochemical measurements of Ni- and Co-base alloys IN-100, IN-738 LC, IN-597, and IN-939 in Na_2SO_4 in mixed $(Na_2, Ca, Mg)SO_4$ and $(Na, K)_2SO_4$ electrolytes at 800 and 900 °C and found that the presence of $MgSO_4$ inhibited basic fluxing of alloys and had little effect on acidic fluxing [96,97]. They attribute the inhibition of basic fluxing by $MgSO_4$ to precipitation of a MgO layer, which is insoluble in basic melts. However, the tube furnace atmosphere of 0.1 wt% SO_2 in O_2 (Pt-catalyzed) of this present work is likely acidic. Tang and Gleeson reported that LTHC with a mixed Na_2SO_4-$MgSO_4$ deposit on PWA 1484 (Bal. Ni/5 Cr/2 Mo/6 W/3 Re/8.7 Ta/5.6 Al/10 Co/0.1 Hf) resulted in corrosion rates 3-4 times greater than LTHC of PWA 1484 and pure Na_2SO_4 [51,75]. Shifler attributed the accelerated corrosion rate of the alloy with mixed Na_2SO_4-$MgSO_4$ to the lower melting temperature and greater liquid fraction of the mixed salt [51].

The effect of Mg^{2+} on corrosion in the LVBR is more straightforward than the furnace results. Not only do mixed Mg^{2+}-Na^+ exposures increase the amount of corrosion compared to pure Na^+, but the corrosion morphology of Alloy 3 changes with additions of Mg^{2+} in Na^+ in the LVBR. In the pure Na^+ deposit, corrosion was localized to areas with corroding yttrides near the solid-gas interface. As explained previously, the corroding yttrides disrupt the scale and form $Y_2(SO_4)_3$, which may lower the melting point along with $NiSO_4$ and $CoSO_4$. This restricts melting and hot corrosion to localized areas that contain these Y-rich phases. The more uniform corrosion of Alloy 3 in the mixed Mg^{2+}-Na^+ deposit suggests that a lower melting salt mixture was obtained on larger area fractions of the sample surfaces. Alloys 1 and 2 corroded in the mixed deposit but not in the pure Na_2SO_4 LVBR environment. The most natural explanation of the LVBR results is that Mg^{2+} additions to Na^+ resulted in greater corrosion by satisfying the conditions for a eutectic melt on larger surface area fractions of the alloys.

The incorporation of Mg^{2+} into the scale of the LVBR alloys probably had little effect on corrosion mechanisms. The (Ni, Co, Mg)O rocksalt scale is porous and nonprotective; it likely does not fulfill the role of a semi-protective MgO layer as described by Rahmel, Wu, Schmidt, and Schorr.

Their analysis showed that Mg^{2+} played no protective role in acidic melts. The SO_3-containing atmospheres of the LVBR and furnace likely maintain relatively acidic melt chemistries. Also, Rahmel, Wu, Schmidt, and Schorr's electrochemical tests were performed on samples exposed to sulfates for only 100 h and in the absence of thermal cycling. For longer times (500 h in the present study) with thermal cycling, protective Al_2O_3 or Cr_2O_3 will eventually spall or otherwise fail in some locations, resulting in loss of any MgO outer layer and the exposure of bare metal to the environment. Once corrosion begins and a porous NiO/CoO layer is formed, dissolution of MgO into this nonprotective oxide probably confers no benefits or detriments. ICP-OES measurements also show water-soluble Mg^{2+}, which suggests that some Mg^{2+} was not incorporated into the NiO/CoO scale, leaving some Mg^{2+} on the surface as $MgSO_4$ and resulting in a lower deposit melting point. In short, service environments (longer exposure times with thermal cycling in the presence of SO_3(g)) might not benefit from a MgO layer as proposed by Rahmel, Wu, Schmidt, and Schorr.

The most significant difference between the LVBR and tube furnace environments was probably the deposit composition. The $MgSO_4$ content in the LVBR deposits was lower than that in the furnace deposits because of the incomplete conversion of MgO to $MgSO_4$. ICP-OES of the LVBR deposits on Al_2O_3 pins indicates a maximum $MgSO_4$ concentration of 50 mol% $MgSO_4$-50 mol% Na_2SO_4. The ICP-OES results are discussed in greater detail in Section 5.6 (see Figure 70). The tube furnace deposit composition was 67 mol% $MgSO_4$-33 mol% Na_2SO_4. This put the LVBR deposit composition near the eutectic composition (100% liquid at 700 °C) while the tube furnace deposit composition is in a two-phase region containing both solid and liquid. The compositions of the two environments are shown in Figure 63. The lever rule gives a 36 mol% liquid fraction for the tube furnace composition.

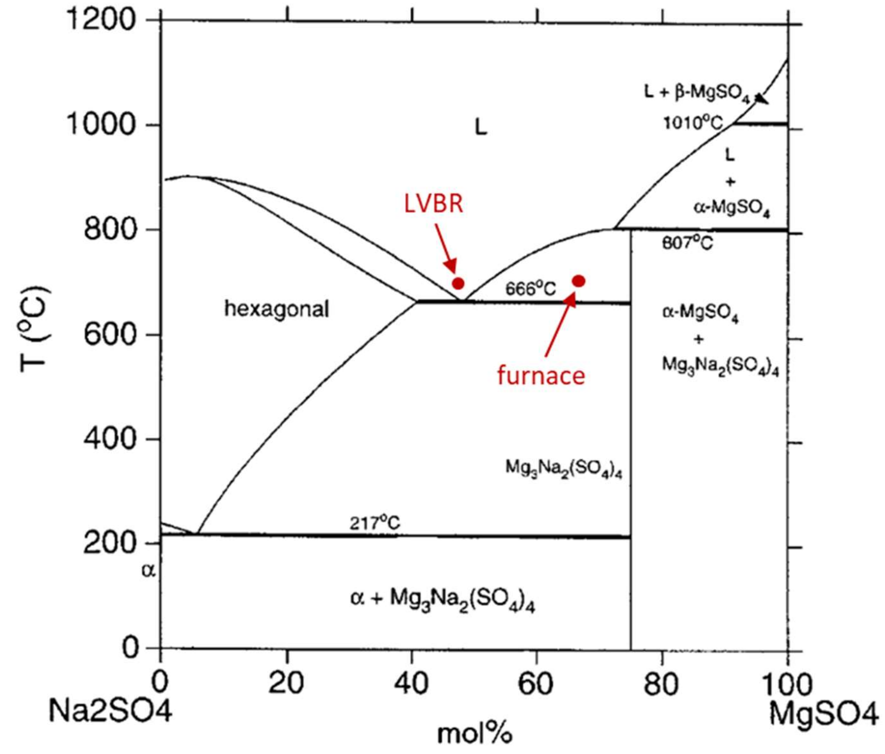

Figure 63. Compositions of deposits in the LVBR and tube furnace environments shown (in red) on the Na_2SO_4-$MgSO_4$ pseudobinary phase diagram. Reprinted by permission from Springer Nature Customer Service Centre GmbH: Springer Journal of Phase Equilibria "Thermodynamic assessment of the K_2SO_4 -Na_2SO_4-$MgSO_4$-$CaSO_4$ system" by Du, H., Copyright (2000) [58].

Therefore, only 36 mol% of the tube furnace deposits was liquid while the LVBR deposits may have completely melted after sufficient $MgSO_4$ formation. The amount of corrosion is known to decrease with decreasing deposit liquid fraction [51], explaining the lack of corrosion in the tube furnace compared to the LVBR.

As explained previously, basic conditions are hypothesized to result in an insoluble MgO film on sample surfaces that are resistant to fluxing. This is the explanation invoked by Jones and Williams for the temporary inhibiting effect of $MgSO_4$ on CoCrAlY in an atmosphere with a pSO_3 of $1x10^{-4}$ atm, not much lower than that of the present study (estimated pSO_3 of $3.6x10^{-4}$ atm). Note that a water-insoluble layer was detected on Alloys 2 and 3 that was rich in Mg and O (see Figure 60 and Figure 61), although Na and S were also detected in the layer. However, exposures of NiAl and NiAlCr to mixed Na_2SO_4-$MgSO_4$ deposits at 700 °C in an atmosphere of 1000 ppm SO_2 in O_2, catalyzed with Pt (same conditions as the present study) for 20 h resulted in hot corrosion and no detectable Mg-rich layer [67]. Gheno, Azar, Heuer, and Gleeson explain that this due to a melt that is sufficiently acidic in the relatively high pSO_3 environment, as the same exposures performed in the absence of SO_x resulted in reduced corrosion. The difference may also be related to additional effects of alloy content, as the corroded NiAl and NiAlCr contain significantly less Cr than the more resistant NiCoCrAlY and CoCrAlY alloys. This is consistent with the dramatic increase in corrosion rate of PWA 1484 (approximately 5 wt% Cr) as observed by Tang and Gleeson.

Lastly, the water vapor content of the LVBR and tube furnace atmospheres were different. The LVBR contains a combustion environment with an estimated pH_2O of 6.35×10^{-2} atm, assuming equilibrium (the details of this estimation are explained in section 5.6). The tube furnace gases flowed through a desiccant to reduce/control the amount of water vapor in the stream. The transition from primarily Al_2O_3 to primarily Cr_2O_3 scales in the presence of mixed Na_2SO_4-$MgSO_4$ in the tube furnace is notable because Cr_2O_3 is known to form volatile $CrO_2(OH)_2(g)$ in the presence of water vapor, reducing its protectivity [5,6]. Future tube furnace exposures should be conducted in atmospheres with varying H_2O content to evaluate the dependence of mixed deposit corrosion on water vapor.

The prior discussion involved many variables that may explain the differences in resulting corrosion in mixed deposits. The differences in the test conditions, materials, and observed corrosion for mixed Na_2SO_4-Mg^{2+} deposits at 700 °C are summarized in Table 12.

Table 12. Summary of test conditions, materials, and results for mixed Na_2SO_4-Mg^{2+} LTHC experiments in this work and the literature

	LVBR	Furnace	Jones [77]	Gheno [67]	Tang [75]
$MgSO_4$ content of deposit	50 mol%	66.7 mol%	50 mol%	48 mol%	Unknown
Time (h)	500	48	0-50	20	0-100
pSO_3 (atm)	≤ 5.9×10^{-3} atm	≤ 3.6×10^{-4} atm	≤ 1.3×10^{-4} atm	≤ 3.6×10^{-4} atm	Unknown
Water vapor	Y (combustion)	N (dry air)	N (dry air)	N (dry air)	Unknown
Alloy	NiCoCrAlY	NiCoCrAlY	CoCrAlY	NiAl and NiAlCr	PWA 1484
Cr content of alloy (wt%)	16-30	16-30	22	5 (NiAlCr)	5
Thermal cycling	Y (1 h. R.T. every 24 h.)	N	N	N	N
Deposition rate	≈ constant at 3.9×10^{-4} mg cm^{-2} h^{-1}	2 mg/cm^2 applied at t=0	4-7 mg/cm^2 applied at t=0	2.8 mg/cm^2 applied at t=0	Unknown
Insoluble Mg^{2+}-rich layer	Only within porous NiO/CoO	Observed for Alloys 2 & 3	Hypothesized but not observed	Not observed	Unknown
Effect of Mg^{2+} on corrosion rate	Increased	Decreased	Decreased	NiAl: Increased, NiAlCr: no change	Increased

4.7 Conclusions

The well-known beneficial effect of Cr (and by extension, Cr-rich phases such as γ) in LTHC was confirmed. Preferential attack of the γ phase was observed for the tube furnace exposures. It is proposed that this is either an effect of the relatively high Co concentration in γ and/or local acidification of the melt due to dissolution of Cr_2O_3. Increasing amounts of β and Al typically increased the amount of corrosion. This is partly due to the lack of Cr in the β phase as well as the increased tendency of the most Al-rich to form reactive yttrides. The yttrides corrode in the presence of Na_2SO_4 through a multistep reaction process involving decomposition into Y-rich sulfides and subsequent formation of $Y_2(SO_4)_3$. The large molar volume increase upon yttride corrosion disrupted the scale by causing buckling, cracking, and spallation. DSC measurements suggest that $Y_2(SO_4)_3$ may depress the melting point of the sulfate deposit, resulting in greater liquid fraction and corrosion.

Mg^{2+} additions to Na^+ resulted in increased corrosion of all three model alloys in the LVBR compared to pure Na^+. Alloys 1 and 2 corroded in the mixed Mg^{2+}-Na^+ environment while no corrosion occurred during pure Na^+ exposures. Mixed Mg^{2+}-Na^+ caused increased corrosion of Alloy 3 over a greater surface area of the alloy. Corrosion in the mixed deposit was not limited to locations containing yttrides, as is the case for pure Na^+ exposures. These results are consistent with a greater liquid fraction of the deposits due to the Na_2SO_4-$MgSO_4$ eutectic. In the tube furnace, none of the alloys corroded when exposed to the Na_2SO_4-$MgSO_4$ mixed deposit at 700 °C for 48 h. Alloys 1 and 3 formed primarily Cr_2O_3 scales and Alloy 2 formed a mixed Cr_2O_3-Al_2O_3 scale. All three alloys are primarily Al_2O_3 formers, and so the presence of $MgSO_4$ apparently caused a transition to Cr_2O_3-rich scales. The difference in corrosion between the LVBR and tube furnace environments is primarily explained by differences in deposit composition. The tube furnace deposit composition of 67 mol% $MgSO_4$-33 mol% Na_2SO_4 is only 36 mol% liquid at 700 °C. The LVBR deposit composition of approximately 50 mol% $MgSO_4$-50 mol% Na_2SO_4 is near the eutectic composition and is 100% liquid at 700 °C. Thermal cycling, longer exposure times, water vapor, and replenishing deposits in the LVBR may also have contributed to greater corrosion than in the furnace. Future work should involve tube furnace exposures of alloys to deposits of varying $MgSO_4$ and Na_2SO_4 content. Tube furnace exposures should also be performed with longer exposure times, with and without thermal cycling, and with varying amounts of water vapor to determine the effects of these variables on mixed-deposit corrosion.

The accelerated corrosion due to Mg^{2+} additions to Na_2SO_4 deposits in the LVBR possibly explain the corrosion the marine turbine blades by CMAS-like CaO- and MgO-containing deposits. While the temperature beneath the platform (≤ 700 °C) is well below the temperature at which CMAS forms a glassy melt (1100-1200 °C), the reaction of MgO to form $MgSO_4$ (and, similarity, reaction of CaO to form $CaSO_4$) may result in a mixed Na_2SO_4-$MgSO_4$ melt. The detection of both water-soluble Mg^{2+} and MgO on LVBR pin surfaces suggests this may occur despite incomplete conversion of the oxides to sulfates. XRD of under-platform turbine blades deposits (Figure 14) shows $CaSO_4$. Also, some water-soluble Mg^{2+} and Ca^{2+} were detected in the water digestion of the turbine blade (Figure 15). These observations indicate that some $MgSO_4$ and $CaSO_4$ may be present on the turbine blades and that the formation of low-melting complex sulfate mixtures is a viable explanation.

5.0 Deposit formation

5.1 Introduction

Deposits on the shipboard engine airfoil described in section "2.1 Characterization of service hardware" had higher concentrations of Na_2SO_4 and the corrosion morphologies were consistent with familiar Na_2SO_4-induced corrosion mechanisms. FactSage modeling predicts these compositions relatively accurately, as measured by ICP-OES. However, the deposit amount was small and the resulting corrosion was comparatively less severe than the Ca- and Mg-rich deposits elsewhere. Empirical findings, together with thermochemical calculations, suggest that higher temperatures in combustion gases and/or minimal sulfur in the cooling channels favor the formation and retention of deposits other than Na_2SO_4. This is consistent with recent sentiment that deposits other than Na_2SO_4 are more relevant for hot corrosion challenges today [44,50,51,98] .

5.2 Knowledge gaps

The most complete studies on the hot corrosion deposition process were performed with the Mach 0.3 Burner Rig at NASA Glenn Research Center [99–103]. Rosner, Fryburg, Kohl, Chen, Stearns, Santoro, and Gökoğlu found that a Chemically Frozen Boundary Layer (CFBL) model accurately modeled deposition rates in the burner rig. The CFBL model, shown schematically in Figure 64, assumes that the rate-limiting step of the deposition process is the diffusion of depositing species across a gas boundary layer (BL) on a surface. The critical variables to estimate are therefore the concentration of the depositing species i at the free gas stream-BL interface, $\omega_{i,e,}$ the concentration of depositing species i at the surface/wall, $\omega_{i,w}$, the diffusivity of each species in air (assumed to be N_2), $D_{i,\ N2}$, and the dimensionless mass transport Sherwood number, Sh_i, discussed in more detail below. The flux of a depositing species, J_i, is given by Equation 16. The density of the external combustion gas stream is ρ and the characteristic length of the sample surface is L (for a cylindrical pin, this is the pin diameter). Equation 16 is analogous to Fick's First Law of Diffusion except that it allows for transport to occur through convective mixing in addition to diffusion. The relative contributions of mixing and diffusion are contained within the Sherwood number. The calculations and results are discussed in greater detail in the Results section.

$$J_i = \frac{-\rho D_{i,N_2}}{L} Sh_i(\omega_{i,e} - \omega_{i,w}) \tag{16}$$

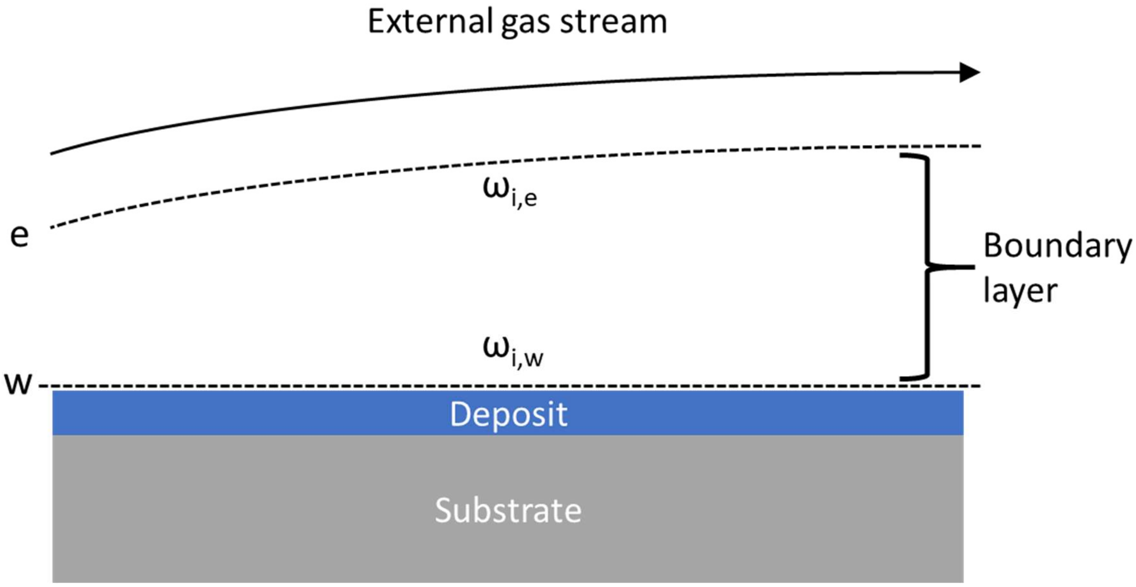

Figure 64. Schematic of the CFBL model

The CFBL model assumes that no chemical reactions occur within the boundary layer. It also assumes a pseudo-steady state process and that the gas composition at both interfaces is fixed. The external stream-BL interface (e) composition may be estimated by calculating the equilibrium composition of the external stream (e.g. by Gibbs free energy minimization). The BL-sample surface gas interface (w) composition may be assumed to be zero if $\omega_{i,w} << \omega_{i,e}$ or estimated using the equilibrium vapor pressures of the condensed deposit species. It is assumed that inward-diffusing precursor species such as NaCl(g) and NaOH(g) react with excess SO_x and O_2 at the surface to form the expected deposit, such as Na_2SO_4.

Rosner, Fryburg, Kohl, Chen, Stearns, Santoro, and Gökoğlu estimated the external stream-BL interface composition via Gibbs free energy minimization using NASA's Chemical Equilibria for Applications software [104]. The assumption of gas phase chemical equilibrium is dubious considering the short residence time of gas in a gas turbine, but this was the best available method at that time. More recent experiments by Schofield, Steinberg, and Hynes suggest that the dominant Na and K gas species in a turbine are NaOH and KOH [39–41]. Therefore, calculations may be simplified by only considering boundary layer diffusion of NaOH, KOH, and Mg- and Ca-containing species across the boundary layer to form deposits by reaction with excess SO_x and O_2. This will allow for the rate of accumulation and relative amounts of Na, Mg, K, and Ca species in the deposit to be determined as a function of service conditions.

5.3 Objective

The effects of Mg salts from seawater have been investigated in the previous chapter; however, the factors that determine the relative amounts of Na, Mg, K, and Ca in hot corrosion deposits require exploration. The LVBR provides a means of examining the compositions, rates of formation, and formation mechanisms of deposits derived from the mixture of seawater and marine fuel combustion gas mixtures at 700 °C. The CFBL model used previously for NASA's Mach 0.3 Burner Rig [99–103] is applied to the LVBR with injected seawater containing salts of Na, Mg, K, and

Ca. The model allows for determination of how environmental factors such as temperature and pressure affect the resulting deposit composition. Experimentally observed LVBR deposits are compared to those previously observed on the actual marine turbine blades. The accuracy and applicability of the CFBL model to predict deposit formation in the LVBR and in actual gas turbines is discussed.

5.4 Methodology – analytical model

Thermochemical predictions, mass transport models, and burner rig experiments were all used to understand the composition and formation of hot corrosion deposits. A first approximation for predicting deposit formation is performing a Gibbs energy minimization to predict the equilibrium composition of the combustion gas stream, noting the prediction of any condensed phase species. This procedure was used in the preceding section of the characterization of gas turbine blades. The Gibbs energy minimization was performed using the FactSage equilibrium module. The same method was again used for the LVBR environment. A mass balance of the burner rig input streams (fuel, air, and salt solution contaminant) was performed to obtain the elemental composition of the LVBR combustion gas. Appendix A shows mass balances for different saltwater contaminant compositions. The equilibrium module with the FactPS database was then used to find the equilibrium composition at the LVBR operating temperature of 700 °C.

Next, the mass balance of the burner rig was used to predict the dewpoints of possible Na, K, Ca, and Mg compounds as functions of temperature and pressure. This was accomplished by targeting the temperature at which a condensed species first appears for a given pressure. The process was repeated for each expected depositing compound for 1-40 atm. This allowed for analysis of the driving forces for deposit formation over ranges of temperature and pressure that are relevant for gas turbines but not attainable in the LVBR.

Of course, the assumption of global thermochemical equilibrium in a gas turbine is a crude approximation and is insufficient for modeling deposition rates. The Chemically-Frozen Boundary Layer (CFBL) model used previously by Rosner, Fryburg, Kohl, Chen, Stearns, Santoro, and Gökoğlu [99–103] to model burner rig deposit formation as a vapor deposition process, rate-controlled by the diffusive and convective transport of depositing species across a gas boundary layer was also used here. A schematic of the gas stream and boundary layer around an LVBR sample is shown in Figure 65. The driving force for diffusion of depositing species is given by the concentration gradient across the boundary layer, $\Delta\omega$. The previously-mentioned authors estimated the concentration of Na, Mg, K, and Ca species by performing a Gibbs energy minimization similar to that used in the present FactSage analyses. They then computed the diffusivity of each species and the resulting flux to the sample surface. The present work assumes all Na and K gas species are NaOH(g) and KOH(g) because of the laser spectroscopy work of Schofield, Steinberg, and Hynes that indicated that hydroxides are the dominant alkali metal species in gas turbine combustion streams [39–41]. Mg and Ca are assumed to be MgO(g) and CaO(g), as these are the Mg- and Ca-rich solid compounds detected in the LVBR deposits. Both the present and previous CFBL models assume that these gaseous species (NaOH(g), KOH(g), MgO(g), and CaO(g)) react with excess SO_x and O_2 at sample surfaces to form solid sulfates. It is also assumed that these surface reactions occur significantly faster than boundary layer diffusion and may be neglected.

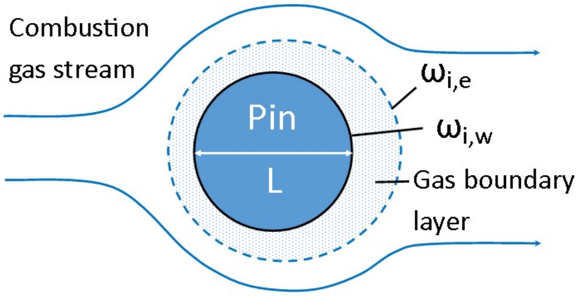

Figure 65. Schematic of flow stream around an LVBR pin sample in cross-section

The overall governing equation for the flux of a depositing species i is shown in Equation 17. This is a diffusion equation that contains the Sherwood number, which includes the relative effects of both diffusive and convective transfer. For a cylinder in crossflow, it is estimated using the Churchill-Bernstein Equation [105], Equation 18. It is a function of the Reynolds number (given by Equation 19) and Schmidt number (given by Equation 20) and is valid when $Re_i*Sc_i \geq 0.2$. Re is the ratio of inertial forces to viscous forces within the fluid and Sc is the ratio of momentum (viscous) transport to Fickian transport (i.e. diffusion via a concentration gradient). Because the surface reactions of depositing species with SO_x and O_2 occur quickly, it is assumed that $\omega_{i,e} >> \omega_{i,w}$ and Equation 17 simplifies to Equation 21.

$$J_i = \frac{-\rho D_{i,N_2}}{L} Sh_i(\omega_{i,e} - \omega_{i,w}) \tag{17}$$

$$Sh_i = 0.3 + \frac{0.62 Re_i^{1/2} Sc_i^{1/3}}{[1 + (0.4/Sc_i)^{2/3}]^{1/4}} \left[1 + \left(\frac{Re_i}{28200}\right)^{5/8}\right]^{4/5} \tag{18}$$

$$Re_i = \frac{\rho u L}{\mu_i} \tag{19}$$

$$Sc_i = \frac{\mu_i}{\rho D_{i,N_2}} \tag{20}$$

$$J_{NaOH} \approx \frac{-\rho D_{i,N_2}}{L} Sh_i(\omega_{i,e}) \tag{21}$$

The diffusion coefficient is given by the Chapman-Enskog Equation [106], Equation 22. This treatment of Chapman and Enskog assumes the diffusivity of species i is controlled by binary collisions with gas molecules that are accurately described by the 12-6 Lennard-Jones parameters σ and ε. The collision cross section is given by the average σ of the two molecules, as shown in Equation 23. The collision integral, Ω_D, is looked up in tables of T*, which is solved with Equation 24. The present study used Lennard-Jones parameters and viscosities tabulated by Svehla [107]. The density of combustion gases was assumed to be the density of air (see Appendix A which shows that the gas stream is primarily N_2), tabulated as a function of temperature and pressure in the CRC Handbook [108]. The tables of T* and Ω_D were obtained from Sherwood [109].

$$D_{i,N_2} \approx 0.0018583\sqrt{\frac{1}{M_i}+\frac{1}{M_{N_2}}}\,T^{3/2}\frac{1}{P\sigma_{i,N_2}^2\Omega_D} \qquad (22)$$

Units for Equation 22: D (cm^2/s), M (g/mol), T (K), P (atm), σ (Å), Ω_D ($Å^2$)

$$\sigma_{i,N_2} = \frac{\sigma_i+\sigma_{N_2}}{2} \qquad (23)$$

$$T^* = \sqrt{\varepsilon_i \varepsilon_{N_2}} \qquad (24)$$

The CFBL treatment considered so far only accounts for the rate of transport of deposit species towards the sample surface. This is valid for temperatures far below the dew point of the sulfate where partial pressures of the deposit species are low. As one approaches the dew point, diffusion of the deposit vapor species from the sample surface to the external gas stream must also be considered. The concentration of the gaseous deposit species at the surface, $\omega_{i,w}$, is given by the vapor pressure of the deposit. The FactSage equilibrium module was used to estimate vapor pressures of each deposit species. The concentration at the boundary layer-external gas stream interface, $\omega_{i,e}$, is assumed to be zero as these species rapidly flow downstream. The model for incoming and outgoing Na species is shown schematically in Figure 66. Note that the overall chemical equation written in Figure 66 is only hypothetical. There may be many other reaction pathways (e.g. $2NaOH(g) + SO_2(g) + 1/2O_2(g) \rightarrow Na_2SO_4(g)$) and intermediate reaction steps. Some of the reactants may also be adsorbed on the deposit and/or substrate surface. NaOH(g) does not react to form $Na_2SO_4(g)$ until it diffuses to the surface. This is consistent with the observations of Schofield, Steinberg, and Hynes, who determined that $Na_2SO_4(g)$ fails to form homogenously, requiring a surface [39–41]. This model is approximately steady state assuming that the concentrations of chemical species at both boundary layer interfaces are constant, that there is excess S- and O-containing reactants at the deposit surface, and that surface reaction of NaOH(g) to form $Na_2SO_4(g)$ is fast. It is also assumed that the surface concentration of $Na_2SO_4(g)$ is high enough for the rapid. nucleation of a condensed phase. Analogous transport schemes are assumed for K, Mg, and Ca species.

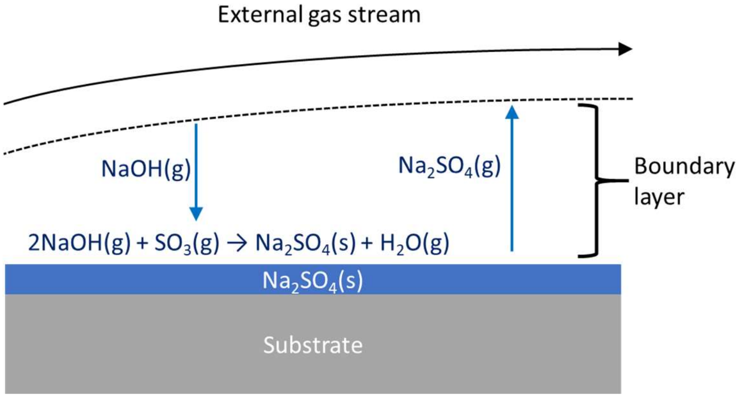

Figure 66. Schematic of boundary layer transport for Na

The formation rate of Na_2SO_4 in the NaCl-injected LVBR at 700 °C was solved by hand to validate each step. More complex calculations, such as deposition of multiple species and/or deposition as a function of temperature, were performed using Python scripts with the Numpy and Scipy libraries. Examples of the hand calculations and Python scripts are shown in Appendix B.

5.5 Methodology - experimental

Each LVBR carousel for runs 1-4 contained sixteen Al_2O_3 pins to act as inert substrates for the collection of salt deposits. Two Al_2O_3 pins were removed from the carousel every 50-100 hours. Two Al_2O_3 pins always remained in the carousel for the 500 h duration of the LVBR exposure. The water-soluble deposits were digested from the pins for ICP analysis according to the procedure described previously. Pins were weighed before and after digestion to measure the area-normalized deposit mass. The time-dependence of these normalized masses provided the rate of water-soluble deposit formation. All seawater cations detected by ICP-OES were assumed to be sulfates as all corresponding oxides were either insoluble or not stable at testing conditions. Each carousel also contained one Pt pin that underwent the same procedure after 500 h exposure for comparison to the Al_2O_3 pins. Plan views of the pins were characterized by SEM/EDS prior to digestion.

Artificial LTHC deposits were created by mixing Na_2SO_4, $MgSO_4$, K_2SO_4, and $CaSO_4$ powders in the experimentally determined proportions. Hot stage XRD was performed on the artificial LTHC deposits using a Malvern-Panalytical Empyrean diffractometer with a Cu source and an Anton Paar HTK1200N oven. XRD patterns were recorded at room temperature, after heating to 300 °C, at 700 °C, and upon cooling to 300 °C. Temperature ramp up and ramp down rates were 100 °C per minute, and temperature was held constant for 5 minutes prior to each scan. Each scan lasted for approximately 5 minutes.

5.6 Results

The equilibrium thermochemical predictions for the LVBR, based on the mass balances in Appendix A, are shown in Table 13. Gas phase products with fugacities < 10^{-6} atm are not shown. There is little difference between the predicted gas phase compositions except for the partial pressure of HCl, which changes with respect to the amount of injected salt solution. The most stable deposit for each seawater compound is the corresponding sulfate (or a double salt sulfate, in the case of $K_2Mg_2(SO_4)_3$). Chloride deposits are not stable under the testing conditions because of the stability of HCl(g). The amount of deposit is roughly 10^{-6} moles deposit per mole of combustion gas for each salt solution composition. Note that solution phases and other line compounds between the different phases are possible, but are not present in the FactPS database. It is assumed that deposit solution phases and compounds may have similar cation ratios as these predicted for pure phase deposits.

Figure 67 shows the FactSage equilibrium dew point predictions. Here "dew point" refers to both the temperature of sublimation of solid compounds and volatilization temperature of liquid deposits. There are also two other relevant transformation temperatures: the decomposition of $MgSO_4$ to MgO and the melting of Na_2SO_4. These two transformation temperatures are shown with dotted curves. At the LVBR's pressure of 1 atm, the predicted dewpoints for Na_2SO_4, K_2SO_4, $CaSO_4$, and MgO are approximately 1000 °C, 800 °C, 1290 °C, and 1460 °C, respectively. The dew point temperatures increase significantly with increasing pressure. At 40 atm, liquid Na_2SO_4 and solid MgO and $CaSO_4$ may be present at temperatures up to 1200 °C. This indicates that hot corrosion may be possible under a wider temperature range in actual turbine conditions.

Table 13. Predicted equilibrium compositions of the LVBR environments

Species	Run 1 (Seawater)	Run 2 (NaCl)	Run 3 ($MgCl_2$)	Run 4 (NaCl & $MgCl_2$)
Gas Phase Fugacity (atm)				
N_2	7.57E-01	7.57E-01	7.57E-01	7.57E-01
O_2	9.56E-02	9.56E-02	9.56E-02	9.56E-02
H_2O	6.35E-02	6.35E-02	6.35E-02	6.35E-02
CO_2	6.15E-02	6.15E-02	6.15E-02	6.15E-02
Ar	9.14E-03	9.14E-03	9.14E-03	9.14E-03
SO_2	7.54E-03	7.54E-03	7.54E-03	7.54E-03
SO_3	5.87E-03	5.87E-03	5.87E-03	5.87E-03
NO	1.73E-05	1.73E-05	1.73E-05	1.73E-05
HCl	2.22E-06	2.80E-06	4.47E-06	3.49E-06
H_2SO_4	2.14E-06	2.14E-06	2.14E-06	2.14E-06
Condensed Phase Mole Fractions				
Na_2SO_4 (s)	8.01E-01	1.00E+00	0.00E+00	3.19E-01
$MgSO_4$ (s)	1.47E-01	0.00E+00	1.00E+00	6.81E-01
$CaSO_4$ (s)	3.49E-02	0.00E+00	0.00E+00	0.00E+00
$K_2Mg_2(SO_4)_3$ (s)	1.69E-02	0.00E+00	0.00E+00	0.00E+00
Moles deposit / system total	1.19E-06	1.20E-06	2.24E-06	1.74E-06

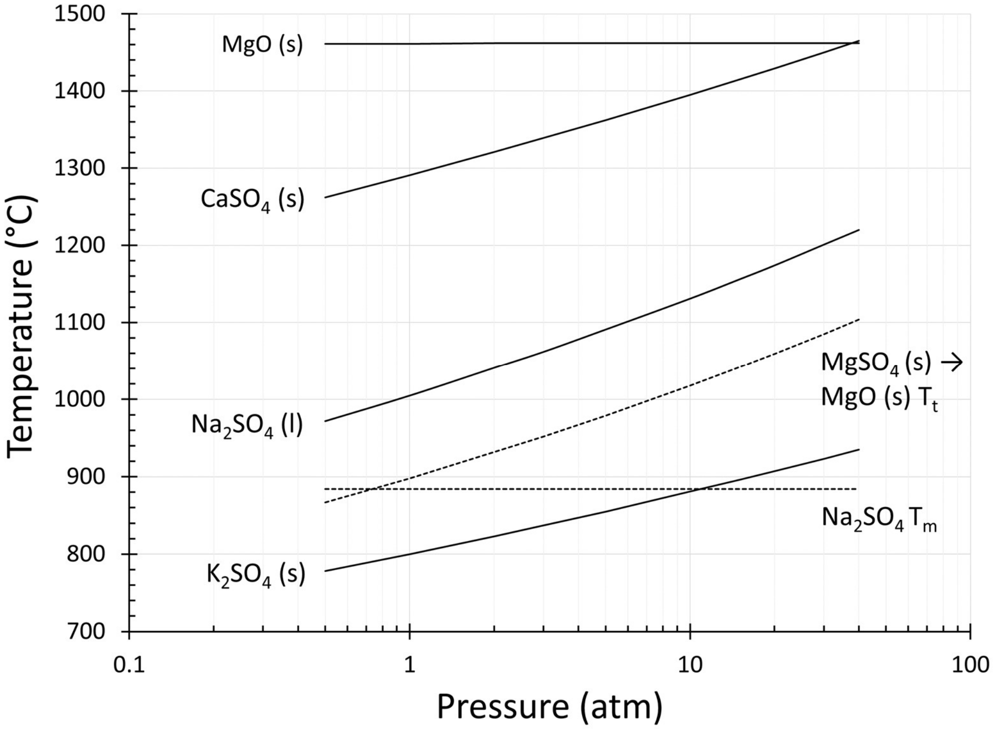

Figure 67. Predicted dewpoints as a function of pressure

The hot stage XRD patterns of the artificial LTHC deposit mixture are shown in Figure 68. The room-temperature Na_2SO_4 V polymorph (an orthorhombic crystal structure with space group Fddd [110]) transforms to the high temperature Na_2SO_4 I polymorph (a hexagonal crystal structure with space group $P6_3/mmc$ [95,110]) at 300 °C. At 700 °C, all cations are in a single solid solution with the hexagonal Na_2SO_4 I crystal structure. Upon cooling back down to 300 °C, an unidentified phase or phases precipitate out of this solid solution. This is likely a double salt or double salts of Na_2SO_4 and the other sulfates as there are multiple poorly-understood double salts in this system [58,73].

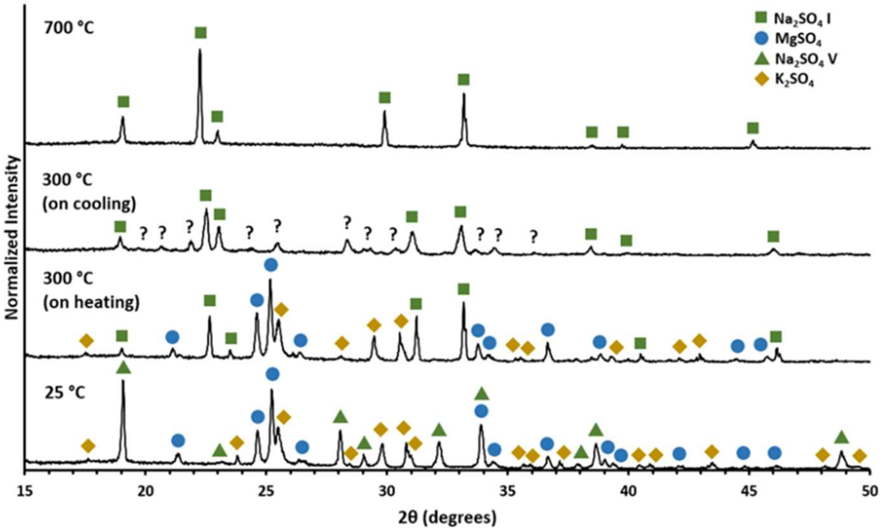

Figure 68. Hot stage XRD patterns for an artificial LTHC deposit with composition (in wt%) 65.1 Na_2SO_4, 27.1 $MgSO_4$, 5.7 $CaSO_4$, and 2.2 K_2SO_4

The area-normalized masses of the water-soluble deposits on Al_2O_3 LVBR pins are shown as a function of time in Figure 69. The salt contaminant with the simplest trend was the NaCl solution, which exhibited a consistent linear time dependence. The deposition rate for the NaCl contaminant is approximately 3.8 x 10^{-3} mg/cm^2·h, resulting in 2 mg/cm^2 of Na_2SO_4 at the end of the 500 h exposure. The seawater contaminant (consisting of primarily NaCl, but also $MgCl_2$ and other salts) exhibited the same trend as NaCl up to 300 h, after which the measured deposit mass plateaued. It is unknown whether this plateau is an intrinsic behavior of the formation of seawater-derived deposits or simply an artifact of imperfectly controlled experimental conditions. Over time, the LVBR flame was observed to grow and shrink. Soot buildup at the fuel injection point was also observed. It is assumed here that the seawater deposit trend prior to 300 h is the more "intrinsic" behavior given its reproducibility in the 100% NaCl exposure. The pure $MgCl_2$ salt solution resulted in negligible water-soluble mass over the entire 500 h exposure period. The 50-50 wt% NaCl-$MgCl_2$ contaminant had a water-soluble deposition rate of less than half that of NaCl and saltwater for the first 200 h of testing. After 200 h, the mass change of water-soluble deposit accelerated to approximately the same rate as NaCl deposition.

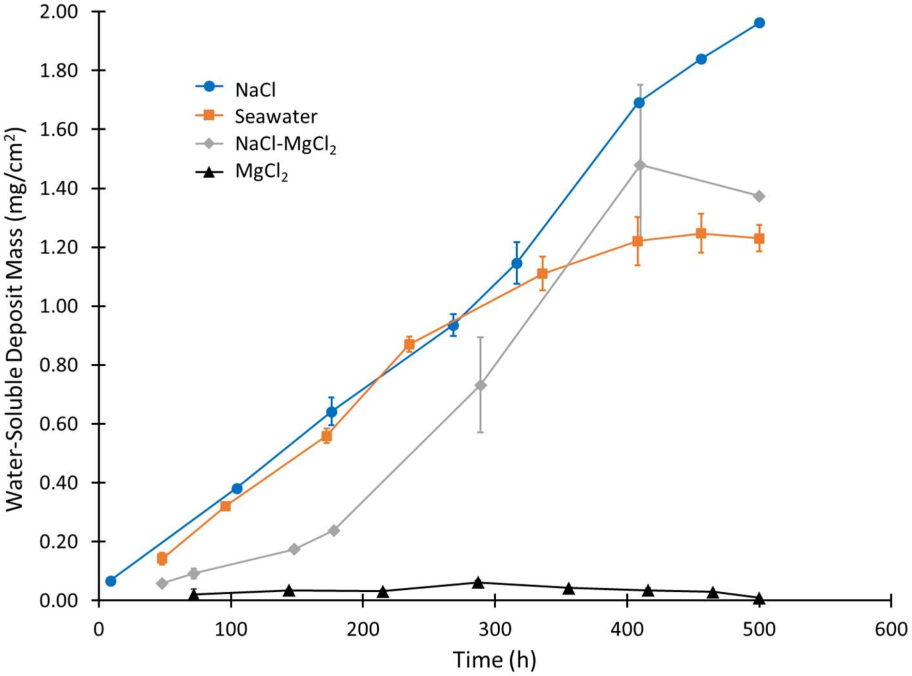

Figure 69. Measured water-soluble deposit masses of intermittently removed Al_2O_3 pins

Figure 70 shows the measured water-soluble Na^+, Mg^{2+}, and S^{2-} on the surfaces of Al_2O_3 LVBR samples with injected $MgCl_2$ and mixed NaCl-$MgCl_2$. No appreciable water-soluble Na^+, Mg^{2+}, and S^{2-} were detected for the pure Mg-salt exposure. The mixed NaCl-$MgCl_2$ exposure shows increasing amounts of Na^+, Mg^{2+}, and S^{2-} with time, consistent with deposits being present as water-soluble sulfates. Water-soluble Mg^{2+} was detected only after 180 h of exposure while water-soluble Na^+ was detected in the earliest measurements. The shapes and trends of the ICP-OES-determined curves are consistent with the measured water-soluble deposit masses of Figure 69.

Figure 71 is an overlay of the NaCl-derived deposition rate and the seawater-derived deposition rate (only including the linear portion prior to 300 h). The fit shows that both closely match a deposition rate of 3.9 x 10^{-3} mg/cm^2·h. This is the deposition rate chosen for comparison to the model predictions.

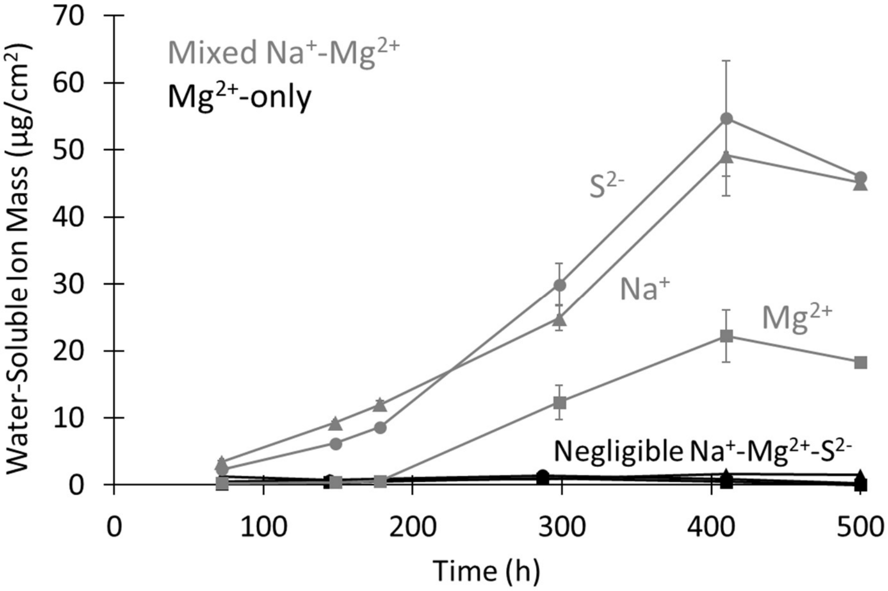

Figure 70. Na$^+$, Mg^{2+}, and S^{2-} measured by ICP-OES for mixed Na$^+$-Mg^{2+} and Mg^{2+}-only exposures in the LVBR at 700 °C (note: S^{2-} measurements likely underestimated due to poor ionization efficiency)

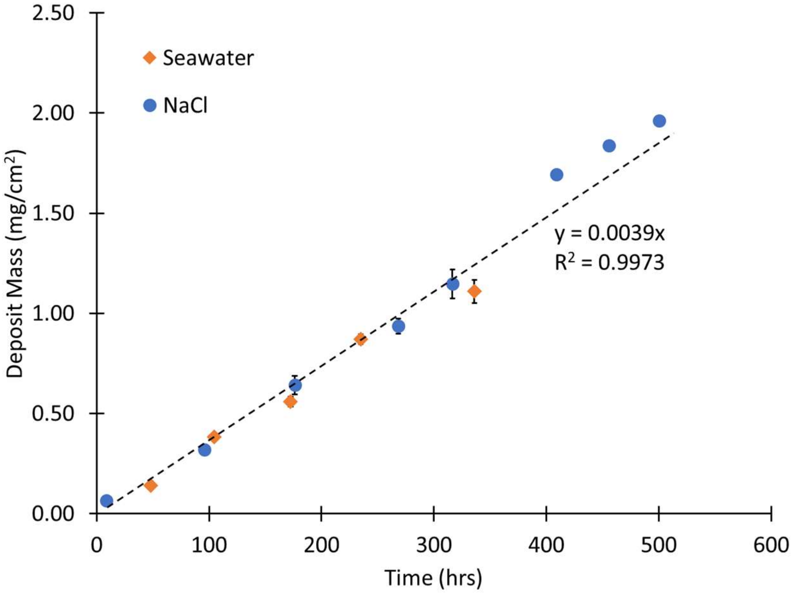

Figure 71. Averaged deposition rates of the NaCl and seawater (linear portion prior to 300 h) both closely fit to a deposition rate of 3.9x10^{-3} mg/cm^2·h. Data is a subset of that in Figure 29 to more clearly show the linear fit

CFBL hand calculations in Appendix B show a predicted deposition rate of 1.24 x 10^{-3} mg/cm^2·h for the LVBR exposure with NaCl solution contaminant. The computed deposition rates for all LVBR runs are shown in Table 14. The total deposition rates are all within a factor of 2 because the number of moles of seawater cations was kept constant and the diffusivities of the hydroxide and oxide vapor species did not vary significantly. The most significant differences between the predicted trends in Table 14 and the measured deposit masses in Figure 69 are the Mg^{2+} exposure and, to a lesser extent, the mixed Na^+-Mg^{2+} run. These differences for the $MgCl_2$ runs indicate that the assumption of $MgSO_4$ over MgO as the depositing species is incorrect.

Table 14. CFBL deposition rate predictions for all LVBR contaminants

	Deposition Rate (mg cm^{-2} h^{-1})				
Contaminant	Total	Na_2SO_4	$MgSO_4$	K_2SO_4	$CaSO_4$
Artificial ocean water	1.45E-03	1.23E-03	1.62E-04	2.06E-05	3.39E-05
NaCl	1.07E-03	1.07E-03	-	-	-
$MgCl_2$	1.68E-03	-	1.68E-03	-	-
NaCl-$MgCl_2$	1.38E-03	4.91E-04	8.90E-04	-	-

The calculated results for artificial ocean water are plotted in Figure 72 as a function of temperature. The primary deposit compound for the artificial ocean water exposure is Na_2SO_4 up to roughly 1040 °C, which is the Na_2SO_4 dew point predicted by the CFBL model at one atmosphere. Above this temperature, the deposit is expected to be rich in $MgSO_4$ and, to a lesser extent, $CaSO_4$. K_2SO_4 behaves similarly to Na_2SO_4 and exhibits a similar relatively low dew point at 800 °C. The total calculated deposition rate at 700 °C is 1.45 x 10^{-3} mg/cm^2·h, with Na_2SO_4 comprising about 85% of the deposit mass. The CFBL model predictions reasonably agree with both experimentally determined deposition rate of 3.9 x 10^{-3} mg/cm^2·h and the equilibrium dewpoints shown in Figure 67. Given that numerous assumptions were made, including that of constant 700 °C combustion gas temperature from flame to sample, inferred (not measured) gas flow rate, and substitutions of Lennard-Jones parameters and viscosity values for compounds lacking available data, it may be concluded that the model is in reasonable agreement with experiment. Another significant source of error may be the 60 rpm rotation of the sample carousel, which was not considered in the CFBL model. This may increase the convective contribution to mass transport, explaining why the model underestimates the deposition rate.

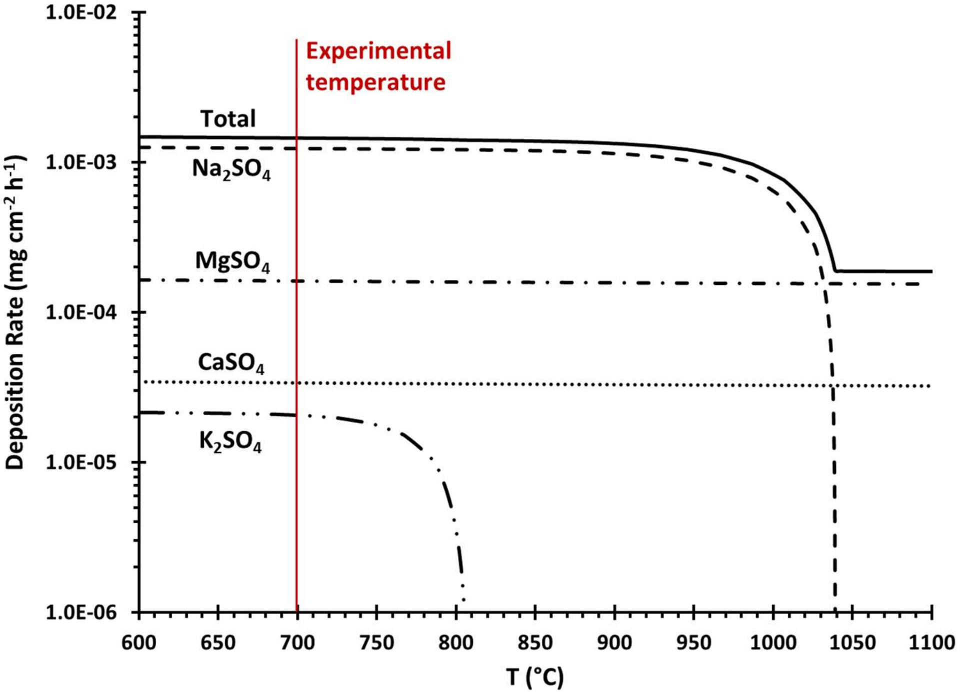

Figure 72. CFBL artificial ocean water model prediction for the LVBR

The Reynolds number for flow of NaOH(g) around the cylindrical pins is approximately 290 (see Appendix B: CFBL Model Example Calculations), indicating laminar boundary layer flow and possible boundary layer separation at the trailing side of the pins [111]. This raises the possibility of unequal deposition rates for the leading and trailing sides of the pins, but microscopy of the pin samples shows similar deposit amounts on both inward- and outward-facing sides. The carousel rotation likely results in more even deposition around the circumference of the samples than if the pins were stationary.

Figure 73 shows SEM images of the Pt pin surface after 500 h exposure in the LVBR at 700 °C. The left image is the exposure with NaCl contaminant, and the right image is that obtained with $MgCl_2$ contaminant. The NaCl-derived deposits fully cover the Pt surface, and EDS clearly shows they are sodium sulfate. Note the morphology of step ledges, hexagonal nuclei, and angles of 120°, which are suggestive of the step-ledge nucleation and growth as well as a hexagonal structure consistent with the Na_2SO_4 I polymorph. The variation in the surface topography suggests a deposit thickness of several μm to tens of μm. In contrast, the $MgCl_2$-derived deposits consist of discrete particles that partially cover the surface. They do not show signs of a step-ledge nucleation and growth mechanism. They are more suggestive of particles that formed upstream and then impacted the sample. EDS suggests they are primarily Mg and O, with no detectable S signal. The dark surface is due to a thin (submicron) Na_2SO_4 layer covering the Pt. This may have originated from Na remaining in the LVBR from previous experiments or from residual Na_2SO_4 from previous exposures that was not fully removed in the water wash. These deposit differences between NaCl and $MgCl_2$ exposures were also observed on Al_2O_3 and alloy samples.

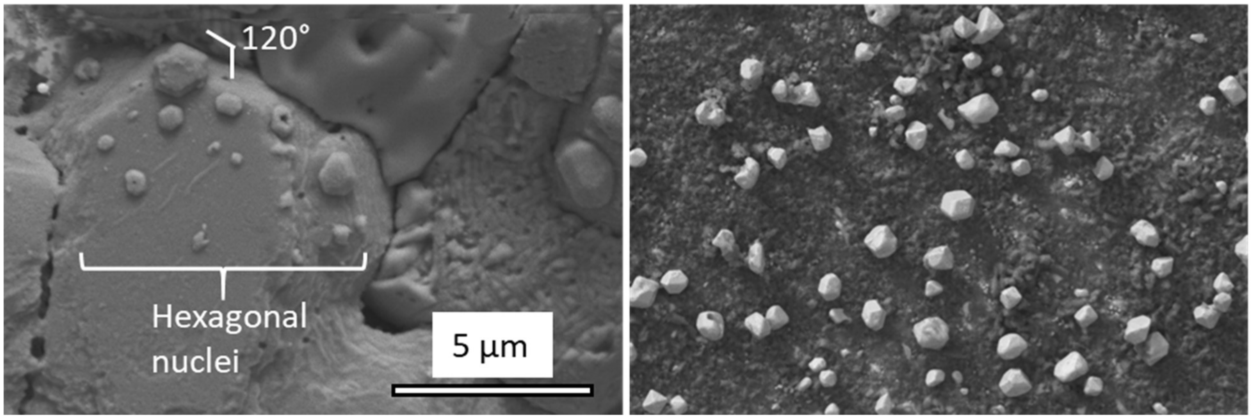

Figure 73. Mixed secondary electron-backsattered electron SEM images show deposits on a Pt pin surface after 500 h LVBR exposure at 700 °C. Left shows deposits derived from NaCl solution injection and right shows deposits from $MgCl_2$ contaminant.

Figure 74 shows deposits on the surface of an Alloy 2 sample after removal from the LVBR NaCl-$MgCl_2$ exposure. EDS point and map data suggest that the large, smooth grains are Na_2SO_4 and that the submicron particles are rich in Mg and O, but poor in S. This is consistent with Mg deposition as particulate MgO. In other locations, the Mg-rich particles appear to react with and become less distinct from the Na_2SO_4 surface.

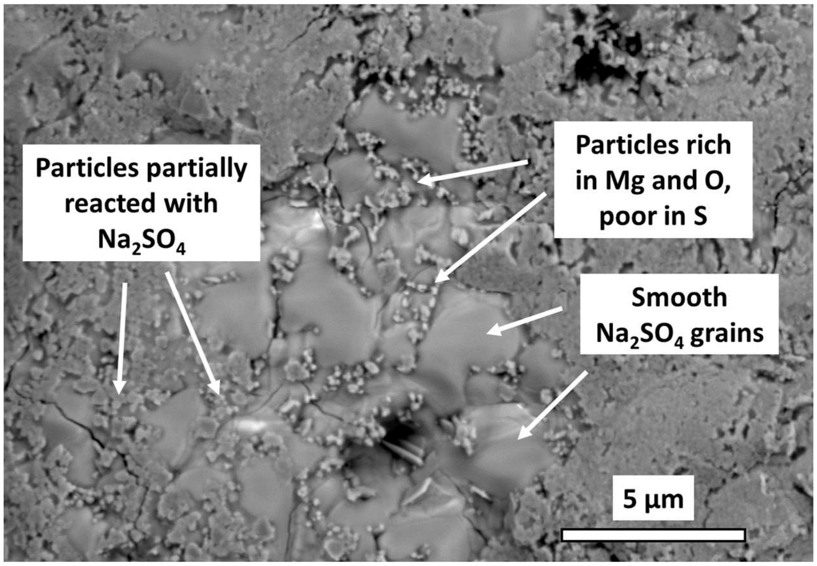

Figure 74. Mg-rich particles in various stages of reaction with Na_2SO_4 on the surface of Alloy 2 after 265 h exposure in the LVBR at 700 °C to the mixed NaCl-$MgCl_2$ salt contaminant

5.7 Discussion

The stark differences between the Na-containing and Mg-containing deposits provide indications of the deposition mechanisms involved in the LVBR. Mg-containing deposits grew primarily through the accumulation of discrete, submicron particles over time. The Na-containing deposits appeared to form via nucleation and growth of Na_2SO_4 on the sample surface. Step ledges and facets in Figure 73 suggest step-ledge growth from vapor phase species. For Na deposits, these observations are consistent with the CFBL assumption that the deposition mechanism is vapor deposition of precursors such as NaOH, which forms Na_2SO_4 via reaction with SO_x and O_2 at the sample surface [99–103]. This suggests that surfaces are vital for Na_2SO_4 formation in these environments and that homogeneous formation of Na_2SO_4 in the gas phase is kinetically limited, consistent with the observations of Schofield, Steinberg, and Hynes [39–41]. Inspection of Equations 6 and 7 show this is unsurprising because, as written, they would involve either ternary/quaternary collisions of gas molecules (SO_2, O_2, H_2O and NaCl or SO_3, H_2O, and NaCl) or multistep processes involving sequences of multiple collisions. This is especially important given the short residence times of gas in a gas turbine [39–41]. Note that while it is reasonable to conclude that the primary deposition mechanism in the LVBR and other similar burner rigs is vapor deposition, other mechanisms may be involved in actual gas turbines. This issue will be discussed later in this section.

The hexagonal faceted microstructure of the Na_2SO_4 deposits in Figure 73 is suggestive of the high temperature hexagonal polymorph. Unfortunately, this could not be confirmed with XRD due to the unfavorable cylindrical pin geometry and small quantity of deposit. This high temperature polymorph may be retained at room temperature by quenching [95,112], and the rapid removal from the LVBR to lab air may have effectively air quenched the deposits. If it is indeed the hexagonal polymorph, the microstructure suggests that growth occurs in a manner to maximize relatively low energy basal plan surface area and minimize high energy prismatic plane area. It also indicates that nucleation of new Na_2SO_4 may occur either on a metal/oxide surface or on the surfaces and step ledges of prior Na_2SO_4 grains.

Anhydrous Na_2SO_4 is commonly encountered as two of its several known polymorphs. These are the high temperature hexagonal Na_2SO_4 I polymorph and the room-temperature orthorhombic Na_2SO_4 V polymorph, commonly known as thenardite [113]. The hexagonal Na_2SO_4 I polymorph exhibits a high solubility for many other sulfates. K_2SO_4 has an identical crystal structure at 700 °C and the Na_2SO_4- K_2SO_4 system is completely miscible at this temperature [58,73]. Na_2SO_4 I may also incorporate up to approximately 35 mol% $MgSO_4$ and/or 35 mol% $CaSO_4$ at 700 °C. This means that quaternary seawater-derived deposits can be in a single phase hexagonal solid solution, as shown in Figure 68. Sulfates of alloying elements are also readily dissolved. At 700 °C, Na_2SO_4 I may incorporate up to 20 mol% $NiSO_4$ or $Y_2(SO_4)_3$ [95]. The incorporation of higher-valence metal sulfate cations is made possible by the formation of Na^+ vacancies to maintain charge neutrality [95,112,114], as shown in Equations 25 and 26 in Kroger-Vink notation for M^{2+} and M^{3+}, respectively. This increase in the concentration of charge carriers is accompanied by an increase in ionic transport through the deposit. Höfer and Eysel predicted a conductivity of nearly 0.1 $(\Omega \cdot cm)^{-1}$ for Na_2SO_4 I with 7 mol% cation vacancies, making doped Na_2SO_4 I deposits relatively fast ion conductors [114]. It is reasonable to say that this allows for rapid interdiffusion of Na_2SO_4 I and other sulfates. This allows for rapid mixing of mixed-cation sulfates, as Figure 68 demonstrates by the formation of a single-phase solid solution within only 5 min at 700 °C.

$$\mathrm{MSO_4} \xleftrightarrow{\mathrm{Na_2SO_4}} \mathrm{M}_{\mathrm{Na}}^{\cdot} + \mathrm{V}_{\mathrm{Na}}' + \mathrm{SO}_{4_{\mathrm{SO_4}}}^{\mathrm{x}} \tag{25}$$

$$\mathrm{M_2(SO_4)_3} \xleftrightarrow{\mathrm{3Na_2SO_4}} 2\mathrm{M}_{\mathrm{Na}}^{\cdot\cdot} + 4\mathrm{V}_{\mathrm{Na}}' + 3\mathrm{SO}_{4_{\mathrm{SO_4}}}^{\mathrm{x}} \tag{26}$$

The delayed deposit mass increase for the NaCl-$MgCl_2$ exposures compared to pure NaCl can be explained by Figure 70. Figure 70 shows that water-soluble Mg^{2+} is not detected until after 180 h of exposure. Two possibilities are either Mg^{2+} is present prior to hour 180, just not in a water-soluble form (i.e. as MgO) or that it does not deposit until 180 h of exposure in the LVBR. The pure $MgCl_2$ exposures show that Mg^{2+} in the absence of Na_2SO_4 deposits as MgO, as in Figure 73, supporting the proposal that the Mg^{2+} exists as water-insoluble MgO prior to sulfation observed after 180 h. Figure 74 appears to show Mg-rich particles in different stages of reaction with Na_2SO_4. EDS shows that these Mg particles are poor in S, but some particles are distinctly separate from the Na_2SO_4 grains while others appear to have partially reacted and to have interdiffused with the sulfate. This is partly explained by the relatively low driving force for sulfation of MgO, as shown in Figure 17. In the absence of Na_2SO_4, no sulfation of MgO was detected even after 500 h of exposure. However, the sulfation of MgO is accelerated in the presence of Na_2SO_4, as inferred by the water-solubilities of Mg^{2+} in Figure 70.

Jones, Nordman, and Gadomski observed a similar effect for Y_2O_3 with and without Na_2SO_4. Y_2O_3 formed $Y_2(SO_4)_3$ in the presence of a Na_2SO_4 deposit. In the absence of such a deposit, Y_2O_3 exhibited incomplete sulfation and they detected $Y_2O_2SO_4$ [94]. This is despite a constant gas stream of SO_3. LTHC has been observed in Pt-catalyzed atmospheres containing only 2.5 ppm SO_2 in O_2

as long as a Na_2SO_4 deposit is present [52,75]. This S concentration is significantly below that required for stabilizing pure $NiSO_4$ or $CoSO_4$ [38,67]. Misra, Whittle, and Worrell explained this enhanced sulfation of oxides in the presence of Na_2SO_4 (in the context of the enhanced sulfation of NiO and CoO in NiO-Na_2SO_4 and CoO-Na_2SO_4 systems) on the grounds that the pSO_3 required for the formation of a MSO_4-Na_2SO_4 melt (where M is Ni or Co), is less than that required for forming pure solid MSO_4 [115]. This thermodynamic explanation also implies the kinetics of sulfation of MgO, NiO, and other oxides may be enhanced due to the larger driving forces for the mixed-sulfate liquid. Note that this enhanced sulfation could be applicable to MgO, CaO, and other CMAS-like oxide particles observed on marine turbine blades. The effect would be a mixed sulfate, increasing the likelihood of eutectic melts and thus hot corrosion.

The observations of enhanced sulfation in the presence of Na_2SO_4 led Misra, Whittle, and Worrell to conclude "Clearly, the formation of the liquid sulfate also depends on the relative proportions of CoO (or NiO) and Na_2SO_4… Thus an important factor may well be the rate of formation of the CoO (or NiO) relative to the rate of Na_2SO_4 deposition…" [115]. This illustrates the need for the present analysis on the deposition process in addition to metallurgical considerations such as alloy content and phase fractions. The salt deposition rate as well as the formation of NiO and CoO determine whether the conditions for melting and subsequent LTHC are met.

It is important to note that the LVBR deposition mechanisms may differ from those in gas turbines. The continuous distribution of Na_2SO_4 on samples exposed in the LVBR (Figure 73) differs significantly from the discontinuous distribution of circular deposits observed on the marine gas turbine blades (Figure 13). It is possible that deposition of Na_2SO_4 may occur via impaction of Na-containing salt particles on turbine blade surfaces rather than through a boundary-layer-controlled vapor deposition mechanism. Multiple mechanisms may be possible, especially given the dynamic environment of a gas turbine. Hanby [42] suggests that deposition may occur due to large NaCl particles breaking off from upstream compressor blades, implying that particles of sufficient size would react to form Na_2SO_4 before all Na is lost as gaseous NaCl. Further characterization of gas turbine deposits, modeling of vapor deposition and impaction, and more deposition experiments performed under a wider range of environments are needed to relate the burner rig deposition mechanisms of the present study to deposition mechanisms of gas turbines.

5.8 Conclusions

Deposition of Na_2SO_4 in the LVBR is consistent with a vapor deposition mechanism with the rate-limiting step being diffusion of precursor species across the boundary layer. Na_2SO_4 formed continuous deposit layers while Mg species tended to deposit as discrete MgO particles. These particles likely reacted in the presence of Na_2SO_4 to form $MgSO_4$, although the kinetics were sluggish. MgO failed to sulfate within 500 h in the absence of Na_2SO_4. The results suggest that Na_2SO_4 promotes the sulfation of oxides such as MgO, NiO, and CoO, which have less stable sulfates. Previous work by Misra, Whittle, and Worrell suggests this is because the pSO_3 required to form a liquid Na_2SO_4-MSO_4 mixture (where M is Ni, Co, Mg) is less than that required to form the pure MSO_4 solid. This analysis highlights the importance of the deposition rate/amount of Na_2SO_4 on sulfation of other oxides, melting, and subsequent hot corrosion. It also raises the possibility that Na_2SO_4 could increase the sulfation kinetics of MgO and CaO in the CMAS-like deposits observed on turbine blades. The morphology of LVBR deposits was significantly different from that of deposits from marine gas turbine blades. This suggests that different deposition mechanisms, particularly impaction of particles, may dominate in field hardware compared to burner rig or other lab testing.

6.0 Corrosion of YSZ coatings and NiCoCrAlY alloys by CMAS-sea salt mixtures

6.1 Objectives

Hot corrosion of field hardware may involve complex deposit mixtures containing sulfates, CMAS, and even NaCl, as seen by the previous characterization of marine turbine blades. Gas turbines may use ceramic thermal barrier coatings (TBCs) on Ni-base alloys. The interaction of these complex deposits with both metallic and ceramic substrates is therefore relevant. The space of possible deposit compositions and engineering materials becomes very large, necessitating machine learning models to predict corrosion mode and extent. In this objective, data from the literature were collected and experiments were performed to generate training sets for the machine learning performed by Mukil Ayasammy and Dr. Prasanna Balachandran, both from UVA. The emphasis here will be on the preliminary experimental findings, particularly on the various qualitative corrosion modes that were observed to provide descriptors for machine learning. The experimental findings answer the research question "How might previous models and understanding be extended to predict corrosion with even more complex deposits and material systems?"

The mechanisms of CMAS attack of Yttria-Stabilized Zirconia (YSZ) Thermal Barrier Coatings (TBCs) in the absence of sea salt and sulfates are relatively well-understood. CMAS deposits form from ingested sand, dust, volcanic ash, or other siliceous debris and typically melt at temperatures ≥ 1150 °C [45,48,116]. The melt infiltrates pores and cracks in the coating, where it dissolves Y_2O_3 from YSZ [117,118]. The loss of Y_2O_3-stabilization and the filling of pores leads to cracking and delamination of the TBC [117–121] as well as an increase in thermal conductivity [122]. However, characterization of marine gas turbine blades reveals that deposits may often be CMAS-sulfate-sea salt mixtures [37,51,98]. There are relatively few published studies of the corrosion of TBCs by these complex CMAS mixtures other than characterization of field hardware degraded by CMAS-$CaSO_4$ mixtures by Braue [46,47,123]. A combination of machine learning and experimental methods are used in the present study to begin to fill in these knowledge gaps.

Preliminary results for the complex multicomponent deposits and coating/alloy systems are presented to extend research into more complex systems. The previous investigations into the effects of Mg salts, Cr and Y alloying additions, and deposition processes are all quantitative, probing fundamental aspects of corrosion mechanisms. The following CMAS-sea salt mixture study is a natural extension of the previous research, albeit more qualitative, but directed toward machine learning predictions and of engineering importance.

6.2 As-received materials

Yttria-Stabilized Zirconia (YSZ) is a common TBC used to protect Ni- and Co-base alloys in gas turbines. Air Plasma-Sprayed (APS) YSZ-alloy coating systems were provided by Dr. Rob Golden of Rolls-Royce Corporation. The as-received microstructure is shown in Figure 75. The system consists of a C263 alloy substrate consisting of a γ solid solution (nominal composition Bal. Ni/20 Co/20 Cr/6 Mo/2 Ti/0.5 Al), a NiCoCrAl bond coat, and a YSZ topcoat. The composition of the NiCoCrAl bond coat is Bal Co/33 Ni/21 Cr/7 Al as determined by EDS. The bond coat also contains Al_2O_3 (dark phase), which is a result of the thermal spraying process. The YSZ coating has a composition of approximately 5 wt% Y_2O_3 in ZrO_2 as determined by EDS. ImageJ analysis

[81,82] shows an average thickness of 250 µm and an average porosity of 17 vol% (assuming the cross-sectional porosity area is equivalent to porosity volume).

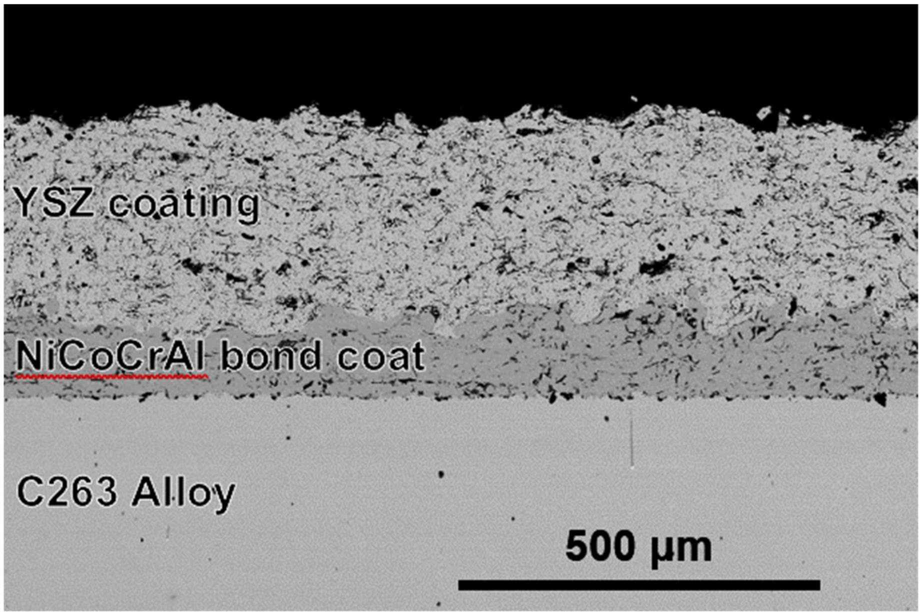

Figure 75. As-received YSZ-coated alloy

In addition to the YSZ-coated C263, standalone NiCoCrAlY Alloy 2, used in the previous section "4.0 Burner rig and furnace LTHC exposures," was exposed to complex deposits for comparison. To reiterate, it has a composition of Bal Ni/26 Co/16 Cr/14 Al/0.1 Y and consists of γ and β solid solutions with occasional yttride precipitates.

6.3 Methodology

The present study consists of a literature data review, estimation of deposit melting points using Thermo-Calc [83] and FactSage [38], and furnace exposures of the ceramic and metallic materials to CMAS/salt deposit mixtures.

6.3.1 Literature review

Data from the literature on mixed CMAS-sulfate-NaCl deposit-induced corrosion were compiled from twelve sources [23,36,70,122,124–131] to create the dataset for machine learning. Six sources were on the corrosion of metallic materials and six others on TBC corrosion. Each unique material-environment high temperature exposure constituted one "data point," which contains descriptors such as composition and porosity as well as environmental/experimental parameters such as temperature, time, and thermal cycling rate. The goal of machine learning is to model the relationship between the extent of corrosion and identified descriptors. The machine learning method used in the present work is called the Support Vector Machine (SVM). SVM is a popular method known for its robustness, especially when it comes to small datasets [132]. The SVM function was used with the non-linear radial basis function kernel from the e1071 package in R. A non-parametric bootstrap method was employed to build an ensemble of SVM models. Building an ensemble of models as opposed to a single model has two advantages: first, the bias-variance tradeoff problem in machine learning can be addressed and secondly, prediction uncertainties (error bars) can be quantified. The model trained on the dataset described above was used to predict the extent of corrosion along with the error bars for new data points. The extent of corrosion was quantified by mass gain and molten deposit penetration depth for metals and ceramics, respectively. An example of model predictions will be shown, but analysis will focus on the experimental results of alloys and ceramic coatings in mixed CMAS-$CaSO_4$-NaCl for identification of descriptors appropriate for machine learning.

6.3.2 Deposit melting point estimation

Significant CMAS attack occurs if the deposit is molten, and melting point correlates to viscosity and thus also the rate at which the molten glass penetrates pores and cracks in the substrate [48,133]. Therefore, deposit melting point is a critical parameter to use in the machine learning model. Deposit compositions not experimentally determined in the literature were calculated using FactSage 8.0 [38], with the Equilibrium module with the FactPS, FToxid, and FTsalt databases, and Thermo-Calc 2020a [83], with the SSUB6 and TCOX9 databases. The CMAS compositions and melting points used for the model are shown in Table 15. "Melting point" is defined here as the minimum temperature at which any amount of liquid is predicted or observed. In general, there was good agreement between experimental melting point determinations and FactSage and Thermo-Calc estimates.

Table 15. Melting temperatures of CMAS-$CaSO_4$ compositions (wt%). FactSage and Thermo-Calc values are theoretical while the "from paper" values are experimentally determined

Source	SiO_2	CaO	$CaSO_4$	MgO	Al_2O_3	Fe_2O_3	FeO	TiO_2	Na_2O	K_2O	Melting T (°C) (FactSage)	Melting T (°C) (Thermo-Calc)	Melting T (°C) (from paper)
Boissonnett 2019	51.9	33.1	0.0	4.0	8.4	2.6	0.0	0.0	0.0	0.0	1135	1159	-
Fang 2019	53.4	31.6	0.0	3.0	6.1	3.5	0.0	0.0	0.9	1.5	916	-	-
Naraparaju 2014	40.0	22.0	0.0	8.0	18.0	0.0	10.0	2.0	0.0	0.0	1032**	-	1200
Naraparaju 2014	32.0	17.6	20.0	6.4	14.4	0.0	8.0	1.6	0.0	0.0	1167	-	1185
Xia 2016	51.8	8.7	0.0	3.9	12.7	18.4	0.0	1.8	0.4	2.3	-	-	1063
Yin 2019*	48.4	33.2	0.0	6.5	11.9	0.0	0.0	0.0	0.0	0.0	1208	1205	1197
Rivera-Gil 2019	75.3	2.8	0.0	0.1	3.3	8.9	0.0	1.6	7.7	0.3	-	-	1035
Rivera-Gil 2019	70.0	4.7	0.0	0.2	6.6	9.9	0.0	1.0	7.4	0.2	-	-	1060
Rivera-Gil 2019	46.4	8.6	0.0	1.7	7.6	26.2	0.0	5.6	3.7	0.2	-	-	1160
UVA - 0 wt% $CaSO_4$*	48.4	33.2	0.0	6.5	11.9	0.0	0.0	0.0	0.0	0.0	1208	1205	-
UVA - 25 wt% $CaSO_4$	36.3	24.9	25.0	4.9	8.9	0.0	0.0	0.0	0.0	0.0	-	1113	-

* UCSB composition

** This FactSage prediction is dubious - experimental result should be used

6.3.4 Furnace exposures

The CMAS composition used for the experiments in the present study was the UCSB Composition, which is 48.4 SiO_2/33.2 CaO/6.5 MgO/11.9 Al_2O_3 in wt% [117]. Additions of $CaSO_4$ and NaCl were used to understand the effects of these constituents on CMAS corrosion. Thermo-Calc calculations of the UCSB CMAS and UCSB CMAS + 25 wt% $CaSO_4$ are shown in Figure 76. The melting point of UCSB CMAS (Figure 76, left) was calculated to be 1205 °C. The addition of 25 wt% $CaSO_4$ results in a melting point reduction of approximately 80 °C. $CaSO_4$ also causes a miscibility gap in the liquid phase at 1250-1300 °C. Lastly, while $CaSO_4$ depresses the initial melting point, some solid deposit phases are predicted to remain up to 1260 °C. The melting point reduction would likely be accompanied by a decrease in viscosity and a resulting increasing in penetration depth of the liquid through cracks and pores in the YSZ coating. The possible effects of two immiscible liquid phases and residual solid phases are less clear.

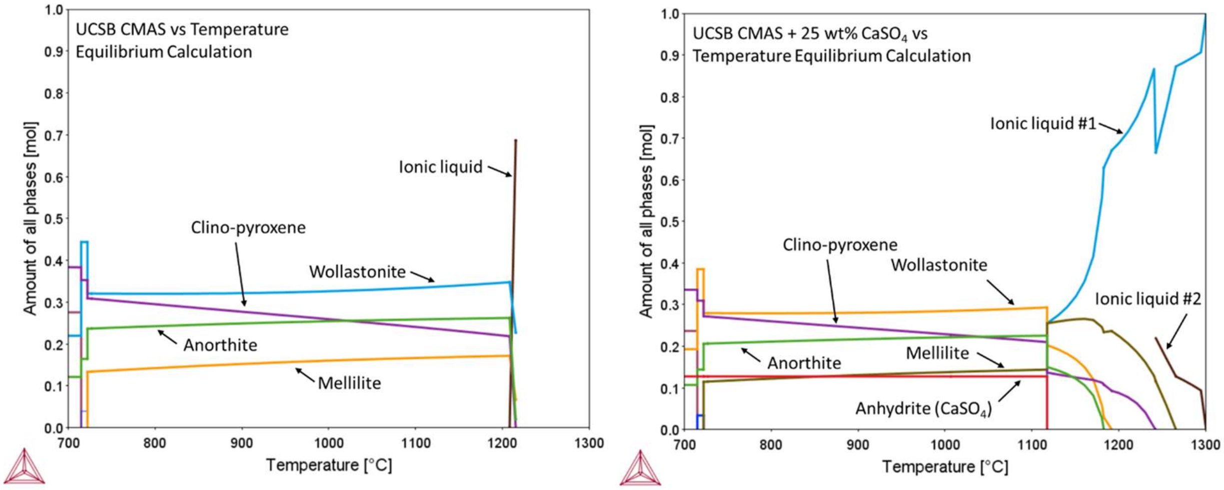

Figure 76. Equilibrium Thermo-Calc calculations for the UCSB CMAS composition with and without 25% wt% $CaSO_4$

Deposits were prepared by mixing powders with compositions listed in Table 16 followed by cold pressing at 10 MPa to create thin pellets. The pellets were placed on the sample surface, as shown in Figure 77. Dry pressed powders were poorly adherent to the Alloy 2 surface, and so the same deposit compositions were mixed with ethanol to obtain a slurry. The slurry was then spread on the alloy surface with a spatula. The masses of deposits for both YSZ and alloy deposits were approximately 20 mg/cm^2. Samples were inserted into a tube furnace preheated to 1250 °C with air flowing at 100 sccm. The temperature was held at 1250 °C for 2 hours and then ramped down to room temperature at 6 °C per minute to reduce coating spallation in the case of YSZ-coated samples. Even with the slow temperature ramp, some coatings spalled or were poorly adhered so that spallation occurred when trying to cross-section samples. XRD was only performed on areas with remaining coating. Spalled coating pieces were recovered and mounted upright for cross-sectional SEM/EDS characterization. Cross sections were mounted in epoxy and polished in nonaqueous media.

Table 16. Deposit compositions used for furnace exposures (note that the 75-25 wt% CMAS-$CaSO_4$ composition was used for a model validation test only)

Deposit Composition (wt%)													
CMAS	$CaSO_4$	NaCl		$CaSO_4$	SiO_2	CaO	MgO	Al_2O_3	NaCl	Na_2O eq		T (°C)	t (h)
100	0	0		0.0	48.5	33.2	6.5	11.9	0.0	0.0		1250	2
75	25	0		25.0	36.3	24.9	4.9	8.9	0.0	0.0		1250	2
50	50	0		50.0	24.2	16.6	3.3	5.9	0.0	0.0		1250	2
0	100	0		100.0	0.0	0.0	0.0	0.0	0.0	0.0		1250	2
90	0	10		0.0	43.6	29.8	5.9	10.7	10.0	5.0		1250	2
0	90	10		0.0	38.8	26.5	5.2	9.5	20.0	9.6		1250	2
45	45	10		45.0	21.8	14.9	2.9	5.3	10.0	5.0		1250	2

Figure 77. Deposit pellet (0.25 in. diameter) on a YSZ sample prior to furnace exposure

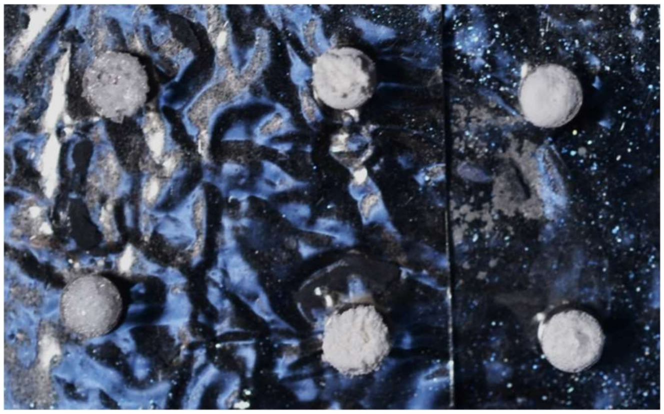

Figure 78. Deposits on Alloy 2 samples (0.125 in. diameter) prior to furnace exposure

6.4 Results

6.4.1 YSZ-coated C263

Post-exposure cross sections for YSZ with 100% CMAS, 50% CMAS-50% $CaSO_4$, and 100% $CaSO_4$ are shown in Figure 79. Higher magnification images are shown in Figure 80. The degradation morphology for the 100% CMAS deposit is consistent with previous studies. Molten CMAS partially dissolved YSZ grains and penetrated pores, cracks, and grain boundaries. This disruption of the material resulted in significant amounts of cracking and void formation. The

100% $CaSO_4$ deposit reacted with the YSZ to form a relatively uniform product layer 50-100 μm thick. Point EDS showed a 1:1 Ca:Zr ratio, consistent with the reaction product being $CaZrO_3$. $CaSO_4$ caused relatively little cracking and reduced void formation compared to CMAS attack. Residual $CaSO_4$ was detected in-between $CaZrO_3$ and YSZ grains, showing that $CaSO_4$ did not completely dissociate into CaO and SO_3 under the testing conditions. The 50% $CaSO_4$-50% CMAS deposit reacted with YSZ to form a less-uniform Ca- and Zr-containing silicate. EDS results indicating a Ca:Zr:Si ratio of 2.8:1:2, consistent with $Ca_3ZrSi_2O_9$, mineral name baghdadite [134]. All deposits, regardless of composition, were detected at the YSZ-bond coat interface, indicating that the coating was fully penetrated in all cases.

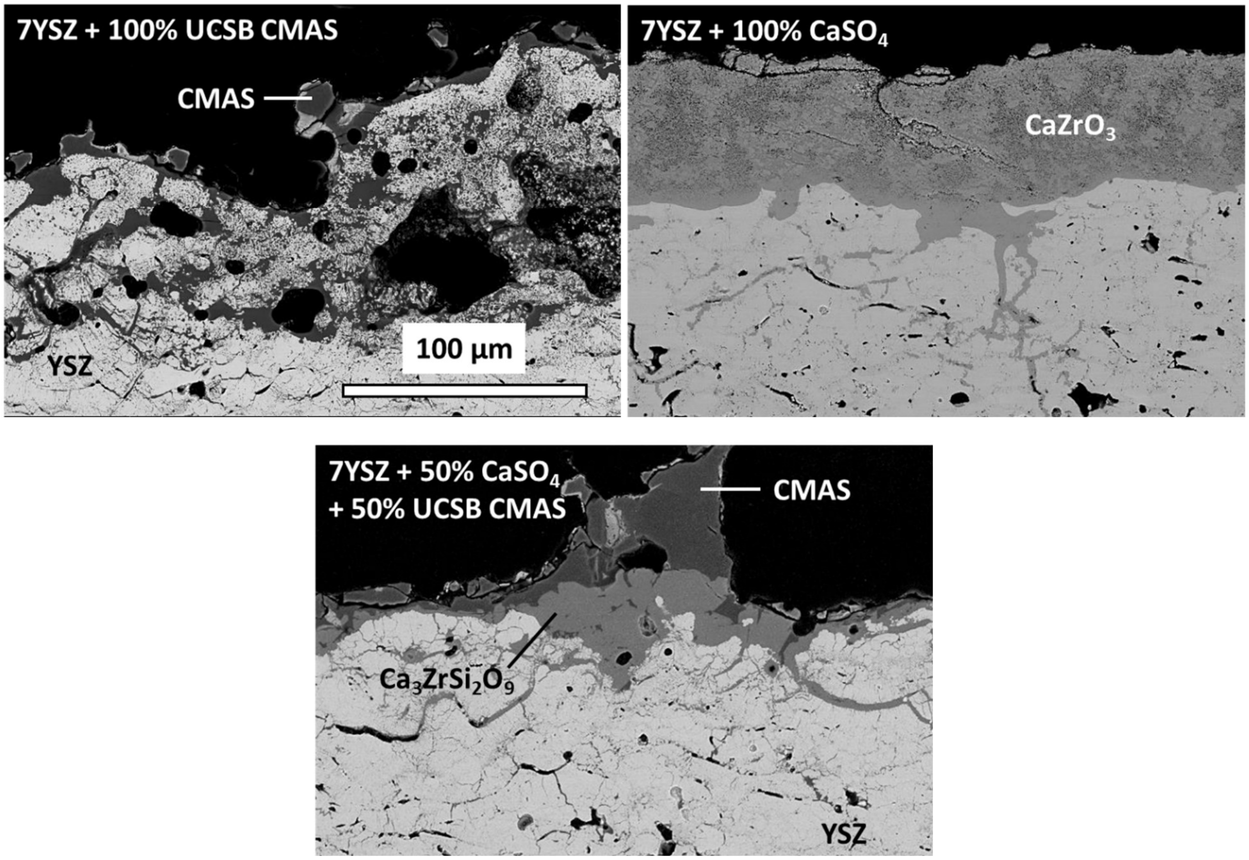

Figure 79. Cross-sectional SEM images of YSZ after 2 h furnace exposure at 1250 °C with 20 mg/cm² deposit. Deposit compositions are specified on each image.

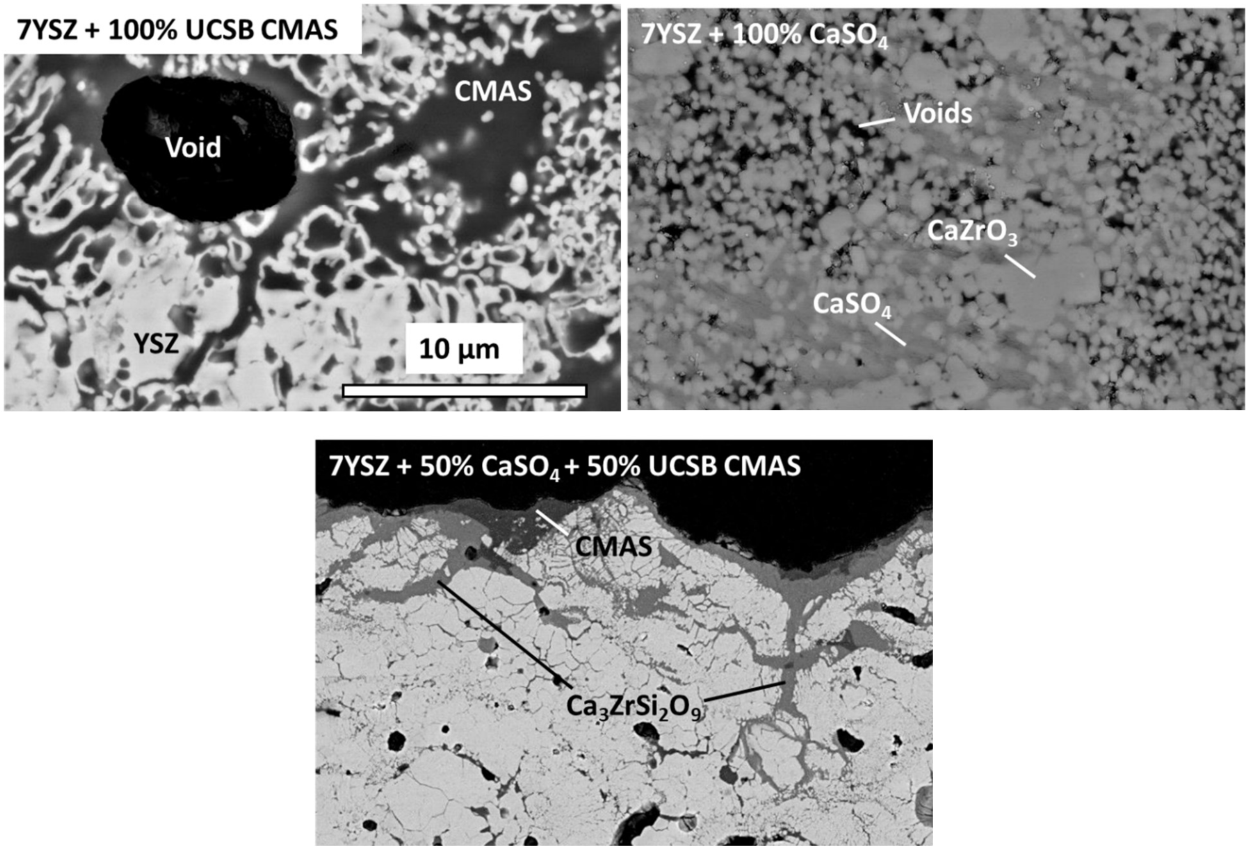

Figure 80. Higher magnification cross-sectional images of YSZ after 2 h furnace exposure at 1250 °C with 20 mg/cm^2 deposit. Deposit compositions are specified on each image.

XRD results of the YSZ surface before and after high temperature exposure to $CaSO_4$ are shown in Figure 81. The $CaZrO_3$ perovskite reaction product was confirmed. Residual $CaSO_4$ was also detected, consistent with SEM/EDS analysis. Diffraction peaks for $CaMoO_4$ were present. Mo, which forms gaseous oxides at 1250 °C [6], originates from the C263 alloy. All alumina boat surfaces and the inside of the quartz tube turned a blue color, consistent with deposition of volatile Mo species. Further SEM and EDS suggest that $CaMoO_4$ is present as a thin layer at the top of the deposit/reaction product. There was no evidence that Mo is present in the molten phases that penetrated the coating.

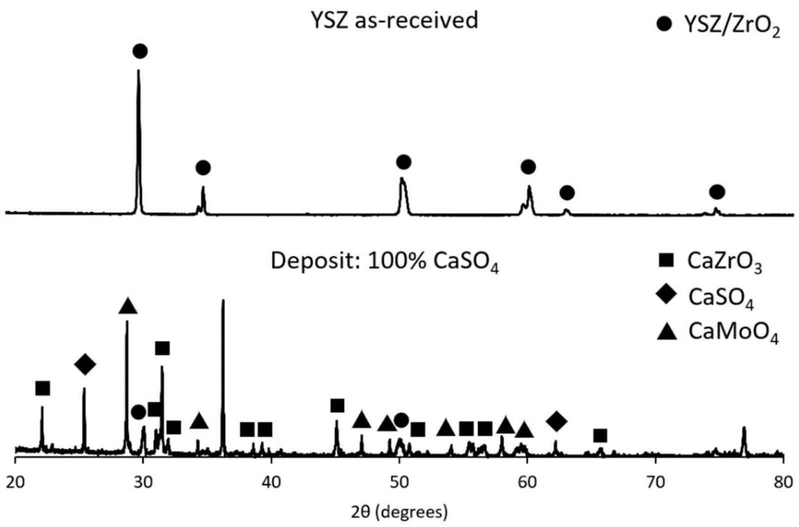

Figure 81. XRD patterns of the YSZ surface before and after 2 h furnace exposure at 1250 °C with 20 mg/cm^2 surface loading of $CaSO_4$

The previous furnace exposures were repeated with all three deposits containing 10% NaCl additions. Figure 82 and Figure 83 show high magnification and low magnification cross-section SEM images, respectively. Qualitatively, there is no significant difference in the reaction morphology. The 90% CMAS-10% NaCl exposure again resulted in similar crack/void formation and partially dissolved YSZ grains depleted in Y_2O_3. The 90% $CaSO_4$-10% NaCl deposit formed a $CaZrO_3$ reaction layer similar to that observed with 100% $CaSO_4$. The 45% CMAS-45% $CaSO_4$-10% NaCl exposure resulted in $Ca_3ZrSi_2O_9$ formation consistent with the 50% CMAS-50% $CaSO_4$ exposure. However, the sample with 45% CMAS-45% $CaSO_4$-10% NaCl retained more of the CMAS deposit, which spalled off during or after the 50% CMAS-50% $CaSO_4$ test. Figure 83 shows cracking within the $Ca_3ZrSi_2O_9$ that may explain the lack of remaining CMAS/$CaSO_4$ in Figure 79 and Figure 80. Two different CMAS phases are visible in Figure 82 for the mixed CMAS-$CaSO_4$ deposit. A plan view image of the same sample in Figure 84 shows the phase contrast more clearly. EDS point analysis suggests that the darker CMAS phase is richer in Mg and Na than the lighter CMAS phase. The observed two phase reaction product is consistent with

Thermo-Calc calculations predicting a miscibility gap for the mixed CMAS-$CaSO_4$ deposit (Figure 76, right).

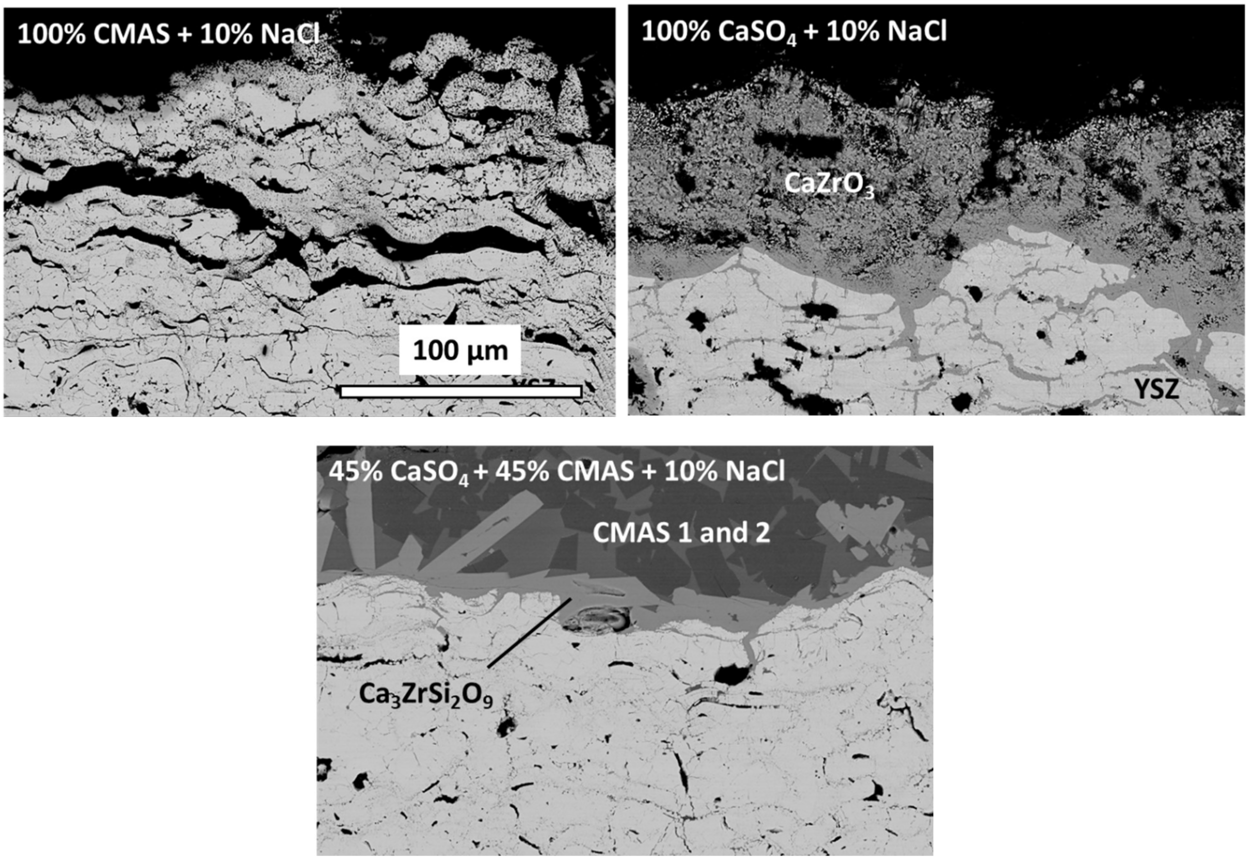

Figure 82. Cross-sectional SEM images of YSZ reaction with NaCl-containing deposits after 2 h furnace exposure at 1250 °C with 20 mg/cm^2 deposit

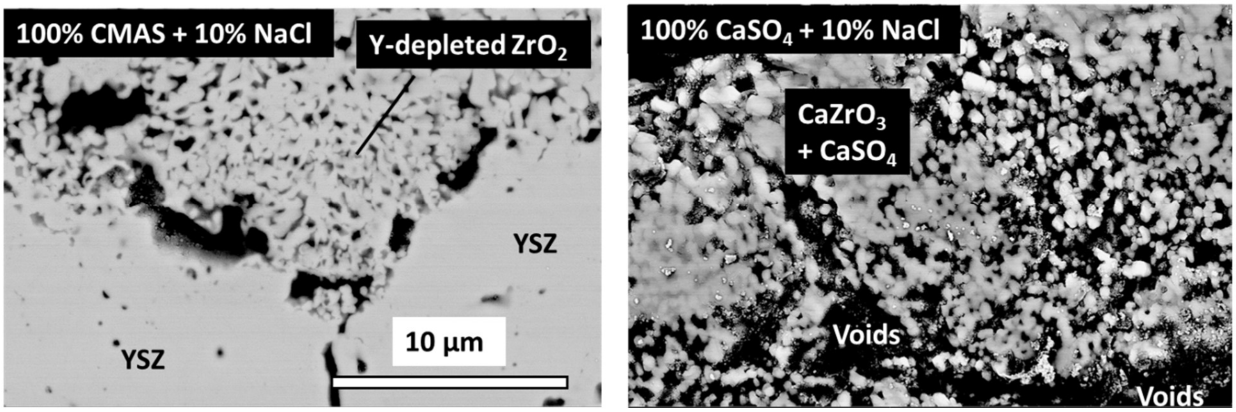

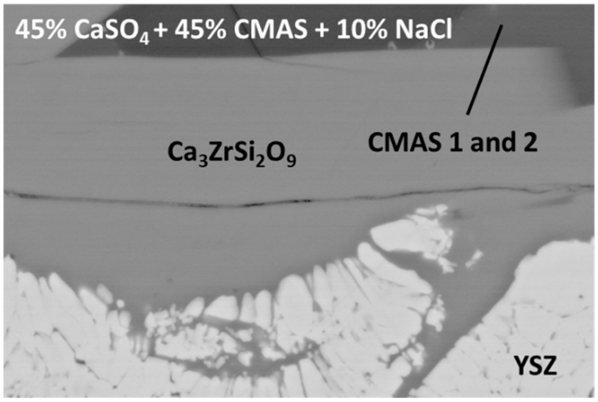

Figure 83. Higher magnification cross-sectional SEM images of YSZ reaction with NaCl-containing deposits after 2 h furnace exposure at 1250 °C with 20 mg/cm^2 deposit

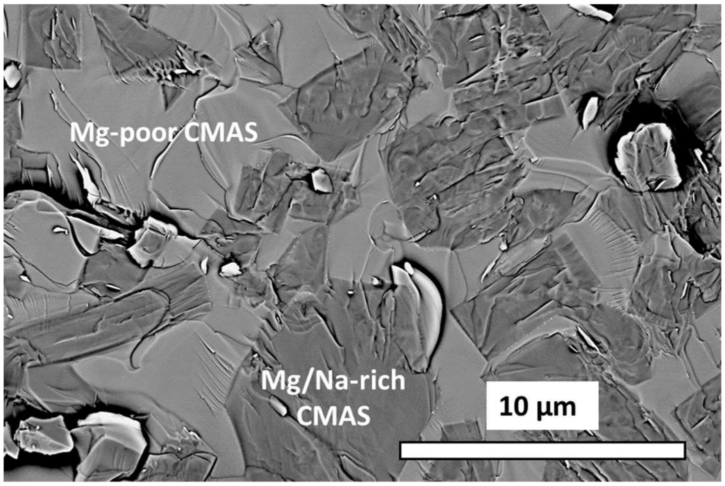

Figure 84. Plan view SEM image of the 45% CMAS-45% $CaSO_4$-10% NaCl deposit after 2 h exposure at 1250 °C clearly showing the presence of two immiscible CMAS phases

The XRD spectra in Figure 85 again show $CaMoO_4$ formation on the top of the reaction layers for all deposit compositions. The $CaZrO_3$ phase is detected for the 90% CMAS-10% NaCl and 45% CMAS-45% $CaSO_4$-10% NaCl exposures. While $Ca_3ZrSi_2O_9$ was the dominant reaction product observed in the 45% CMAS-45% $CaSO_4$-10% NaCl cross-sections, this phase is not detected by XRD. However, Figure 82 shows this phase is formed beneath remaining CMAS layer that is greater than 50 µm thick.

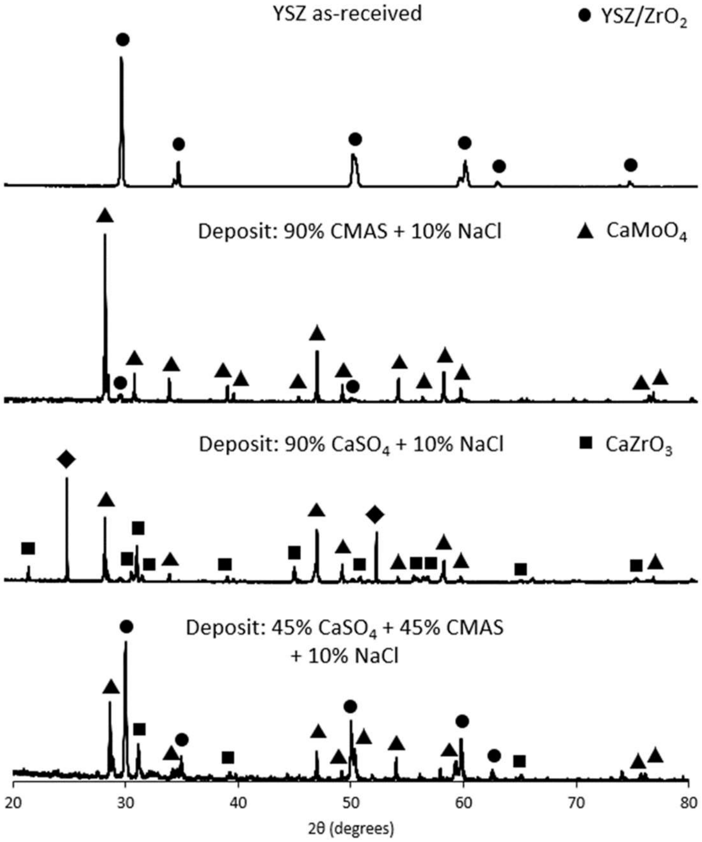

Figure 85. XRD spectra of the surface of YSZ samples exposed to NaCl-containing deposits after 2 h furnace exposure at 1250 °C

The CMAS and $CaSO_4$ exposures resulted in different YSZ coating failure modes, as seen in Figure 86. CMAS attack resulted in cracking within the YSZ coating, while the $CaSO_4$-attacked coating usually delaminated from the bond coat in one single piece and with less intra-coating cracking. Higher magnification SEM images of TBC-bond coat interface for the sample exposed to 100% $CaSO_4$ are shown in Figure 87. The interface is littered with nonprotective oxides containing Ni, Co, and Cr. A Ca-containing phase is also present, which EDS suggests is $CaAl_2O_4$. Cracks bridging the crests of the wavy interface are visible in locations where the TBC still adheres to the bond coat.

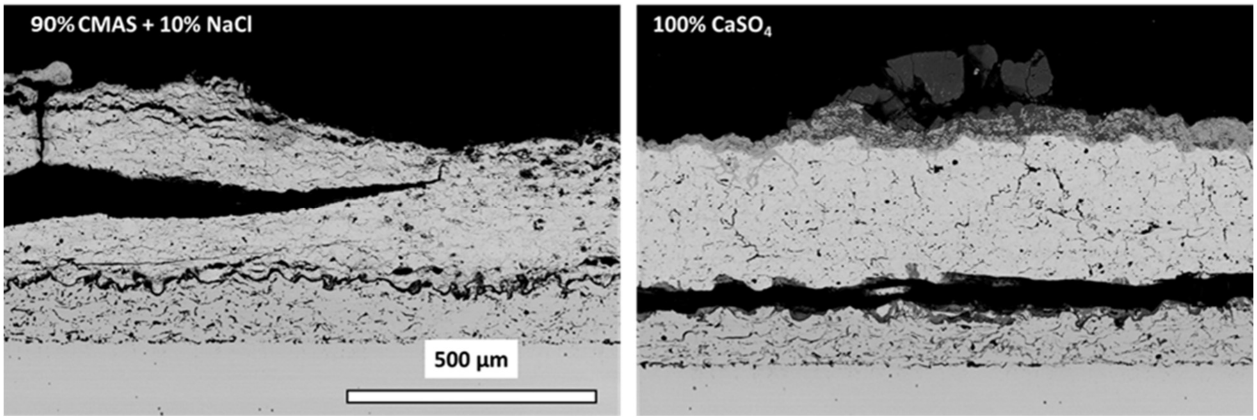

Figure 86. Different coating failure modes observed for CMAS-rich deposits compared to $CaSO_4$-rich deposits for 2 h at 1250 °C

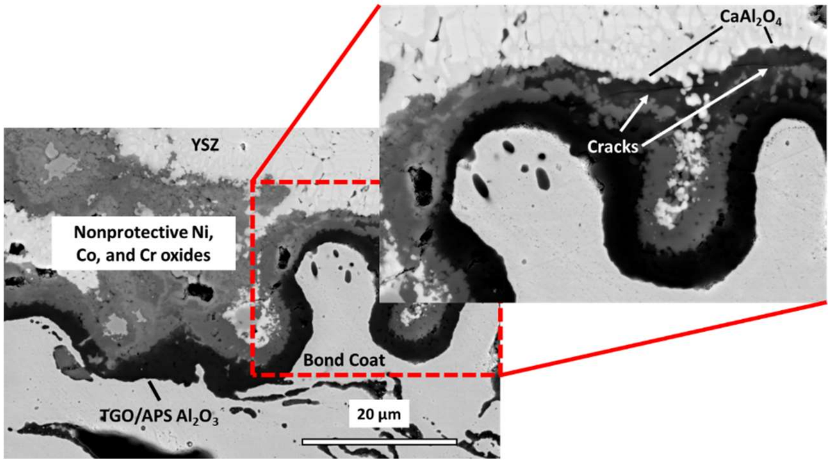

Figure 87. SEM Images of the TBC-bond coat interface for the 100% $CaSO_4$ exposure for 2 h at 1250 °C

6.4.2 NiCoCrAlY and complex deposits

Table 17 shows that the weight gain of Alloy 2 (43.6 Ni/25.6 Co/16.4 Cr/14.3 Al/0.1 Y) exposed at 1250 °C with deposit loadings specified in Table 16 is relatively low at 1 mg/cm^2, with little variation with deposit composition. Figure 88, Figure 89, and Figure 90 all show modest oxidation rather than the more significant corrosion product observed beneath the TBC in Figure 87. All exposures resulted in significant Al depletion and a resulting β→γ phase transformation beneath the scale. The yttrides are preferentially oxidized due to the reactivity of Y, as explained in "4.6.2 The effects of yttrium and yttrides". The $CaSO_4$-rich exposures resulted in Al_2O_3 scales approximately 2 µm thick. The mixed $CaSO_4$-CMAS exposures resulted in two-layer scales consisting of Al_2O_3 below and Ca aluminates above. The CMAS exposure cross-sections are more difficult to interpret. The CMAS-rich deposits appeared to be more adherent to the oxide scales and therefore survived sectioning. An Al_2O_3 scale 2 µm thick formed from 100% CMAS exposure. The NaCl-containing CMAS phase separated, with Cr detected in one of the CMAS phases. The Al_2O_3 scale was either absent or too thin to resolve.

Table 17. Weight gain of Alloy 2 (43.6 Ni/25.6 Co/16.4 Cr/14.3 Al/0.1 Y) after 2 h furnace exposure at 1250 °C with 20 mg/cm² deposit

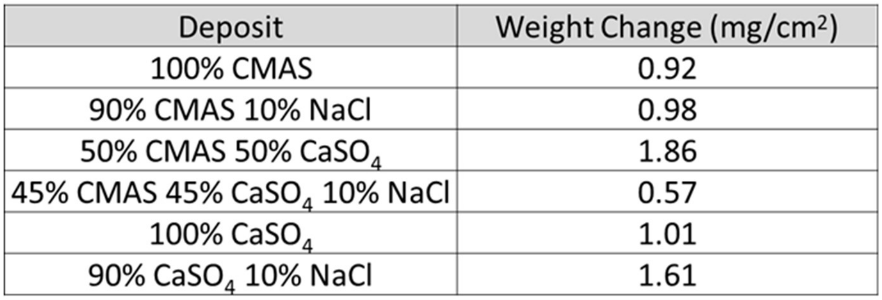

Deposit	Weight Change (mg/cm²)
100% CMAS	0.92
90% CMAS 10% NaCl	0.98
50% CMAS 50% $CaSO_4$	1.86
45% CMAS 45% $CaSO_4$ 10% NaCl	0.57
100% $CaSO_4$	1.01
90% $CaSO_4$ 10% NaCl	1.61

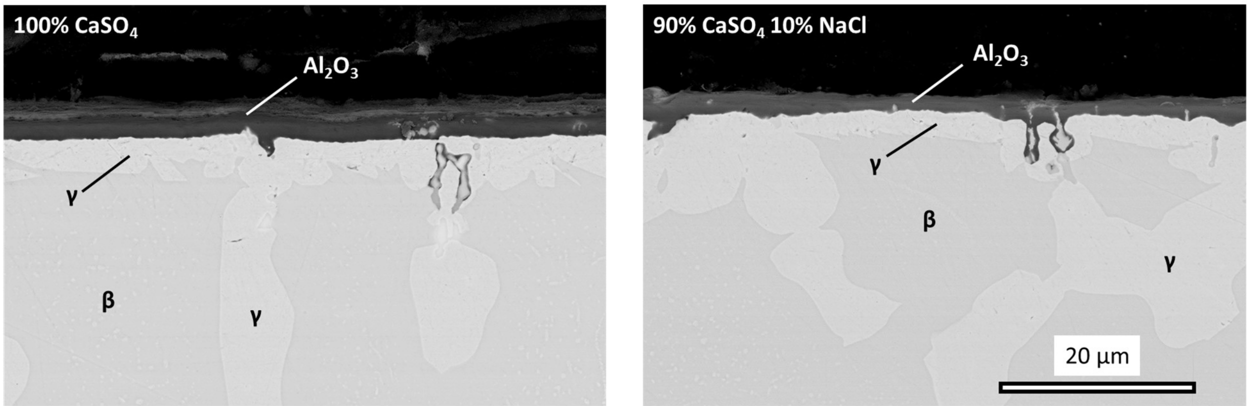

Figure 88. Cross-sectional SEM images of Alloy 2 exposed to the CaSO$_4$-rich deposits for 2 h at 1250 °C

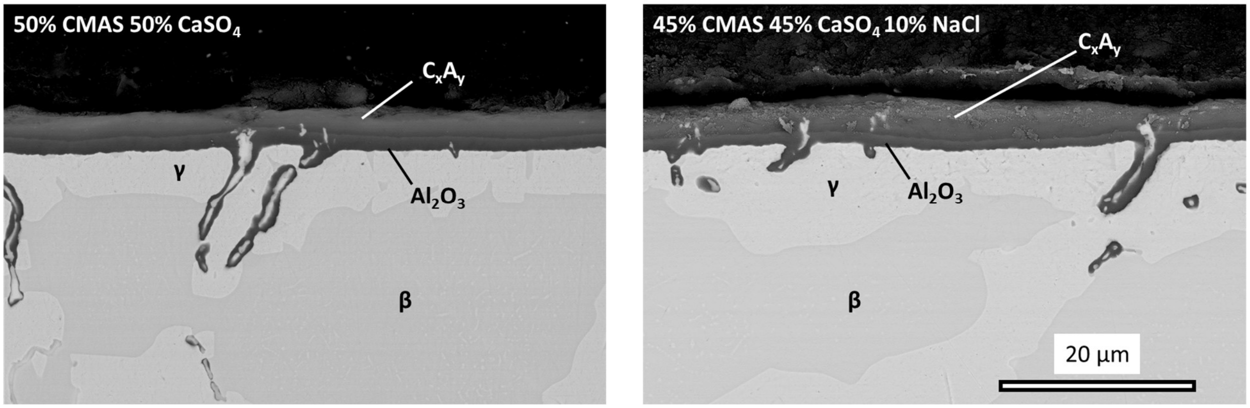

Figure 89. Cross-sectional SEM images of Alloy 2 exposed to the mixed CMAS-CaSO$_4$ deposits for 2 h at 1250 °C

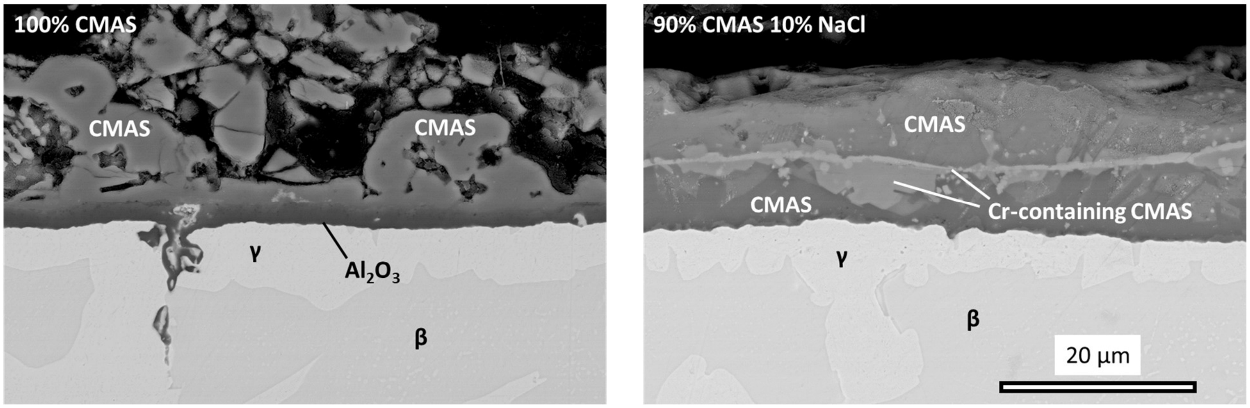

Figure 90. Cross-sectional SEM images of Alloy 2 exposed to the CaSO$_4$-rich deposits for 2 h at 1250 °C

Lastly, an example of a machine learning model prediction for hypothetical Ni-25Cr and Co-25Cr alloys exposed to 2 mg/cm^2 Na_2SO_4 and 1000 ppm SO_3 for 12 h is shown in Figure 91. This is an example illustrating the model's capabilities, comparing predictions with observed trends in the literature (for example, Figure 5).

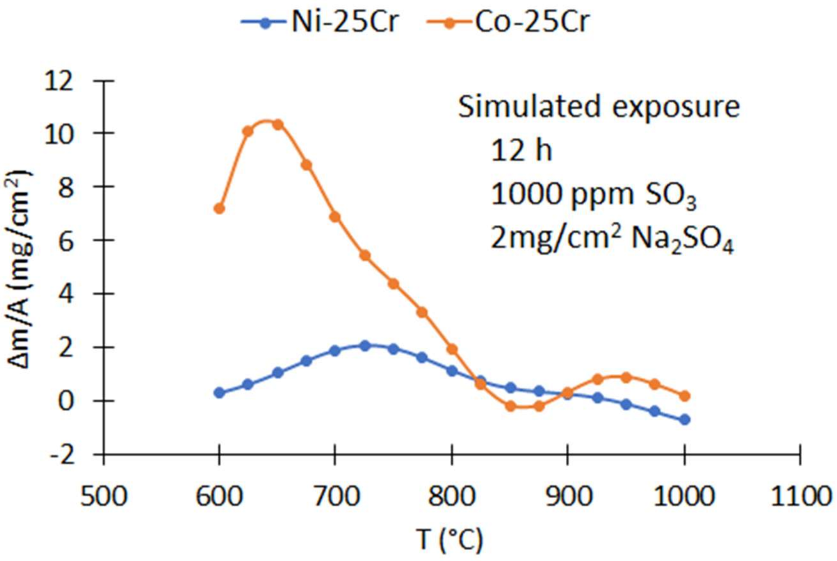

Figure 91. An example of a machine learning prediction for a hypothetical hot corrosion experiment for Ni-25Cr and Co-25

6.5 Discussion

6.5.1 YSZ

The CMAS-$CaSO_4$ corrosion of YSZ TBCs exhibited three main modes of attack, distinguished by the identity of the reaction product. Pure CMAS deposits resulted in a melt infiltrating cracks, pores, and grain boundaries, partial dissolution of YSZ, loss of Y_2O_3 stabilization, and subsequent cracking. These results are consistent with CMAS degradation mechanisms described in the literature [117–121].

The $CaZrO_3$ perovskite phase that formed from exposure to pure $CaSO_4$ has been observed on aero engine turbine blades by Braue [46,47,123]. The deposits observed by Braue consisted of CMAS with $CaSO_4$, Fe_2O_3, and TiO_2, referred to as "FTCMAS". The reaction of YSZ with FTCMAS is shown in Figure 92. $CaSO_4$ tended to separate from the rest of this deposit and infiltrate deeper into the YSZ channels, exposing YSZ columns to relatively pure $CaSO_4$. This resulted in $CaZrO_3$ formation at the column tips and within the channels between columns. Braue proposes two possible explanations for the $CaSO_4$ separation from the FTCMAS. One is that relatively pure $CaSO_4$ deposited on the YSZ prior to deposition of sand/dust-derived deposition of FTCMAS. Another is that separation of the $CaSO_4$ from the FTCMAS possibly results from a miscibility gap between sulfate-rich and sulfate-poor liquid phases.

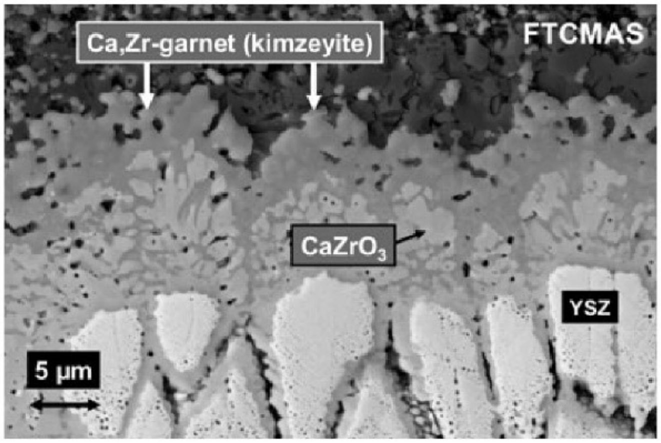

Figure 92. Cross-sectional SEM image of a YSZ coating reacting with FTCMAS from field hardware. Reprinted from "Recession of an EB-PVD YSZ Coated Turbine Blade by $CaSO_4$ and Fe, Ti-Rich CMAS-Type Deposits" 4485, Copyright (2011) [47], with permission from John Wiley & Sons - Books.

Braue also observed that a silicate containing Ca and Zr formed above the $CaZrO_3$ reaction layer, where $CaSO_4$ was intermixed with CMAS silicate. The silicate observed on the field hardware was identified as $Ca_3(Zr,Ti,Fe,)_2(Al,Fe,Si)_3O_{12}$, a silicate with a garnet crystal structure and the mineral name kimzeyite. While the reaction product formed by mixed CMAS-$CaSO_4$ on YSZ in the present study, $Ca_3ZrSi_2O_9$ (baghdadite), is different from that observed in field hardware, the difference is easily explained by the differences in CMAS composition. Qualitatively, the results are the same. $CaSO_4$ mixed with CMAS reacting with YSZ results in a Ca-Zr-silicate, with the exact identity of the silicate dependent upon the deposit composition. Only relatively pure $CaSO_4$ reacting with YSZ forms the $CaZrO_3$ perovskite. In fact, reactions of $CaZrO_3$ and FTCMAS powders above 1200°C show that $CaZrO_3$ transforms to Ca-Zr-silicate [47].

The present study supports the hypothesis that the dual layer reaction product observed by Braue was the result of deposition of relatively pure $CaSO_4$, possibly derived from ingestion of sea spray in a coastal region, and only later deposition of FTCMAS from ingested sand, dust, or ash. While in the present work a miscibility gap was observed in the reaction product of YSZ exposed to the molten CMAS-$CaSO_4$ mixture, neither of the immiscible phases consisted of relatively pure sulfate. Both contained appreciable amounts of oxides of Si, Al, Mg, and Ca. The phases also were not in two distinct layers as they were on the field hardware. This suggests that relatively pure $CaSO_4$ does not separate from the CMAS, supporting the hypothesis that Braue's field hardware experienced sequential deposition of $CaSO_4$ and oxides/silicates. However, one cannot rule out the possibility that $CaSO_4$ more easily phase separates from FTCMAS than the UCSB CMAS used in the present study.

The differences in failure modes between pure $CaSO_4$ and pure CMAS may be partially explained by the fact that $CaZrO_3$ is phase stable from room temperature to approximately 2000 °C [135,136] while ZrO_2 (formed from the selective dissolution of Y_2O_3) undergoes a tetragonal to monoclinic phase transformation upon cooling through 1202 °C [135,136]. Therefore $CaZrO_3$, the reaction product formed by reaction of YSZ with $CaSO_4$, may result in less cracking within the coating compared to reaction of YSZ with CMAS due to polymorphic phase transition-induced volume changes. Y_2O_3-poor ZrO_2, the reaction product formed by reaction with CMAS, is more detrimental to the mechanical integrity of the scale. However, reaction of $CaSO_4$ with the bond coat underneath YSZ formed more oxides of Ni, Co, and Cr at the interface, leading to catastrophic debonding of the TBC. A second factor that may reduce intra-coating cracking by $CaSO_4$ compared to that of CMAS is that the coefficient of thermal expansion (CTE) of $CaSO_4$ better matches the CTE of YSZ [47]. Linear CTEs of $CaSO_4$, YSZ, and CMAS are approximately $11 \times 10^{-6}\ K^{-1}$ [137,138], $11\text{-}13 \times 10^{-6}\ K^{-1}$ [139], and $9\text{-}10 \times 10^{-6}\ K^{-1}$ [48,116], respectively. Therefore, filling of pores and cracks by $CaSO_4$ may cause lower thermal mismatch stresses than penetration of CMAS glass.

Lastly, filling of voids, cracks, and grain boundaries of $CaSO_4$ in Figure 79 and Figure 80 suggest penetration of a liquid, especially considering the short exposure time (2 h at 1250 °C followed by a temperature decrease of 6 °C/min to room temperature). However, $CaSO_4$ melts at approximately 1460 °C [140]. One possible explanation is the formation of a low-melting $CaSO_4$-$Y_2(SO_4)_3$ eutectic. This hypothesis is supported by two facts. The first is that Y_2O_3 is not detected in the $CaZrO_3$ product, and so it must be rejected from reacting YSZ grains. The only possible Y_2O_3 sinks are the other YSZ grains, the $CaSO_4$ deposit, or both. Secondly, Y_2O_3's strong tendency to form sulfates has been previously demonstrated, and it is more stable than $CaSO_4$ [94]. Therefore, the proposed displacement reaction in Equation 27 would result in a $CaSO_4$-$Y_2(SO_4)_3$ mixture in the case of excess $CaSO_4$.

$$3\mathrm{CaSO_4} + \mathrm{Y_2O_3} \leftrightarrow \mathrm{Y_2(SO_4)_3} + 3\mathrm{CaO} \tag{27}$$

Unfortunately, there are no data available on the melting points of $CaSO_4$-$Y_2(SO_4)_3$ mixtures, so it cannot yet be confirmed that these mixtures form a melt at ≤ 1250 °C. DSC of $CaSO_4$-$Y_2(SO_4)_3$ mixtures should be performed in the future to determine melting points of this system.

To conclude, the three different deposit chemistries resulted in three different corrosion products after reaction with YSZ. Exposures to pure CMAS resulted in selective dissolution of Y_2O_3 from YSZ grains, exposure to pure $CaSO_4$ resulted in $CaZrO_3$, and 50-50 wt% CMAS-$CaSO_4$ resulted in a Ca-Zr-silicate, in this case $Ca_3ZrSi_2O_9$ (baghdadite). The different reaction products resulting from different deposit chemistries provided clear descriptors for the qualitative machine learning classification of degradation modes. In the future, more experimental data could be used to train machine learning models to predict corrosion products/modes over a more continuous range of relative CMAS-$CaSO_4$ content.

6.5.2 NiCoCrAlY

Alloy 2 clearly needed CMAS/$CaSO_4$ exposure longer than 2 h to exhibit significant corrosion. This is somewhat surprising given that the NiCoCrAlY TBC bond coat, which has a similar composition, corroded significantly. This too may be explained by the presence of a $CaSO_4$-$Y_2(SO_4)_3$ melt due to reaction with YSZ. The Y content of Alloy 2 (0.1 wt%) is significantly less than that of YSZ (≈ 4 wt%). Therefore, most of the $CaSO_4$ deposit on Alloy 2 remained solid, resulting in minimal reaction over the exposure period. This is consistent with the relatively Ca-free Al_2O_3 scale observed on Alloy 2 when exposed to pure $CaSO_4$.

The $CaSO_4$-CMAS mixture likely melts at 1250 °C (T_m of the CMAS component is 1208 °C) and results in reaction with the Al_2O_3 scale to form Ca aluminates. These aluminates are denoted here as Ca_xA_y because there are multiple Ca aluminates and EDS lacks the accuracy to distinguish between them. The formation of Ca_xA_y-Al_2O_3 scale is consistent with the observations of Gheno, Gleeson, Meier, and Brennan [70–72,128] on reaction of NiCoCrAlY alloys with CaO/$CaSO_4$. They observed the transition to Cr_2O_3/chromate formation at longer exposure times ($\geq$ 50 h). The Al-depleted zone and $\beta \rightarrow \gamma$ transformation observed in the present study may foreshadow similar results, as Cr oxidation will proceed more rapidly as the Al reservoir further depletes.

The results for 100% CMAS and 90% CMAS-10% NaCl reactions with Alloy 2 are more ambiguous. A Ca_xA_y reaction product is not observed, and a detectable Al_2O_3 scale is observed only in the case of the 100% CMAS deposit. The phase separation of the 90% CMAS-10% NaCl is intriguing, especially as EDS suggests that dissolution of Cr from the alloy may play a role. It is not clear why the presence of 10% NaCl contributes to the phase separation. One may speculate that NaCl further decreases the melting point, as suggested by Table 15. The presence of liquid at lower temperatures during cooling could then be more vulnerable to liquid phase separations. However, future work is necessary to confirm the proposed mechanisms, specifically DSC of CMAS-NaCl mixtures. The Alloy 2 experiments would benefit from longer exposure times to obtain larger weight changes and thicker reaction product layers.

Lastly, the machine learning model prediction in Figure 91 appears promising because it qualitatively captures known trends of corrosion rate with temperature and composition. The prediction shows two temperature ranges of increased corrosion rate, one at around 650-750 °C and another at 900-1000 °C. This is in good agreement with the well-known LTHC and HTHC (or Type II and Type I) modes of hot corrosion explained previously in Figure 5. It also predicts an increased corrosion rate of Co-25Cr compared to Ni-25Cr, especially at LTHC temperatures. This is also expected because of the greater stability of $CoSO_4$ compared to $NiSO_4$ and the lower eutectic temperature of $CoSO_4$-Na_2SO_4 compared to $NiSO_4$- Na_2SO_4 [16,54]. The quantitative predictions of corrosion rates may not be accurate, but the qualitative trends of environment and material variables are correct. This prediction for NiCr and CoCr model alloys does not prove that the machine learning model is predictive for CMAS- and NaCl-containing deposits, but it is a good base on which to incorporate more data on corrosion by complex deposit mixtures.

6.6 Conclusions

The attack of YSZ by CMAS, $CaSO_4$, and CMAS-$CaSO_4$ mixtures at 1250 °C for 2 h exhibited three degradation modes as characterized by the identity of the reaction product, providing relevant descriptors for machine learning models to distinguish modes of attack. Attack of YSZ with UCSB CMAS resulted in filling of cracks and pores with a melt, partial dissolution of YSZ grains, selective dissolution of Y_2O_3 compared to ZrO_2, and cracking within the coating. Attack by pure $CaSO_4$ resulted in a $CaZrO_3$ corrosion product and reduced intra-coating cracking, although the coating delaminated from the bond coat, which corroded significantly. Attack of YSZ by a CMAS-$CaSO_4$ mixture resulted in the formation of a Ca-Zr-silicate, likely $Ca_3ZrSi_2O_9$, and two immiscible deposit phases. The addition of 10 wt% NaCl did not significantly affect the degradation modes, although differences in the amount of degradation could not be assessed. These results are consistent with the characterization of field hardware.

NiCoCrAlY Alloy 2 did not substantially react with pure $CaSO_4$ at 1250 °C and 2 h, likely because the deposit remained solid and because of limited opportunity for the formation of a eutectic. Alloy 2 reacted with CMAS-$CaSO_4$ and CMAS-$CaSO_4$-NaCl mixtures to form a dual layer Ca aluminate-Al_2O_3 scale consistent with other studies of NiCoCrAlY in the presence of CaO/$CaSO_4$ deposits. The reaction of Alloy 2 with pure CMAS and 90% CMAS-10% NaCl was difficult to interpret. There was little reaction besides formation of Al_2O_3, and NaCl caused phase separation in the deposit, including some phases rich in dissolved Cr. All exposures resulted in an Al-depletion layer and a $\beta \rightarrow \gamma$ phase transformation. Future work should include longer exposure times.

The machine learning model successfully captured important Na_2SO_4 hot corrosion trends in temperature and alloy composition. The model predicts HTHC and LTHC phenomena for Ni-25Cr and Co-25Cr at roughly the correct temperatures. It also successfully predicts greater corrosion rates for Co-25Cr than Ni-25Cr, particularly at LTHC conditions. The model appears to be a promising base on which to incorporate more training data on CMAS- and NaCl-containing deposits for predicting hot corrosion of complex alloy/coating/deposit systems.

The preliminary thermochemical calculations in Table 15 predict that some complex, mixed CMAS deposits begin to melt at temperatures as low as 900-1050 °C. While the corrosivity of CMAS deposits on the marine turbine blades could be explained by the formation of a mixed sulfate, as discussed in “4.6.3 The effect of Mg2+,” DSC of various CMAS-$CaSO_4$-NaCl compositions should be performed to confirm these predictions and to seek the lowest realistic deposit melting temperatures. Even if no melting is observed at the low temperatures beneath the platform (≤ 700 °C) it is possible that CMAS glass melts could form at HTHC temperatures (approximately 900 °C). This could help explain the corrosion and fracture of the turbine blade airfoils.

7.0 Summary of findings

Mixed Na_2SO_4-$MgSO_4$ deposits on NiCoCrAlY alloys in the LVBR increased the severity of LTHC as compared to pure Na_2SO_4 deposits. The characterization results were consistent with increased corrosion from greater deposit liquid fractions caused by a lowering of the deposit melting point. This possibly explains the corrosivity of CaO/MgO CMAS-like deposits at temperatures well below the temperatures at which they form a glass melt, as reaction of CaO and MgO with SO_3 could result in mixed sulfates. The shorter-term 48 h furnace exposures exhibited decreased corrosion severity with $MgSO_4$ addition to Na_2SO_4. This was probably due to differences in deposit compositions between the two environments. The LVBR deposits were nearly 50 mol% $MgSO_4$-50 mol% Na_2SO_4, which is completely liquid at 700 °C. The tube furnace deposits of 67 mol% $MgSO_4$-33 mol% Na_2SO_4 had an estimated liquid fraction of 36 mol%. The difference in deposit compositions was due to incomplete conversion of MgO to $MgSO_4$ in the LVBR It is proposed that the LVBR results are more relevant to actual gas turbine conditions because the LVBR exposures involved longer times, thermal cycling, and oxide formation prior to significant deposition.

The LVBR and furnace experiments confirmed the beneficial role of Cr in maintaining a protective scale in LTHC conditions. The concentrations of water-soluble alloying elements from the Na_2SO_4 exposures correlate well with the stabilities of their corresponding sulfates, suggesting acidic fluxing. Increasing Al content and β phase fractions in model alloys caused increasing concentrations of Y in the remaining liquid during casting. This resulted in greater phase fractions of coarse Ni-Al-Y precipitates. These precipitates preferentially corroded to form $Y_2(SO_4)_3$, disrupted the oxide scale, and possibly lowered the melting point of the deposit. These effects increased the amount of corrosion of Alloy 3 compared to Alloys 1 and 2. Yttrides played a lesser role for NiCoCrAlY corrosion with mixed Na_2SO_4-$MgSO_4$ deposits, attributed to attainment of a eutectic over greater fractions of the sample surfaces.

Deposition of Na_2SO_4 in the LVBR was in fair agreement with the CFBL boundary layer vapor deposition model. The deposition mechanism of Mg species was different from that of Na. Mg deposited as MgO and then gradually reacted with SO_3 to form $MgSO_4$. Significant water-soluble Mg^{2+} was detected for the mixed Na^+-Mg^{2+} exposure while nearly none was detected for the pure Mg^{2+} exposure. This suggests that the presence of Na_2SO_4 contributes to greater and/or faster sulfation of MgO and that the deposition rate of Na_2SO_4 plays a critical role in sulfating other oxides in the system. The morphology of deposits on LVBR samples and on gas turbine hardware were significantly different from each other, suggesting that different deposition mechanisms dominate each environment. The field hardware deposits are more suggestive of deposit formation by the impaction of Na_2SO_4 or other Na^+-containing particles. The LVBR deposits appear to form via a vapor deposition mechanism as described by the CFBL model.

The analysis thoroughly investigated the roles of Na, Mg, and all alloying elements of NiCoCrAlY alloys in the formation of low-melting multicomponent deposits. ICP-OES characterization provided quantitative insight into the degree of sulfation of each element. The result is a detailed understanding of this multicomponent system and the effects of varying deposit composition, alloy composition, and alloy phase fraction on LTHC. This understanding was expanded upon in a preliminary investigation of mixed CMAS-$CaSO_4$-NaCl corrosion of YSZ and a NiCoCrAlY alloy. Different modes of attack were identified according to the different corrosion products formed.

All these findings constitute a systematic analysis of complex, multicomponent material-environment interactions and their impact on low temperature hot corrosion mechanisms of NiCoCrAlY alloys.

8.0 Impact

This work provided important insight into interpreting the sparse and seemingly contradictory literature on the effects of Mg^{2+} additions to Na_2SO_4 on low temperature hot corrosion. The use of two different experimental setups, the LVBR and the tube furnace, demonstrated that the effects of mixed Mg- and Na-containing deposits may be more sensitive to experimental conditions (particularly $MgSO_4$ content of the deposit, exposure time, and thermal cycling) compared to corrosion induced by pure Na_2SO_4. It was determined that Mg^{2+} likely accelerates low temperature hot corrosion in gas turbine conditions (long exposure times and thermal cycling). Previous studies showing lower corrosion rates with Mg^{2+} additions at isothermal conditions and for relatively short times (< 200 h) may now be reinterpreted in this context.

ICP-OES of water-soluble deposits provided uniquely quantitative insights into the relative amounts of Na^{+}, Mg^{2+}, Ni^{2+}, $Co^{2+/3+}$, $Cr^{3+/6+}$, Al^{3+}, and Y^{3+} salts in the deposits and reaction products. The detrimental effects of Y^{3+} compared to Ni^{2+} and $Co^{2+/3+}$, as well as the correlation between $Y_2(SO_4)_3$ and yttride phase fractions, were quantified. Previous studies only report the qualitative observation that yttride phases corrode preferentially. The effects of $Y_2(SO_4)_3$ disrupting protective scales and causing melting of the deposit are likely more significant than previously thought, comparable to the effects of $NiSO_4$ and $CoSO_4$ if there are coarse yttrides present. New insights were obtained on the deposition process of both Na_2SO_4 and mixed deposits. The ICP-OES results revealed that MgO deposits convert to $MgSO_4$ more quickly in the presence of Na_2SO_4. The sluggish transformation (beginning after 180 h of exposure) of MgO to $MgSO_4$ was observed, providing insight into the kinetics of MgO sulfation. ICP-OES, SEM/EDS, and a mass transport model revealed different deposition mechanisms in the LVBR for Na^{+} (vapor deposition, with nucleation and growth occurring on the sample surface) and Mg^{2+} (the accumulation of impacting MgO particles). This difference between Mg^{2+} and Na^{+} deposition has not been reported in the existing literature.

Lastly, preliminary work demonstrated a framework for extending scientific understanding of the reaction of multilayered coating systems with complex CMAS-salt mixtures. Machine learning methods and furnace exposures allowed for the determination and classification of different corrosion modes (e.g. reaction of YSZ with $CaSO_4$ to form $CaZrO_3$ as compared to reaction of YSZ with CMAS, which forms Y-depleted ZrO_2).

Together, these original insights illustrate how hot corrosion/high temperature corrosion in complex, realistic gas turbine environments may be systematically studied. This work contributed important information on hot corrosion in complex deposits which is necessary for explaining the damage observed in field hardware.

9.0 Suggested future work

- Perform more tube furnace exposures to determine the deposit composition, time, thermal cycling, and water vapor dependence on LTHC with complex Na_2SO_4-$MgSO_4$ deposits
    - Hypothesis: deposit compositions closer to the eutectic composition, longer exposures, thermal cycling, and increased amount of water vapor all increasing the corrosion rate in mixed deposits
    - Expose samples to varying Na_2SO_4-$MgSO_4$ composition
    - Expose samples for longer times (closer to the 500 h of the LVBR exposures)
    - Conduct both isothermal and thermally-cycled exposures in the tube furnace to determine if thermal cycling increases corrosion in Mg^{2+}-containing deposits
    - Conduct exposures with varying amounts of water vapor
    - Use larger sample sizes that can be characterized using XRD

- Expand the CMAS-$CaSO_4$-NaCl-induced corrosion literature search and perform more experiments
    - Train the machine learning models on these larger datasets
    - Perform validation experiments to test predictive capabilities of the models

10.0 Other accomplishments during PhD training

1. Project Title: Development of Test Protocols and Testing of Marinized Materials for Mixed Mode Hot Corrosion/Oxidation | Office of Naval Research | Grant No. N00014-14-1-0637
    - Conducted over 8,000 h of LVBR testing (7 tests lasting 1000 hours each and 2 tests lasting 500 hours each) of marine alloys and coatings
    - Characterized samples, measured metal loss for proprietary alloy/coating systems, and reported data (120 pages of data and interpretation of results)

2. Project Title: Design of UHTC for Oxidation Resistance | Office of Naval Research | Grant No. N00014-19-1-2274
    - Assessed the literature on the tantalum-oxygen system
    - Created a preliminary CALPHAD model and phase diagram of the tantalum-oxygen system
    - Publication to be submitted after the liquid phase is accurately modeled

11.0 Publications

Published:

- Hot Corrosion of Shipboard Gas Turbine Blades. *Oxid. Met.* **94**, 301–322 (2020)

Pending:

- Low Temperature Hot Corrosion of NiCoCrAlY Alloys Exposed to Mixed Na-Mg Deposits
- Formation of Deposits in a Low Temperature Hot Corrosion Environment
- CALPHAD Assessment of the Tantalum-Oxygen System

Citations

1. Ellingham, H. J. T. Reducibility of Oxides and Sulfides in Metallurgical Processes. *J. Soc. Chem. Ind. Trans. Commun.* **63**, 125–160 (1944).
2. Wagner, C. Theoretical Analysis of the Diffusion Processes Determining the Oxidation Rate of Alloys. *J. Electrochem. Soc.* **99**, 369–380 (1952).
3. Wagner, C. Reaktionstypen bei der Oxydation von Legierungen. *Z. Elektrochem.* **63**, 772–782 (1959).
4. Wagner, C. Formation of Composite Scales Consisting of Oxides of Different Metals. *J. Electrochem. Soc.* **103**, 627 (1956).
5. Young, D. J. *High Temperature Oxidation and Corrosion of Metals*. (2016). doi:10.1016/s1875-9491(08)00023-9.
6. Kofstad, P. High Temperature Corrosion. (1988).
7. Zhang, Z. G., Gesmundo, F., Hou, P. Y. & Niu, Y. Criteria for the formation of protective Al_2O_3 scales on Fe-Al and Fe-Cr-Al alloys. *Corros. Sci.* **48**, 741–765 (2006).
8. Hou, P. Y. & Stringer, J. The effect of reactive element additions on the selective oxidation, growth and adhesion of chromia scales. *Mater. Sci. Eng. A* **202**, 1–10 (1995).
9. Stringer, J. The reactive element effect in high-temperature corrosion. *Mater. Sci. Eng. A* **120–121**, 129–137 (1989).
10. Whittle, D. P. & Stringer, J. Improvements in High Temperature Oxidation Resistance by Additions of Reactive Elements or Oxide Dispersions. *Philos. Trans. R. Soc. A Math. Phys. Eng. Sci.* **295**, 309–329 (1980).
11. B.A. Pint. Progress in Understanding the Reactive Element Effect Since the Whittle and Stringer Literature Review. *Proc. John Stringer Symp. High Temp. Corros. Citeseer* 9–19 (2003).
12. Mendis, B. G., Livi, K. J. T. & Hemker, K. J. Observations of reactive element gettering of sulfur in thermally grown oxide pegs. *Scr. Mater.* **55**, 589–592 (2006).
13. Smialek, J. L. Effect of Sulfur Removal on Al_2O_3 Scale Adhesion. *Metall. Trans. A* **22**, 739–752 (1991).
14. Meier, G. H., Pettit, F. S. & Smialek, J. L. The effects of reactive element additions and sulfur removal on the adherence of alumina to Ni- and Fe-base alloys. *Mater. Corros.* **240**, 232–240 (1995).
15. Quadakkers, W. J., Holzbrecher, H., Briefs, K. G. & Beske, H. Differences in Growth Mechanisms of Oxide Scales Formed on ODS and Conventional Wrought Alloys. *Oxid. Met.* **32**, 67–88 (1989).
16. Pettit, F. Hot Corrosion of Metals and Alloys. *Oxid. Met.* **76**, 1–21 (2011).
17. DeCrescente, M. A. & Bornstein, N. S. Formation and Reactivity Thermodynamics of Sodium Sulfate With Gas Turbine Alloys. *Corrosion* **24**, 127–133 (1968).
18. Nishikata, A., Numata, H. & Tsuru, T. Electrochemistry of molten salt corrosion. *Mater. Sci. Eng. A* **146**, 15–31 (1991).
19. Burrows, B. W. & Hills, G. J. Electrochemical Studies of Molten Alkali Sulphates. *Electrochim. Acta* **15**, 445–458 (1970).
20. Lewis, G. N. *Valence and the Structure of atoms and molecules*. (The Chemical Catalog Company, Inc., 1923).
21. Rapp, R. A. Hot corrosion of materials: A fluxing mechanism? *Corros. Sci.* **44**, 209–221 (2002).
22. Johnson, D. M., Whittle, D. P. & Stringer, J. Mechanisms of Na_2SO_4-induced accelerated oxidation. *Corros. Sci.* **15**, (1975).
23. Goebel, J. A., Pettit, F. S. & Goward, G. W. Mechanisms for the hot corrosion of nickel-base alloys. *Metall. Trans.* **4**, 261–278 (1973).
24. Rapp, R. A. & Goto, K. S. The Hot Corrosion of Metals by Molten Salts. *ECS Proc. Vol.* **1981–10**, 159–177 (1981).

25. Delahay, P., Pourbaix, M. & Van Rysselberghe, P. Potential-pH diagrams. *J. Chem. Educ.* **27**, 683–688 (1950).
26. Pourbaix, M. *Thermodynamique des solutions aqueuses diluées. Représentation graphique du rôle du pH et du potentiel*. (1945).
27. Rapp, R. A. Whitney Award Lecture—1986: Chemistry and Electrochemistry of the Hot Corrosion of Metals. *Corrosion* **42**, 568–577 (1986).
28. Rapp, R. a., Mehl, R. F. & Medalist, A. Some generalities in the analyses of equilibria in lonic solutions. *Metall. Mater. Trans. A* **31**, 2105–2118 (2000).
29. Zhang, Y. S. Solubilities of Cr_2O_3 in Fused Na2SO4 at 1200 K. *J. Electrochem. Soc.* **133**, 655–657 (1986).
30. Jose, P. D., Gupta, D. K. & Rapp, R. A. Solubility of α-Al_2O_3 in Fused Na_2SO_4 at 1200 K. *J. Electrochem. Soc.* **132**, 735–737 (1985).
31. Schryer, D. Solubility of alpha-Al2O3 in Fused Na2SO4. *J. Electrochem. Soc.* **111**, 758–759 (1985).
32. McCreath, C. G. & Condé, J. F. G. Hot corrosion in marine gas turbines. in *High Temperature Alloys for Gas Turbines* (eds. Brunetaud, R. et al.) 237–247 (Springer, 1982). doi:https://doi.org/10.1007/978-94-009-7907-9_8.
33. Bol'shakov, K. A. & Fedorov, P. I. Study of Sodium Sulfate-Cobalt Sulfate, and Sodium Sulfate-Nickel Sulfate Systems. *Zhurmal Obs. Khimii* **26**, 348–350 (1956).
34. Luthra, K. L. & Leblanc, O. H. Low temperature hot corrosion of CoCrAl alloys. *Mater. Sci. Eng.* **87**, 329–335 (1987).
35. Chase Jr., M. W. *et al.* NIST-JANAF Thermochemical Tables. *National Institute of Standards and Technology* https://janaf.nist.gov/ (1985).
36. Luthra, K. L. & Shores, D. A. Mechanism of Na_2SO_4 Induced Corrosion at 600°–900°C. *J. Electrochem. Soc.* **127**, 2202 (1980).
37. Meisner, K. J. & Opila, E. J. Hot Corrosion of Shipboard Gas Turbine Blades. *Oxid. Met.* **94**, 301–322 (2020).
38. Bale, C. W. *et al.* FactSage thermochemical software and databases. *Calphad Comput. Coupling Phase Diagrams Thermochem.* **26**, 189–228 (2002).
39. Hynes, A. J., Steinberg, M. & Schofield, K. The chemical kinetics and thermodynamics of sodium species in oxygen-rich hydrogen flames. *J. Chem. Phys.* **80**, 2585–2597 (1984).
40. Schofield, K. & Steinberg, M. Sodium/sulfur chemical behavior in fuel-rich and -lean flames. *J. Phys. Chem.* **96**, 715–726 (1992).
41. Schofield, K. The kinetic nature of sulfur's chemistry in flames. *Combust. Flame* **124**, 137–155 (2001).
42. Hanby, V. I. Sodium Sulphate Formation and Deposition in Marine Gas Turbines. *Am. Soc. Mech. Eng.* 129–133 (1973).
43. Kohl, F. J., Santoro, J., Stearns, C. A. & Fryburg, G. C. Theoretical and experimental studies of the deposition of Na_2SO_4 from seeded combustion gases. *J. Electrochem. Soc. Solid-state Sci. Technol.* **126**, 1054–1061 (1979).
44. Krisak, M. B., Bentley, B. I., Phelps, A. W. & Radsick, T. C. Review of calcium sulfate as an alternative cause of hot corrosion. *Journal of Propulsion and Power* vol. 33 697–703 (2017).
45. Smialek, J. L., Archer, F. A. & Garlick, R. G. *Chemistry of Saudi Arabian sand: a deposition problem on helicopter turbine airfoils*. *NASA Technical Memorandum 105234* (1991).
46. Braue, W. Environmental stability of the YSZ layer and the YSZ/TGO interface of an in-service EB-PVD coated high-pressure turbine blade. *J. Mater. Sci.* **44**, 1664–1675 (2009).
47. Braue, W. & Mechnich, P. Recession of an EB-PVD YSZ coated turbine blade by $CaSO_4$ and Fe, Ti -Rich CMAS-Type deposits. *J. Am. Ceram. Soc.* **94**, 4483–4489 (2011).
48. Wiesner, V. L. & Bansal, N. P. Mechanical and thermal properties of calcium-magnesium aluminosilicate (CMAS) glass. *J. Eur. Ceram. Soc.* **35**, 2907–2914 (2015).
49. Bansal, N. P. & Choi, S. R. Properties of CMAS glass from desert sand. *Ceram. Int.* **41**, 3901–3909 (2015).

50. Shifler, D. A. *et al.* CMAS Effects on Ship Gas-Turbine Components / Materials. in *Proceedings of the ASME Turbo Expo 2018: Turbine Technical Conference & Exposition GT2018* 1–12 (2018).
51. Shifler, D. A. The Increasing Complexity of Hot Corrosion. *J. Eng. Gas Turbines Power* (2017) doi:10.1115/1.4038037.
52. Shifler, D. A. & Choi, S. R. CMAS Effects on Ship Gas-Turbine Components/Materials. in *Proceedings of ASME Turbo Expo 2018 Turbomachinery Technical Conference and Exposition GT2018* (2018).
53. Harris, K., Erickson, G. L. & Schwer, R. E. Mar M 247 Derivations - CM 247 LC DS Alloy CMSX Single Crystal Alloys Properties & Performance. *Superalloys 1984* 221–230 (1984) doi:10.1353/shb.0.0105.
54. Wortman, D. J., Fryxell, R. E., Luthra, K. L. & Bergman, P. A. Mechanism of Low Temperature Hot Corrosion: Burner Rig Studies. *Thin Solid Films* **64**, 281–288 (1979).
55. Luthra, K. L. Low Temperature Hot Corrosion of Cobalt-Base Alloys: Part II. Reaction Mechanism. *Metall. Trans. A* **13**, 1853–1864 (1982).
56. Degen, T., Sadki, M., Bron, E., Konig, U. & Nenert, G. The HighScore suite. *Powder Diffr.* **29**, S13–S18 (2014).
57. ASTM. D1141-98 Standard Practice for the Preparation of Substitute Ocean Water. *Astm* **98**, 1–3 (2013).
58. Du, H. Thermodynamic Assessment of the K_2SO_4-Na_2SO_4-$MgSO_4$-$CaSO_4$ System. *J. Phase Equilibria* **21**, 6–18 (2000).
59. Shifler, D. A., Russom, D. M. & Rodman, B. E. Evaluating the Hot Corrosion Effects of High Temperature Coatings for Marine Gas Turbines. *Corrosion* (20005).
60. Kosieniak, E., Biesiada, K., Kaczorowski, J. & Innocenti, M. Corrosion failures in gas turbine hot components. *J. Fail. Anal. Prev.* **12**, 330–337 (2012).
61. Tschinkel, J. Formation of Sodium Sulfate in Gas Turbine Combustors. *Corrosion* **28**, 161–169 (1972).
62. Hwang, Y.-S. & Rapp, R. A. Synergistic Dissolution of Oxides in Molten Sodium Sulfate. *J. Electrochem. Soc.* **137**, 1276 (1990).
63. Alvarado-Orozco, J. M., Garcia-Herrera, J. E., Gleeson, B., Pettit, F. S. & Meier, G. H. Reinterpretation of Type II Hot Corrosion of Co-Base Alloys Incorporating Synergistic Fluxing. *Oxid. Met.* **90**, 527–553 (2018).
64. Zheng, X. & Rapp, R. A. Electrochemical Impedance of a Platinum Electrode in Fused Na_2SO_4 Melts in SO_2-O_2 Environments. *J. Electrochem. Soc.* **140**, 2857 (1993).
65. Luthra, K. L. Mechanism of oxidation-sulfation reactions of CoO in the presence of Na_2SO_4. *Metall. Trans. A* **13**, 1647–1654 (1982).
66. Luthra, K. L. Low Temperature Hot Corrosion of Cobalt-Base Alloys: Part I. Morphology of the Reaction Product. *Metall. Trans. A* **13**, 1843–1852 (1982).
67. Gheno, T., Zahiri Azar, M., Heuer, A. H. & Gleeson, B. Reaction morphologies developed by nickel aluminides in type II hot corrosion conditions: The effect of chromium. *Corros. Sci.* **101**, 32–46 (2015).
68. Chiang, K. T., Meier, G. H. & Perkins, R. A. The effects of deposits of CaO, $CaSO_4$, and MgO on the oxidation of several Cr_2O_3-forming and Al_2O_3-forming alloys. *J. Mater. Energy Syst.* **6**, 71–86 (1984).
69. Nagarajan, V., Smith, R. D. & Wright, I. G. Influence of solid-state CaS-CaO-$CaSO_4$ deposits on corrosion of high-temperature alloys in simulated FBC environments. *Oxid. Met.* **31**, 325–340 (1989).
70. Gheno, T., Meier, G. H. & Gleeson, B. High Temperature Reaction of MCrAlY Coating Compositions with CaO Deposits. *Oxid. Met.* **84**, 185–209 (2015).
71. Gheno, T. & Gleeson, B. On the Reaction Mechanism of MCrAlY Alloys with Oxide–Sulfate Deposits at 1100 °C. *Oxid. Met.* **86**, 385–406 (2016).
72. Gheno, T. & Gleeson, B. Modes of Deposit-Induced Accelerated Attack of MCrAlY Systems at

1100 °C. *Oxid. Met.* **87**, 249–270 (2017).

73. Yazhenskikh, E., Jantzen, T., Kobertz, D., Hack, K. & Müller, M. Critical thermodynamic evaluation of the binary sub-systems of the core sulphate system Na_2SO_4–K_2SO_4–$MgSO_4$–$CaSO_4$. *Calphad Comput. Coupling Phase Diagrams Thermochem.* **72**, (2021).
74. Dexter, S. J. & Culberson. Global Variability of Natural Sea Water. *Mater. Perform.* **19**, 16 (1980).
75. Tang, Z. & Gleeson, B. Unpublished work.
76. Bornstein, N. S. Reviewing Sulfidation Corrosion- Yesterday and Today. *J. Met.* **48**, 37–39 (1996).
77. Jones, R. L. & Williams, C. E. *Mixed* $MgSO_4$*-*Na_2SO_4 *Effects in the 973 K Hot Corrosion of CoCrAlY.*
78. Lowell, C. E., Sidik, S. M. & Deadmore, D. L. Effect of sodium, potassium, calcium, and chlorine on the high temperature corrosion of In-100, U-700, IN-792, and Mat M-509. *Trans. ASME* **103**, 294–307 (1981).
79. Task, M. N., Gleeson, B., Pettit, F. S. & Meier, G. H. The effect of microstructure on the type II hot corrosion of Ni-base MCrAlY alloys. *Oxid. Met.* **80**, 125–146 (2013).
80. Luthra, K. L. Kinetics of the Low Temperature Hot Corrosion of Co-Cr-Al Alloys. *J. Electrochem. Soc.* **132**, 1293–1298 (1985).
81. Schneider, C. A., Rasband, W. S. & Eliceiri, K. W. NIH Image to ImageJ: 25 years of image analysis. *Nature Methods* vol. 9 671–675 (2012).
82. Rueden, C. T. *et al.* ImageJ2: ImageJ for the next generation of scientific image data. *BMC Bioinformatics* **18**, 529 (2017).
83. Andersson, J. O., Helander, T., Höglund, L., Shi, P. & Sundman, B. Thermo-Calc & DICTRA, computational tools for materials science. *Calphad Comput. Coupling Phase Diagrams Thermochem.* **26**, 273–312 (2002).
84. Puetz, P., Huang, X., Lima, R. S., Yang, Q. & Zhao, L. Characterization of transient oxide formation on CoNiCrAlY after heat treatment in vacuum and air. *Surf. Coat. Technol.* **205**, 647–657 (2010).
85. Injeti, G. Identification of a smart bond coating for gas turbine engine applications. *J. Coatings Technol. Res.* **5**, 385–391 (2008).
86. Jackson, E. M. M. *et al.* Effect of surface preparation on the durability of NiCoCrAIY coatings for oxidation protection and bond coats for thermal barrier coatings. *Mater. Corros.* **59**, 494–500 (2008).
87. Sumner, J., Encinas-Oropesa, A., Simms, N. & Nicholls, J. R. Type II hot corrosion: Behaviour of CMSX-4 and IN738LC as a function of corrosion environment. *Mater. Corros.* 188–196 (2014) doi:10.1002/maco.201307425.
88. Luthra, K. L. & Wood, J. H. High Chromium Cobalt-Base Coatings for Low Temperature Ht Corrosion. *Thin Solid Films* **119**, 271–280 (1984).
89. Shih, S., Zhang, Y. & Li, X. *Sub-melting Point Hot Corrosion of Alloys and Coatings*. Materials Science and Engineering, A* vol. 120 (1989).
90. Task, M. N., Gleeson, B., Pettit, F. S. & Meier, G. H. Compositional factors affecting protective alumina formation under type II hot corrosion conditions. *Oxid. Met.* **80**, 541–552 (2013).
91. Alvarado-Orozco, J. M., Garcia-Herrera, J. E., Gleeson, B., Pettit, F. S. & Meier, G. H. Reinterpretation of Type II Hot Corrosion of Co-Base Alloys Incorporating Synergistic Fluxing. *Oxid. Met.* **90**, 527–553 (2018).
92. Fukumoto, M., Suzuki, T., Sano, M., Hirade, M. & Kara, M. Solubility of metal oxides under control of basicity by electrolysis in fused Na_2SO_4. *Mater. Trans.* **45**, 2994–2998 (2004).
93. Kuenzly, J. D. & Douglass, D. L. The oxidation mechanism of Ni3Al containing yttrium. *Oxid. Met.* **8**, 139–178 (1974).
94. Jones, R. L., Nordman, D. B. & Gadomski, S. T. Sulfation of Y_2O_3 and HfO_2 in relation to MCrAl coatings. *Metall. Trans. A* **16**, 303–306 (1985).
95. Eysel, W., Höfer, H. H., Keester, K. L. & Hahn, T. Crystal chemistry and structure of Na2SO4(I) and its solid solutions. *Acta Crystallogr. Sect. B* **41**, 5–11 (1985).
96. Rahmel, A., Schmidt, M. & Schorr, M. The influence of electrode potential on the corrosion of gas

turbine alloys in sulfate melts. *Oxid. Met.* **18**, 195–223 (1982).

97. Wu, W. T. & Rahmel, A. Inhibition of Hot Corrosion by MgSO4 and BaSO4 and its potential dependence. *Mater. Corros.* **35**, 139–149 (1984).
98. Shifler, D. A. Hot corrosion: a modification of reactants causing degradation. *Mater. High Temp.* **35**, 225–235 (2018).
99. Rosner, D. E., Chen, B.-K., Fryburg, G. C. & Kohl, F. J. Chemically Frozen Multicomponent Boundary Layer Theory of Salt and/ or Ash Deposition Rates from Combustion Gases. *Combust. Sci. Technol.* **20**, 87–106 (1979).
100. Santoro, G. J., Gokoglu, S. A., Kohl, F. J., Stearns, C. A. & Rosner, D. A. Deposition of Na2SO4 from Salt-Seeded Combustion Gases of a High Velocity Burner Rig. *AIME, Metall. Soc* 417–434 (1985).
101. Rosner, D. E. & Liang, B. Laboratory Studies of the Deposition of Alkali Sulfate Vapors from Combustion Gases Using a Flash-Evaporation Technique. *Chem. Eng. Commun.* **42**, 171–190 (1986).
102. Stearns, C. A., Kohl, F. J. & Rosner, D. E. Combustion System Processes Leading to Corrosive Deposits. in *High Temperature Corrosion* (ed. Rapp, R. A.) 441–450 (National Association of Corrosion Engineers, 1981).
103. Rosner, D. E., Chen, B.-K., Fryburg, G. C. & Kohl, F. J. Rosner CombSciTech 1979.pdf. *Combust. Sci. Technol.* **20**, 87–106 (1979).
104. Gordon & McBride. *NASA SP-273: Computer Program for Calculation of Complex Chemical Equilibrium Compositions, Rocket Performance. Incident and Reflected Shock. and Chapman-Jouguet Detonations*. (1976).
105. Churchill, S. W. & Bernstein, M. A Correlating Equation for Forced Convection From Gases and Liquids to a Circular Cylinder in Crossflow. *J. Heat Transfer* **99**, 300 (1977).
106. Chapman, S. & Cowling, T. G. *The Mathematical Theory of Non-Uniform Gases*. (Cambridge University Press, 1995).
107. Svehla, R. A. *Estimated Viscosities And Thermal Conductivities Of Gases At High Temperatures*. https://ntrs.nasa.gov/search.jsp?R=19630012982 (1962).
108. *CRC Handbook of Chemistry and Physics (Internet Version)*. (CRC Press/Taylor & Francis, 2018).
109. Sherwood, T. K., Pigford, R. L. & Wilke, C. R. *Mass Transfer*. (McGraw-Hill, 1975).
110. Rasmussen, S. E., Jørgensen, J. E. & Lundtoft, B. Structures and Phase Transitions of Na_2SO_4. *J. Appl. Crystallogr.* **29**, 42–47 (1996).
111. Welty, Wicks, Wilson & Rorrer. *Fundamentals of Momentum, Heat, and Mass Transfer*. (Wiley Global Education, 2007).
112. Armbruster, T., Basler, R., Mikhail, P. & Hulliger, J. Defect-Structure of Ytterbium(III) Doped Na2SO4 Phase I. *J. Solid State Chem.* **145**, 309–316 (1999).
113. Cooper, T. G. & de Leeuw, N. H. A computer modelling study of the incorporation of K^+, Ca^{2+} and Mg^{2+} impurities in two Na_2SO_4 polymorphs: Introducing a Na_2SO_4 potential model. *J. Cryst. Growth* **294**, 137–149 (2006).
114. Höfer, H. H., Eysel, W. & von Alpen, U. Electrochemistry of Na_2SO_4 (I) solid solutions with aliovalent cation substitution. *J. Solid State Chem.* **36**, 365–370 (1981).
115. Misra, A. K., Whittle, D. P. & Worrell, W. L. Thermodynamics of Molten Sulfate Mixtures. *J. Electrochem. Soc.* **129**, 1840–1845 (1982).
116. Bansal, N. P. & Choi, S. R. Properties of CMAS glass from desert sand. *Ceram. Int.* **41**, 3901–3909 (2015).
117. Krämer, S., Yang, J., Levi, C. G. & Johnson, C. A. Thermochemical interaction of thermal barrier coatings with molten CaO-MgO-Al_2O_3-SiO_2 (CMAS) deposits. *J. Am. Ceram. Soc.* **89**, 3167–3175 (2006).
118. Vidal-Setif, M. H., Chellah, N., Rio, C., Sanchez, C. & Lavigne, O. Calcium-magnesium-alumino-silicate (CMAS) degradation of EB-PVD thermal barrier coatings: Characterization of CMAS damage on ex-service high pressure blade TBCs. *Surf. Coatings Technol.* **208**, 39–45 (2012).

119. Krämer, S. *et al.* Mechanisms of cracking and delamination within thick thermal barrier systems in aero-engines subject to calcium-magnesium-alumino-silicate (CMAS) penetration. *Mater. Sci. Eng. A* **490**, 26–35 (2008).
120. Cai, Z., Jiang, J., Wang, W., Liu, Y. & Cao, Z. CMAS penetration-induced cracking behavior in the ceramic top coat of APS TBCs. *Ceram. Int.* **45**, 14366–14375 (2019).
121. Cai, Z. *et al.* Stress evolution in ceramic top coat of air plasma-sprayed thermal barrier coatings due to CMAS penetration under thermal cycle loading. *Surf. Coatings Technol.* **381**, (2020).
122. Boissonnet, G., Chalk, C., Nicholls, J., Bonnet, G. & Pedraza, F. Thermal insulation of CMAS (Calcium-Magnesium-Alumino-Silicates)- attacked plasma-sprayed thermal barrier coatings. *J. Eur. Ceram. Soc.* **40**, 2042–2049 (2020).
123. Braue, W., Mechnich, P. & Peters, P. W. M. The $CaSO_4$ phase in fully infiltrated electron-beam physical vapour deposited yttria stabilized zirconia top coats from engine hardware. *Mater. High Temp.* **28**, 315–323 (2011).
124. Rivera-Gil, M. A. *et al.* High temperature interaction of volcanic ashes with 7YSZ TBC's produced by APS: Infiltration behavior and phase stability. *Surf. Coatings Technol.* **378**, 124915 (2019).
125. Yin, B., Zhang, F., Zhu, W., Yang, L. & Zhou, Y. Effect of Al_2O_3 modification on the properties of YSZ: Corrosion resistant, wetting and thermal-mechanical properties. *Surf. Coatings Technol.* **357**, 161–171 (2019).
126. Task, M. N., Gleeson, B., Pettit, F. S. & Meier, G. H. Compositional effects on the Type I hot corrosion of β-NiAl alloys. *Surf. Coatings Technol.* **206**, 1552–1557 (2011).
127. Arbab, M. & Shatynski, S. R. Hot Corrosion of Nickel in Na_2SO_4-$CaSO_4$ Mixtures. *J. Electrochem. Soc.* **132**, 2264–2268 (1985).
128. Brennan, P. T. Environmental Factors Affecting CaO and $CaSO_4$-Induced Degradation of Second-Generation Nickel-Based Superalloys. (University of Pittsburgh, 2020). doi:10.1016/s1347-4367(18)30002-8.
129. Fang, H., Wang, W., Huang, J. & Ye, D. Corrosion resistance and thermal-mechanical properties of ceramic pellets to molten calcium-magnesium-alumina-silicate (CMAS). *Ceram. Int.* **45**, 19710–19719 (2019).
130. Naraparaju, R. *et al.* Estimation of CMAS infiltration depth in EB-PVD TBCs: A new constraint model supported with experimental approach. *J. Eur. Ceram. Soc.* **39**, 2936–2945 (2019).
131. Xia, J. *et al.* On the resistance of rare earth oxide-doped YSZ to high temperature volcanic ash attack. *Surf. Coatings Technol.* **307**, 534–541 (2016).
132. Kecman, V. Support Vector Machines - An Introduction. in *Support Vector Machines: Theory and Applications* (ed. Wang, L.) 1–47 (Springer-Verlag Berlin Heidelberg, 2005). doi:10.1007/b95439.
133. Poirier, D. R. & Geiger, G. H. *Transport Phenomena in Materials Processing*. (Springer, 2016).
134. Al-Hermezi, H. M., McKie, D. & Hall, A. J. Baghdadite, a new calcium zirconium silicate mineral from Iraq. *Mineral. Mag.* **50**, 119–123 (1986).
135. Kwon, S. Y. & Jung, I. H. Critical evaluation and thermodynamic optimization of the CaO-ZrO2 and SiO2-ZrO2 systems. *J. Eur. Ceram. Soc.* **37**, 1105–1116 (2017).
136. Jin, Z. & Du, Y. Thermodynamic calculation of the ZrO_2-$YO_{1.5}$-CaO phase diagram. *Calphad* **16**, 355–362 (1992).
137. Ballirano, P. & Melis, E. Thermal behaviour of β-anhydrite $CaSO_4$ to 1,263 K. *Phys. Chem. Miner.* **34**, 699–704 (2007).
138. Khan, A. A. Computer Simulation of Thermal Expansion of Non-Cubic Crystals: Forsterite, Anhydrite and Scheelite. *Acta Crystallogr.* **32**, 11 (1976).
139. Evans, G. A., Dan, D. R., Hutchinson, J. W., Meier, G. H. & Pettit, F. S. Mechanisms controlling the performance and durability of thermal barrier coatings. *Prog. Mater. Sci.* **46**, 5–50553 (2001).
140. Rowe, J. J., Morey, G. W. & Hansen, I. D. The binary system K_2SO_4-$CaSO_4$. *J. Inorg. Nucl. Chem.* **27**, 53–58 (1965).

Appendices

Appendix A: Mass Balance of LVBR

Mass Balance for ASTM D1141 Artificial Ocean Water Solution (Diluted 21.3x (LVBR Run #1):

Input Streams:

D1141 Ocean Water (diluted 21.3x)	
Species	Mass Fraction
NaCl	1.31E-03
$MgCl_2$	2.76E-04
Na_2SO_4	2.19E-04
$CaCl_2$	6.18E-05
KCl	3.70E-05
$NaHCO_3$	1.07E-05
KBr	5.37E-06
H_3BO_3	1.44E-06
$SrCl_2$	1.33E-06
NaF	1.60E-07
H_2O	9.98E-01

Solution mass flow rate: 0.371 g/min

Air	
Species	Mass Fraction
N_2	0.755
O_2	0.232
Ar	0.013

Air mass flow rate: 130.05 g/min

F76 Marine Diesel with 0.5 wt% S	
Species	Mass fraction
C	0.857
H	0.139
N	0.06
S	0.5

Fuel mass flow rate: 4.76 mL/min * 0.84 g/mL = 4 g/min

Elemental Mass Flow Rate:

Final Elemental Composition		
Species	Mass (g per min flow)	Mass Fraction
Ar	1.69E+00	1.24E-02
B	8.70E-08	6.37E-10
Br	1.25E-06	9.13E-09
C	3.43E+00	2.51E-02
Ca	7.72E-06	5.65E-08
Cl	3.66E-04	2.68E-06
F	2.50E-08	1.83E-10
H	5.94E-01	4.35E-03
K	7.33E-06	5.36E-08
Mg	2.44E-05	1.78E-07
N	9.84E+01	7.20E-01
Na	2.03E-04	1.49E-06
O	3.05E+01	2.23E-01
S	2.00E+00	1.46E-02
Sr	2.55E-07	1.87E-09
Total	1.37E+02	1.00E+00

Mass Balance for NaCl Solution Injection (LVBR Run #2):

Input Streams:

NaCl Solution	
Species	Mass Fraction
NaCl	1.92E-3
H_2O	BAL

Solution mass flow rate: 0.385 g/min

Air and fuel mass flow rates are the same as above

Elemental Mass Flow Rate:

Final Elemental Composition		
Species	Mass (g per min flow)	Mass Fraction
Ar	1.69E+00	1.24E-02
C	3.43E+00	2.51E-02
Cl	4.60E-04	3.37E-06
H	5.94E-01	4.35E-03
N	9.84E+01	7.20E-01
Na	2.57E-04	1.88E-06
O	3.05E+01	2.23E-01
S	2.00E+00	1.46E-02
Total	1.37E+02	1.00E+00

Mass Balance for $MgCl_2$ Solution Injection (LVBR Run #3):

Input streams:

$MgCl_2$ Solution	
Species	Mass Fraction
$MgCl_2$	2.90E-3
H_2O	BAL

Solution mass flow rate: 0.341 g/min

Air and fuel mass flow rates are the same as above

Elemental Mass Flow Rate:

Final Elemental Composition		
Species	Mass (g per min flow)	Mass Fraction
Ar	1.69E+00	1.24E-02
C	3.43E+00	2.51E-02
Cl	7.37E-04	5.39E-06
H	5.94E-01	4.35E-03
Mg	2.52E-04	1.85E-06
N	9.84E+01	7.20E-01
O	3.05E+01	2.23E-01
S	2.00E+00	1.46E-02
Total	1.37E+02	1.00E+00

Mass Balance for NaCl-$MgCl_2$ Solution Injection (LVBR Run #4):

Input streams:

$MgCl_2$ Solution	
Species	Mass Fraction
NaCl	8.90E-4
$MgCl_2$	1.55E-3
H_2O	BAL

Solution mass flow rate: 0.341 g/min

Air and fuel mass flow rates are the same as above

Elemental Mass Flow Rate:

Final Elemental Composition		
Species	Mass (g per min flow)	Mass Fraction
Ar	1.69E+00	1.24E-02
C	3.43E+00	2.51E-02
Cl	5.37E-04	4.20E-06
H	5.94E-01	4.35E-03
Mg	1.34E-04	9.79E-07
Na	1.18E-04	8.66E-07
N	9.84E+01	7.20E-01
O	3.05E+01	2.23E-01
S	2.00E+00	1.46E-02
Total	1.37E+02	1.00E+00

Appendix B: CFBL Model Example Calculations

Description:

Estimate Na_2SO_4 formation rate on pin samples (1/8” diameter, 2.5” tall) in the LVBR for LVBR Run #2 conditions

Conditions:

- 700 °C in the sample chamber, assume also 700 °C in burner duct
- Injection of NaCl salt solution (2.18 ppmw of Na in combustion gas stream)
- Combustion of F76 Marine Diesel with 0.5 wt% S addition
- Assume NaOH(g) is the diffusing species across the boundary layer and that it forms a stoichiometrically equivalent amount of $Na_2SO_4(s)$ at sample surface
- Assume local thermochemical equilibrium at both boundary layer interfaces
- Assume collisions between NaOH(g) and gas species other than N_2 are infrequent

Governing Equations:

$$J_{NaOH} = \frac{-\rho D_{NaOH,N_2}}{L} Sh_{NaOH}(\omega_{NaOH,e} - \omega_{NaOH,w}) \qquad \text{(CFBL diffusion eqn)}$$

$$J_{NaOH} \approx \frac{-\rho D_{NaOH,N_2}}{L} Sh_{NaOH}(\omega_{NaOH,e}) \qquad \text{because } \omega_{NaOH,e} >> \omega_{NaOH,w}$$

where:

$$D_{NaOH,N_2} \approx 0.0018583\sqrt{\frac{1}{M_{NaOH}} + \frac{1}{M_{N_2}}}\, T^{3/2} \frac{1}{P\sigma^2_{NaOH,N_2}\Omega_D} \qquad \text{(Chapman-Enskog eqn)}$$

$$\sigma_{NaOH,N_2} = \frac{\sigma_{NaOH} + \sigma_{N_2}}{2} \qquad \text{(Collision diameter)}$$

Ω_D is looked up in tables of T*, where $T^* = \sqrt{\varepsilon_{NaOH}\varepsilon_{N_2}}$ (Collision integral)

$$Sh_{NaOH} = 0.3 + \frac{0.62Re^{1/2}Sc^{1/3}}{[1 + (0.4/Sc)^{2/3}]^{1/4}}\left[1 + \left(\frac{Re}{282000}\right)^{5/8}\right]^{4/5} \qquad \text{(Churchill–Bernstein eqn)}$$

$$Re_{NaOH} = \frac{\rho u L}{\mu_{NaOH}} \qquad \text{(Reynolds number)}$$

$$Sc_{NaOH} = \frac{\mu}{\rho D_{NaOH,N_2}} \qquad \text{(Schmidt number)}$$

Calculations:

$$\sigma_{\mathrm{NaOH,N_2}} = \frac{3.804\ \text{Å}^3 + 3.798\ \text{Å}^3}{2} = 3.801\ \text{Å}^3$$

$$\mathrm{T}^* = (1962\ \mathrm{K} * 71.4\ \mathrm{K})^{1/2} = 374.28\ \mathrm{K} \Rightarrow \Omega_D \approx 0.4231$$

$$u = \frac{\dot{m}}{\rho A} = \left(137\ \frac{\mathrm{g}}{\mathrm{min}}\right)\left(\frac{1\ \mathrm{m}^3}{358.6\ \mathrm{g}}\right)\left(\frac{1}{\pi(0.07\ \mathrm{m})^2}\right) = 24.82\ \mathrm{m/\,min} = 0.41\ \mathrm{m/s}$$

$$\mathrm{D}_{\mathrm{NaOH,N_2}} = 0.0018538\sqrt{\frac{1}{39.997\ \frac{\mathrm{g}}{\mathrm{mol}}} + \frac{1}{28.014\ \frac{\mathrm{g}}{\mathrm{mol}}}}\ (973.15\ \mathrm{K})^{3/2}\ \frac{1}{(1\ \mathrm{atm})\left(3.801\ \text{Å}^3\right)^2(0.4231)}$$

$$\mathrm{D}_{\mathrm{NaOH,N_2}} = 2.274\ \frac{\mathrm{cm}^2}{\mathrm{s}}$$

$$\mathrm{Re}_{\mathrm{NaOH}} = \frac{\left(358.6\frac{\mathrm{g}}{\mathrm{m}^3}\right)\left(0.41\frac{\mathrm{m}}{\mathrm{s}}\right)\left(3.175\times10^{-3}\mathrm{m}\right)}{1606\times10^{-6}\frac{\mathrm{g}}{\mathrm{m\cdot s}}} = 290.18$$

$$\mathrm{Sc}_{\mathrm{NaOH}} = \frac{1606\times10^{-6}\frac{\mathrm{g}}{\mathrm{m\cdot s}}}{\left(358.6\ \frac{\mathrm{g}}{\mathrm{g}^3}\right)\left(2.274\times10^{-4}\ \mathrm{m}^2/\mathrm{s}\right)} = 1.969\times10^{-2}$$

The Churchill-Bernstein equation is only valid for Re*Sc > 0.2, so check:

$$\mathrm{Re}_{\mathrm{NaOH}} \cdot \mathrm{Sc}_{\mathrm{NaOH}} = (290.18)(1.696\times10^{-2}) = 5.7 > 0.2$$

$$\mathrm{Sh}_{\mathrm{NaOH}} = 0.3 + \frac{0.62(290.18)^{1/2}(1.969\times10^{-2})^{1/3}}{\left[1 + (0.4/1.969\times10^{-2})^{2/3}\right]^{1/4}}\left[1 + \left(\frac{290.18}{282000}\right)^{5/8}\right]^{4/5} = 1.991$$

$$\mathrm{J}_{\mathrm{NaOH}} \approx \frac{\left(-35\ \ .6\frac{\mathrm{g}}{\mathrm{m}^3}\right)\left(2.274\times10^{-4}\ \frac{\mathrm{m}^2}{\mathrm{s}}\right)}{3.175\times10^{-3}\mathrm{m}}(1.991)\left(3.78\times10^{-6}\ \frac{\mathrm{g}}{\mathrm{g}}\right) = -1.933\times10^{-4}\ \frac{\mathrm{g}}{\mathrm{m}^2\cdot\mathrm{s}}$$

$$\mathrm{J}_{\mathrm{Na_2SO_4}} = -\left(-1.933\times10^{-4}\ \frac{\mathrm{g\ NaOH}}{\mathrm{m}^2\cdot\mathrm{s}}\right)\left(\frac{142.04\ \mathrm{g\ Na_2SO_4}}{2\cdot39.997\ \mathrm{g\ NaOH}}\right)\left(\frac{10\ \mathrm{mg}}{\mathrm{g}}\right)\left(\frac{1\ \mathrm{m}^2}{10^4\ \mathrm{cm}^2}\right)\left(\frac{3600\ \mathrm{s}}{\mathrm{h}}\right)$$

$$\mathrm{J}_{\mathrm{Na_2SO_4}} = 1.24\times10^{-3}\ \frac{\mathrm{mg}}{\mathrm{cm}^2\cdot\mathrm{h}}$$

(The flux of Na_2SO_4 in the opposite direction can be neglected as this is well below the dew point)

Python source code used to generate Figure 72:

```
import numpy as np
import scipy.interpolate

# Chapman=Enskog eqn, returns D_ij
def chapman_enskog(T, P, i, j, omega):
    # get properties data
    M_i = i[1]
    M_j = j[1]
    sigma_i = i[2]
    sigma_j = j[2]

    # calculate sigma_ij
    sigma_ij = (sigma_i + sigma_j) / 2

    # C-E Eqn broken up into parts for clarity
    CE1 = (1 / M_i) + (1 / M_j)
    CE2 = 1 / (P * sigma_ij**2 * omega)

    return 0.0018583 * CE1**(1/2) * T**(3/2) * CE2

# lookup omega from T* of molecules i and j, uses csv table
def omega(i, j):
    epsilon_i = i[3]
    epsilon_j = j[3]
    T_star = (epsilon_i * epsilon_j)**(1/2)

    # first check if T_star can be interpolated from table
    if T_star < 0.3 or T_star > 400:
        raise Exception("Error: T_star is out of range")

    # lookup value from table if interpolation is possible
    else:
        return table_interp("omega.csv", T_star)

# returns sherwood number for cylinder in crossflow
def sherwood_no(Re_i, Sc_i):
    # check if Churchill-Bernstein eqn may is valid for this flow regime
    if Re_i * Sc_i > 0.2:
        # Churchill-Bernstein Eqn broken up into smaller terms for clarity
        CB1 = 0.62 * Re_i**(1/2) * Sc_i**(1/3)
        CB2 = 1 + (0.4 / Sc_i)**(2/3)
        CB3 = 1 + (Re_i / 282000)**(5/8)
        return 0.3 + CB1 * CB2**(-1/4) * CB3**(4/5)

    else:
        raise Exception("Error: Re * Sc < 0.2")

# returns Re_i
def reynolds_no(rho, u, L, mu_i):
    return rho * u * L / mu_i

# returns Sc_i
def schmidt_no(mu_i, rho, Dij):
    return mu_i / (rho * Dij /10000)

# returns viscosity of species i at temp T
# defaults to NaOH viscosity if compound data not found
def mu(i, T):
    try:
        return table_interp(f"{i[0]}.csv", T)

    except:
        return table_interp("NaOH.csv", T)

# returns density of air at temp T in g/m^3
def rho_lookup(T):
```

```
    return 352009 * T**(-1.00170)

def table_interp(filename, value):
    with open(filename, newline = "") as file:
        table = np.loadtxt(file, skiprows = 1, dtype = float)

    x = table[:, 0]
    y = table[:, 1]

    interpolated = scipy.interpolate.interp1d(x, y, kind = "linear")

    return interpolated(value)

# general diffusion/convection eqn
def J_i(T, P, u, L, i, j, c_i):
    omega_i = omega(i, j)
    mu_i = mu(i, T)
    rho = rho_lookup(T)
    D_ij = chapman_enskog(T, P, i, j, omega_i)
    Re_i = reynolds_no(rho, u, L, mu_i)
    Sc_i = schmidt_no(mu_i, rho, D_ij)
    Sh_i = sherwood_no(Re_i, Sc_i)
    J_i = rho * (D_ij / 10000) * Sh_i * c_i / L

    return J_i

def single_point_calc(T, u):
    # molecule data in form [name, MW, sigma, epsilon, mu]
    # using NaOH L-J data for compounds not in Svehla
    naoh = ["NaOH", 39.997, 3.804, 1962]
    koh = ["KOH", 56.11, 3.804, 1962]
    mgo = [" MgO", 40.304, 3.804, 1962]
    cao = ["CaO", 56.0774, 3.804, 1962]
    na2so4 = ["Na2SO4", 142.04, 3.804, 1962]
    k2so4 = ["K2SO4", 174.259, 3.804, 1962]
    n2 = ["n2", 28.014, 3.798, 71.4]

    # set conditions
    P = 1
    L = 0.003175

    # compositions given by LVBR mass balance and vapor pressures
    c_naoh = 0.00000378
    c_koh = 0.000000077
    c_mgo = 0.000000295
    c_cao = 0.000000079
    c_na2so4 = table_interp("Na2SO4_vp.csv", T) * (na2so4[1] / n2[1])
    c_k2so4 = table_interp("K2SO4_vp.csv", T) * (k2so4[1] / n2[1])

    # solve for inward fluxes (from gas stream toward surface)
    J_naoh = J_i(T, P, u, L, naoh, n2, c_naoh)
    J_koh = J_i(T, P, u, L, koh, n2,  c_koh)
    J_mgo = J_i(T, P, u, L, mgo, n2,  c_mgo)
    J_cao = J_i(T, P, u, L, cao, n2, c_cao)

    # solve for outward fluxes (from surface to gas stream)
    # factor of 3.6 is to convert from g, m^2, h to mg, cm^2, s
    J_na2so4_out = J_i(T, P, u, L, na2so4, n2, c_na2so4) * 3.6
    J_k2so4_out = J_i(T, P, u, L, k2so4, n2, c_k2so4) * 3.6

    # handle stoichiometry
    J_na2so4 = J_naoh * (na2so4[1] / (2 * naoh[1])) * 3.6
    J_k2so4 = J_koh * (k2so4[1] / (2 * koh[1])) * 3.6
    J_mgso4 = J_mgo * (120.366 / mgo[1]) * 3.6
    J_caso4 = J_cao * (136.14 / cao[1]) * 3.6

    J_na_net = (J_na2so4 - J_na2so4_out)
    J_k_net = (J_k2so4 - J_k2so4_out)
    J_total = J_na_net + J_k_net + J_mgso4 + J_caso4
```

```
    return [J_total, J_na_net, J_mgso4, J_k_net, J_caso4]

if __name__ == "__main__":
    data = []
    T = 873.15
    T_end = 1373.15
    interval = 1

    while T <= T_end:
        row = single_point_calc(T, 0.41)
        row.append(T)
        data.append(row)
        T += interval

    np.savetxt("output.csv", data, delimiter = "\t")
```